N° d'ordre : 41725

THESE

Présentée à l'Université de Lille 1
Ecole Doctorale Sciences Pour l'Ingénieur

Pour obtenir le grade de :

DOCTEUR DE L'UNIVERSITE

Spécialité : Micro et nano technologies, acoustique et télécommunications

Par

Ragavendran SIVAKUMARASAMY

Institut d'Electronique, de Microélectronique et de Nanotechnologie

Biocapteurs à base de nanotransistor 0D / 0D nanotransistor Biosensors

Soutenance prévue le 20 avril 2015 devant la Commission d'examen

Membres du jury :

Dr. Dominique VUILLAUME	Directeur de thèse (IEMN - Lille)
Dr. Nicolas CLEMENT	Co-directeur de thèse (IEMN - Lille)
Dr. Anne-Marie GUE	Rapporteur (LAAS - Toulouse)
Dr. Anne CHARRIER	Rapporteur (CiNAM - Marseille)
Dr. Guilhem LARRIEU	Membre (LAAS - Toulouse)
Dr. Gilles DAMBRINE	Membre (IEMN - Lille)
Dr. Katsuhiko NISHIGUCHI	Invité (NTT Basic Research Laboratories - Japan)

Acknowledgements

Most successful research efforts require significant help from a lot of people. I spent the last three years learning that lesson despite my best efforts to deny the truth of it. Even when I was imagining myself to be “going it alone” there were a number of people whose support was instrumental to keeping me heading toward the goal of producing this dissertation. Some of these people contributed directly to the science and engineering, while other helped me to properly place my experiences in lab within the larger context of my life.

First and foremost, I would like to express my gratitude and heart full thanks to my PhD supervisor Nicolas Clément. He provided guidance at all key moments in my work and helped with his immense knowledge to solve problems.

Besides my supervisor, I would like to thank the rest of the thesis committee:
Dominque Vuillaume, Anne-Marie Gue, Anne Charrier, Guilhem Larrieu and Gilles Dambrine for their handful support.

I wish to thank all technical engineers Francois Vaurette, David Guerin, Pascal Tilmant, Vanessa Avramovic, Marc Dewitte, Charlene Billard, Etienne Okada for their technical help in the cleanroom and laboratory.

I wish to thank Yannick Coffinier for providing foetal bovine serum and Dr. M. Clément at “Clinique Veterinaire du clair matin” for performing the ionogram for blood serum with IDEXX catalyst Dx biochemical analyzer.

Special thanks to my office mates, Sathya Punniyakoti, Jeorge Trasobares, Fei Wang, Selina La Barbera. It was a great time to share technical thoughts with them.

I am greatful to the administrative committee at IEMN and University of Lille 1 for their administrative support.

This study was funded by Singlemol and BQR projects from Nord-Pas de Calais Council and Lille University, France and NTT Basic Research Laboratory, Japan in close collaborators of Katsuhiko Nishiguchi and Akira Fujiwara.

Thanks Mom and Dad for teaching me to love learning and to never be finished with it. Thank you both for all you have done to get me here. I wouldn’t be in this position without your example and support.

My final words of thanks are reserved for my wife Gomathi Vairam and my little son Keshav. Because of their encouragement, love, forgiveness, patience I made it through without too many scars. I love you and while I'm no longer a student, I hope to study you for the rest of my life.

Acknowledgments

List of Acronyms and Symbols

List of Figures

List of Tables

Chapter1: PDMS/silicon chip alignment with sub-µm precision

Chapter 2: Ultimate Integration of a PDMS-based Lab-on-a-Chip with Nanotransistor Biosensors

Chapter 3: U-shape pH response with Zero-Dimensional Nanotransistor Biosensors

Chapter 4: Cation selectivity and super Nerntzian sensitivity with 0D Nanotransistor Biosensors: Application to Blood ionogram

Chapter 5: Conclusions and Perspectives

Abstract

List of acronyms and symbols

ISE	Ion selective electrodes
ISFETs	Ion sensitive field-effect transistors
FET	Field effect transistors
MOSFET	Metal-oxide-semiconductor field-effect transistor
CMOS	Complementary metal oxide semiconductor
IUPAC	International union of pure and applied chemistry
SET	Single electron transistor
SiNW ISFETs	Silicon nanowire ion sensitive field-effect transistors
SiNW FET	Silicon nanowire field-effect transistor
PDMS	Polydimethylsiloxane
RIE	Reactive ion etching
0D ISFETs	Zero dimensional ion sensitive field effect transistors
PADOX	Pattern dependant oxidation
LoCs	lab-on-chips
AFM	Atomic force microscopy
SEM	Scanning electron microscopy
FBS	Foetal bovine serum
RMS	Root mean square
XPS	X-ray photoelectron spectroscopy
0D	Zero dimensional
3D	Three dimensional
2D	Two dimensional
CPE	Constant phase element
PZC	Point zero charge
SBM	Site-binding model
ID	Inner diameter
OD	Outer diameter
ΔD	Misalignment
D	Distance
MHz	Mega Hertz
H	Channel height
W	Channel width
C_d	Critical distance

P_c	Critical pressure
μ	Shear modulus or modulus of rigidity
F	Lateral force
Z_d	Critical PDMS wall displacement
d_{ec}	Distance of the electrical contact pads
$d_{\mu c}$	Distance of microfluidic channel
d_{cc}	Distance from the center of tube inlet to the tube outlet
d_w	Distance of the PDMS1 wall near the electrical contacts
d_{wt}	Distance of PDMS2 wall and the tube
I_{th}	Threshold current
I_d	Drain current
V_{ug}	Liquid-gate voltage
V_d	Drain voltage
V_s	Source voltage
V_{bg}	Back-gate voltage
ΔV_T	Variation in the threshold voltage
V_T	Threshold voltage
C	Capacitance
G	Conductance
G_{liq}	Conductance of microfluidic channel
C_{gs}	Gate source capacitance
G_{ds}	Drain source conductance
C_{bgs}	Capacitance between back gate and source
$C_{lg/Bg}$	Capacitance between the microfluidic channel and the back gate
$C_{pt/Bg}$	Capacitance between the platinum and back gate
ζ	Zeta potential at the PDMS interface
$G_{liq/3}$	Third conductance of a fraction of the microfluidic channel length
ΔV_{bg}	Variation of back gate voltage
V_{Pt}	liquid- gate voltage using Platinum electrode
C_{bg}	Back gate capacitance
C_{lg}	Liquid gate capacitance
C_{dl}	Double-layer capacitance
Ψ_0	Surface potential at liquid / oxide interface

σ_0	Surface charge density
K	Dissociation constant
ν	Density of sites
N_s	Total density of sites
a_{Hs}^{+}	Activity of surface protons
a_{Hb}^{+}	Activity of bulk protons
Δq	Equivalent elementary charge
C_{cg}	Capacitance between liquid gate and the silicon channel
C_{fg}	Capacitance between the storage node and the liquid gate
C_{fc}	Capacitance between storage node and the silicon channel
g_m	Transconductance
a_i	Ion activity
k	Boltzmann constant
T	Temperature
e	Elementary charge
z	Charge of ion or mobile particles
A_i	Nernstian slope
z_i	Ionic valency of ion i
a_{i0}	semi-empirical constant
k_{ij}	Selectivity coefficient
$a_{iunknown}$	Unknown activity of ion i in the unknown solution

List of Figures

Figure 2.7 (a) SEM picture showing the 200 µm-thick PDMS1 just after demolding from the 2 levels mold. A very thin layer of PDMS remains but can easily be removed from blowing or using a needle after which holes extremely well defined **(b)**

Figure 2.8 (a) Schematic view of 1.5 mm x 1.5 mm LoC with PDMS1 showing the Cd and PDMS2 with tubings for inlet and outlet **(b)** Optical microscopic image of the bonded PDMS1 on silicon nanotransistor biosensor chip.

Figure 2.9 (a) Zoom on Figure 2.8b to show aligned 10 µm width microfluidic channel on the 0D ISFETs. **(b)** Picture of the packaged 1.5 mm x 1.5 mm chip

Figure 2.10 (a) Schematic view of the experimental setup used for setting up the critical pressure P_c as a function of C_d. An electrical contact hole at atmospheric pressure P_0 is located at a distance C_d (range: 5-200 µm) from the microfluidic channel. **(b)** Optical microscope image of the experimental setup after leakage. **(c)** Experimental results of P_c (pressure just before PDMS debonding and fluid leakage) as a function of C_d for different channel widths (H = 44 µm). Inset: Schematic view of the PDMS wall deformation under shear stress used to derive Eq 2.1. Debonding area is in orange. **(d)** same as c, but with H = 88 µm.

Figure 2.11 Schematic view of the Lab-On-Chip with the distances to be optimized (d_{ec}, d_w, $d_{\mu c}$, d_{wt}, d_{cc}) for ultimate integration.

Figure 2.12 Optical micrograph showing 400pL NaCl inside the 10 µm microfluidic channel.

Figure 2.13 (a) Schematic view of the electronic connections related to the 0D ISFETs. **(b)** Drain current I_d vs. liquid-gate voltage V_{ug} at different NaCl concentration. V_d = 50 mV, V_s = V_{bg} = 0 V. Inset: scanning electron microscope image of the 0D ISFET (silicon nanowire dimensions: diameter 15 nm, length: 25 nm) **(c)** Variation of the threshold voltage V_T as a function of NaCl concentration at constant pH for the ultimately integrated LoC with PDMS microfluidic channels (black balls for continuous flow and green balls for 400 pL volume) and for microbaths (blue and red balls from ref.3). Inset: optical microscope image showing the 400 pL NaCl inside the microfluidic channel. **(d)** Variation of 0D ISFET's threshold voltage as a function of [NaCl] for 4 different devices in microfluidic channel and **(e)** Schematic figure of SU8 microbath on 0D ISFET adapted from reference [12] **(f)** Variation of 0D ISFET's threshold voltage as a function of [NaCl] for microbath.

Figure 2.14 (a) Zoomed-out optical microscope image from Figure 2.9a, showing the microfluidic channel limit in red (10-µm-wide microfluidic channel) and the nanotransistor below. Black area indicates coupling between the source and liquid gate. Gray area indicates coupling when the microfluidic channel width exceeds 10 µm. **(b)** Schematic view of the experimental setup for measuring the frequency response of the nanotransistor biosensor. Liquid gate and drain are connected together and biased with DC (+0.1 V) plus AC (0.05 V) signals. The measured impedance is transposed to that of an equivalent G-C parallel circuit, with G and C the measured conductance and capacitance, respectively. **(c & d)** Measured C and G as a function of frequency for nanotransistor biosensors with microfluidic channel widths of 10 and 150 µm. **(e)** Schematic equivalent circuit derived from the step-by-step approach done in Figure 2.15 CPE, constant phase element representing the double-layer capacitance at the Pt electrode (see Figure 2.15a for its measurement between two Pt electrodes); G_{liq}, conductance of the microfluidic channel; $C_{Pt/Bg}$, capacitance between the Pt and back gate (independent of the presence of liquid); and $C_{lg/Bg}$, capacitance between the microfluidic channel and the back gate. Component values corresponding to asymptotic fits in (d) and (e) are as follows: $G_{liq\_W=150\mu m}$ ~ 60 nS, $G_{liq\_W=10\mu m} < 6$ nS, $C_{Pt/Bg} = 0.8$ pF, $G_{ds} = 4$ µS.

Figure 2.15 Measured capacitance C and conductance G with the impedancemeter (G, C parallel equivalent circuit) **(a & b)** between two Pt electrodes inside the microfluidic channel. Results are nicely fitted with a constant phase element (CPE) with m=0.75, $A=3\times10^{-11}$ [at 1M], $A=2\times10^{-11}$ [at 0.1M], $A=8\times10^{-12}$ [at < 0.1M] shown in **(g). (c & d**) between a Pt electrode inside the 200 µm microfluidic channel and the back-gate. Results are nicely fitted with a constant phase element (CPE), with m=0.2, $A=2\times10^{-7}$ [at 1M], $A=5.5\times10^{-8}$ [at 0.1M], $A=1.5\times10^{-8}$ [at 10^{-2}M], $A=4.5\times10^{-9}$ [at 10^{-3}M], $A=2\times10^{-9}$ [at 1µM] shown in **(h). (e & f)** Between a Pt electrode inside the microfluidic channel and the back-gate for 3 different microfluidic channel widths.

Figure 2.16 (a) Drain current-liquid gate nanotransistor characteristics for microfluidic channel widths of W = 10 µm and W = 200 µm. In both cases, $V_{bg} = -16$ V, to be in the usual front-channel operation mode. **(b)** Threshold voltage V_T (measured at $I_d = 5$ nA) plotted as a function of microfluidic channel width W. The error bar, which is larger than the error related to ionic strength, corresponds to the typical dispersion in V_T between 0D ISFETs when a large microfluidic channel width is used. Inset: Schematic equivalent circuit. ζ, zeta potential at the PDMS interface; and $G_{liq/3}$, third of the conductance of a fraction of the microfluidic channel length. **(c)** Schematic cross-sectional view of the PDMS device, with negative charges at the interface (ξ potential) and the nanoscale transistor with electrons that can be in the front or back channel. **(d)** I_d–V_{lg} for different V_{bg} values from 0 to -18 V, by steps of $\Delta V_{bg} = 2$V. Beige color indicates the back-channel operation mode (large interspacing between I_d–V_{lg} curves). Peach color corresponds to front-channel operation. W = 200 µm. **(e)** Similar curve as (d), but with W = 10 µm. (f) V_T–V_{bg} curve for all microfluidic channel widths obtained from the V_T at each V_{bg}, as indicated in (d) and (e). Dashed line indicates the biasing conditions for (a) (front-channel mode).

Figure 2.17 (a) Figure 2.16b is plotted with an additional ionic strength (1 µM) to highlight the small impact of ionic strength on the observed effect. **(b)** Schematic cross section view of the device composed of PDMS with negative charges at interface (potential Ψ_0), the nanoscale transistor with electrons that can be either in front- or back-channel and capacitive coupling C_{PDMS}, C_{Pt} to the device **(c)** Schematic equivalent circuit proposed in Figure 2.16b inset. By playing with the value of G_{liq} using Orcad Pspice simulator, we see that V_{Pt}-V_{lg} α $1/G_{liq}$, that led us to the semi-empirical law (Eq 2.3) that fits nicely experimental results (Figure 2.16b).

Figure 3.1 (a) Schematic view of pH glass electrode (GE) **(b)** plot showing universal monotonic decrease of surface potential Ψ_0 with pH, The point zero charge pH value is set to PZC =2 as usual for SiO_2 **(c)** Figure reprinted from reference [15]. Plot showing magnitude of surface charge density (σ) increases with decrease in particle diameter for fixed background salt concentration and pH **(d)** Figure adapted from reference [17]. The absence of charge sites in graphene surface showing flat pH response, substantially reduced sensitivity of ~ 0 mV/pH.

Figure 3.2 (a) Schematics illustrate the acid-base equilibrium (chemical reaction) on SiO_2 surface and the potential distribution of double layer formed at a solid material that immersed in an electrolyte solution **(b)** charge distribution at an oxide-electrolyte solution interface.

Figure 3.3 (a) Schematic view of ion-sensitive field-effect transistor (ISFET) **(b)** the nanowire ISFET and **(c)** the 0D ISFET proposed in this study **(d)** Drain-current (I_D) versus gate voltage (V_G) curve showing typical oscillations of a single-electron transistor (SET) or quantum dot at “elevated” temperature when liquid gate is replaced by a polysilicon gate.

Figure 3.4(a) Scanning Electron Microscope (SEM) image of a nanoribbon ISFET (W= 10 µm, L= 7 µm, thickness = 40 nm) used as a reference sample to extract the properties of our hydrated thermal SiO_2 and to illustrate conventional pH response obtained with the Site Binding Model (SBM). **(b)** Plot of the surface potential Ψ_0 versus pH for the large ISFET. Solid black balls represent experimental data points whereas red line is the theoretical fit with SBM (red) and blue lines are theoretical borders of SBM often called Nernst limits for pH sensors shown in Figure 3.1a, 3.3a and 3.3b. The measured threshold voltage V_{th} were converted to surface potential via Ψ_0=V_{th} (PZC)-V_{th} **(c)** raw transistor characteristics (Drain-current - $V_{Ag/AgCl}$ at different pH values for the large nanoribbon ISFET) and extraction of Ψ_0. The point zero charge pH value is set to PZC=2 as usual for SiO_2.

Figure 3.5 (a) Scanning Electron Microscope (SEM) image of 0D ISFET (after thermal oxidation, silicon channel width W = 15 nm and length L= 25nm are obtained) **(b)** Plot of the surface potential Ψ_0 versus pH for the 0D ISFET. Solid black balls represent experimental data points with a U-shape curve. Blue lines are asymptotic guides for eyes. Shaded areas in Figure are used to highlight the rupture in concept between conventional and 0DISFET devices. Due to uncertainty in exact pH value near pH=7, point are not represented in this pH range **(c)** Drain-current (I_D) versus $V_{Ag/AgCl}$ curve at different pH values for 0D ISFET. From the curve threshold voltage V_{th} were converted to surface potential via $\Psi_0=V_{th}$ (PZC)-V_{th}

Figure 3.6 (a)-(d) Plot of the surface potential Ψ_0 versus pH for four identical device of 0D ISFET measured simultaneously showing similar results. It is seen that two back-to-back curves composed of a plateau and a slope of ~ ±59 mV/pH with a symmetry axis at pH = 6.

Figure 3.7 (a) Schematic cross section view of the 0DISFET showing typical surface functional groups at the surface of SiO_2, and Na^+ counter ions (for NaOH, at pH ≥ 8) **(b)** Estimation of the density of SiOH, SiO^- and $SiOH_2^+$ sites and their number on 0DISFET's SiO_2 sensing layer as a function of pH based on the SBM using pK_a = -2, pK_b = +6 and a total density of sites $N_s = 5x10^{18}$ m^{-2} and $N_s = 10^{16}$ m^{-2}. Because we don't observe the monotonic pH response, the later value of N_s is considered as an upper estimation for 0D ISFETs. When N_s is low (e.g $N_s = 10^{16} m^{-2}$), the SBM predicts a reduction of [SiOH] with pH, leading to N_s = [SiO^-] at high pH. The SiO_2 sensing layer area is $2.75x10^{-15}$ m² (35 nm-thick SiO_2 gate oxide).

Figure 3.8 (**a**) Density of SiO^- sites and their number on the 0DISFET's SiO_2 sensing layer as a function of pH based on the SBM using pK_a = -2, pK_b = +6 and different densities N_s of available sites (corresponds to [SiOH] at pH=2). The SiO_2 sensing layer area is $2.75x10^{-15}$ m² (35 nm-thick SiO_2 gate oxide) **(b)** Estimation of the surface potential Ψ_0 as a function of pH for different N_s. **(c)** zoom on (b) for lowest N_s. A density of 10^{16} m^{-2} corresponds to only 30 SiO^- sites at maximum on the 0D ISFET (see c) resulting in a shift of 30 mV that could'nt be clearly distinguished in experimental datas. Above $N_s = 10^{16}$ m^{-2}, we believe that we would have detected the signal arising from SiO^- sites (ex 400 mV for $N_s = 5\times10^{18}$ m^{-2}).

Figure 3.9 (a) Time-dependent fluctuation of Ψ_0 and equivalent charge fluctuation Δq across the gate capacitor as a function of time for a device without defect. Transconductance $g_m = 7.8x10^{-9}S$, gate capacitance C_g = 2aF, current drift is below 1% (range 2.67-2.69 nA), gate voltage V_g = 0V. **(b)** Zoom from Figure (a) with a red line as a guide for eyes to highlight discrete events. The amplitude could correspond quantitatively to the equivalent charge fluctuation induced by the reversible transition of a single SiOH site into SiO^- site **(c)** Schematic cross-section of a single molecule memory in liquid-gate showing capacitive coupling with the various elements (C_{cg}, C_{fc} and C_{fg}) **(d)** Figure adapted from reference 26. Measurement of long-term drift in Q_0 (t) as a function of time showing stability of ΔQ_0 (t) < 0.01e, under vacuum and at temperature below 0.1 K

Figure 3.10 (a) Schematic cross-section of a single electron memory in liquid-gate showing capacitive coupling with the various elements (C_{cg}, C_{fc} and C_{fg}) **(b)** time domain electrical characteristic when a single active defect is near the channel with single-electron trapping / detrapping (large fluctuation amplitude) with 60% current fluctuation (100 pA-160 pA). $V_g = -0.96$ V, $g_m = 4.65\text{x}10^{-10}$ S, $C_{cg} = 2$ aF.

Figure 3.11 (a) Strain and **(b)** stress obtained from the simulation of dry oxidation at 1000°C for 80 mn. Figure adapted from the above mentioned reference [41] Colors have been added for clarity.

Figure 3.12 (a) Contact angle (~74°) at the end of the device fabrication, before insertion in a lab-on-chip **(b)** Contact angle (~14°) after plasma O_2 at 120 W and 0.7 mbar for 180 s, a step necessary for PDMS-based lab-on-chip fabrication (as discussed in Chapter1 and Chapter2). **(c)** Distribution plot of surface charge groups as a function of temperature. Figure adapted from reference 30 **(d)** Schematic cross section view of the 0D ISFET in the hypothesis of unhydroxylated silica at the nanoconstriction (fully covered with siloxane bonds). The charge of siloxane bond is neutral but strong dipoles tend to attract cations **(e)** Schematic 3D view of the 0D ISFET's SiO_2 interface showing a proposed pattern-dependent surface chemistry with mainly silanol groups on large access leads and siloxane groups on top of the nanoconstriction.

Figure 3.13 (a) Topography AFM image of the 0D ISFET. **(b)** Schematic graph of a typical force-distance curve done with an AFM. **(c)** Using Peak-force AFM (Brüker), at each pixel, a force-distance curve is done, which allows plotting the adhesion map, each pixel is 1 nm.

Figure 3.14 (a) I_d-$V_{Ag/AgCl}$ curves for a silicon nanoribbon transistor and a 0D ISFET showing the shift of threshold voltage to higher voltages for the smallest device **(b)** Simplified schematic cross-section view of the two "large" MOSFETs in the "on" state (accumulation of electrons in the channel) whereas the nanoconstriction is at its threshold voltage.

Figure 3.15 (a) Schematic 3D view of the 0DISFET's SiO_2 interface showing a proposed pattern-dependent surface chemistry with mainly silanol and SiO^- groups on large access leads and silanol groups on top of the nanoconstriction **(b)** Schematic cross section view of the 0D ISFET in the hypothesis of silica with large pK_b at the nanoconstriction (fully covered with siloxane bonds). The charge of silanol bond is neutral but strong dipoles tend to attract cations.

Figure 4.1 Schematic figures highlighting the use of ISFET based nanosensors in various applications of which we have shown super Nerntzian sensitivity of Na^+, K^+ Ca^{2+}, and Mg^{2+} in serum using our 0D ISFETs. This can be proof of principle towards biomedical field.

Figure 4.2 Schematic representation of 3 commercial equipments used to measure electrolytes concentration in serum; **(a) Method 1**: Socimed serie ISE: use only ISEs **(b) Method 2**: Fuji Dri-chem Nx500: hybrid approach using Potentiometric method for Na^+, K^+ and Cl^- , Colorimetric method for Ca^{2+} and Mg^{2+} **(c) Method 3**: Idexx catalyst dx: dry-slide technology, colorimetric method.

Figure 4.3 (a) Ψ_0 is plotted as a function of ions activity a_i for five different solutions (KH_2PO_4, NaCl, KCl, HCl, LiCl and NaOH). The solid line corresponds to the full Nernstian response (slope of +59 mV / log a_i). **(b)** A_i from fits of (a) with Eq 4.1 is plotted for all tested solutions. The Nernst limit of 59 mV / log a_i is indicated as a black line.

Figure 4.4 (a) Datas of a_{i0} extracted from Figure 4.3a are plotted as a function of cations charge **(b)** as a function of cations radius **(c)** as a function of hydrated cations radius.

Figure 4.5 Figures reprinted from reference [6] **(a)** Radial distribution functions of Na^+ and K^+ peaks corresponds to contact ion pairing between the carboxylic groups and the metal cations and solvent-separated ion pairs **(b)** for divalent ions of Ca^{2+} and Mg^{2+}.

Figure 4.6 (a) Ψ_0 is plotted as a function of Na^+ activity for 3 different pHs (2, 5 and 10) to verify equation Eq 4.1 Fitting parameters are A_{Na+}=0.09 V/log(a_{Na+}), A_{H+}=0.059 V/pH, a_{NaCl0}=5x10^{-4}M/L, a_{HCl0}=5.3x10^{-4}M/L, **(b)** Ψ_0 is plotted as a function of Na^+ activity for 3 different KCl concentrations (10^{-5} M, 10^{-4} M and 10^{-2}M). Fitting parameters are A_{Na+}=0.09 V/log(a_{Na+}), A_{K+}=0.059 V/pH, a_{NaCl0}=10^{-3}M/L, a_{KCl0}=3x10^{-4}M/L.

Figure 4.7 (a) Schematic representation of a new technique based on Eq 4.3 to extract selectively of a cation concentration without selective coating layer. For example, to extract the concentration of Mg^{2+} in an unknown solution, we add $MgCl_2$ salts in the unknown solution until reaching a threshold in Ψ_0 (spike technique). Best quantitative results are reached by considering a large range of ion concentrations and fitting with Eq 4.3 **(b)** Sensitivity of this device is determined by a_{i0} extracted from cation response in DI water (Eq 4.1). It is good enough for ionogram application **(c)** Example of difference between Eq 4.3 and Eq 4.2 for a minority ion in serum such as Mg^{2+}. With Eq 4.2 with κ_i =1 for all ions, only the majority ions (Na^+) would be detected in blood serum. **(d)** Optical image of the lab-on-chip used for this blood ionogram. Scale bar is 50 µm. It includes electrical contact pads, four identical 0D nanotransistor biosensors, two Pt gates and a 200 µm-large microfluidic channel with inlets / outlets for Pt tubes. **(e)** Zoomed image on the sensor zone (black square area on figure d).

Figure 4.8 (a) $\Delta\Psi_0$-[$MgCl_2$] is plotted for DI water and FBS. Sensitivity is enough to detect [Mg^{2+}] in FBS (shift to higher [$MgCl_2$]). Good fits are obtained with Eq 4.3. **(b)** $\Delta\Psi_0$-[ ], with [ ] corresponding to $MgCl_2$, $CaCl_2$, KCl and NaCl concentrations, are fitted with Eq 4.3 **(c)** Extracted cations concentrations from fits of (b) and error bars are compared with values provided by life technologies, except for [Mg^{2+}] (not provided by life technologies) that was analyzed with IDEXX catalyst Dx biochemical analyzer.

Figure 4.9 (a) Experimental histogram of threshold voltage variation from 100 measurements with the same device: liquid = DI water) **(b)** liquid = DI water + 0.1M $MgCl_2$ (c) liquid=FBS (d) liquid = FBS + 0.1M $MgCl_2$

Figure 4.10 (a) simulated $\Delta\Psi_0$ curve as a function of Mg^{2+} concentration based on the Gaussian distribution with a standard deviation in Ψ_0 of 20 mV. Each point is generated randomly **(b)** Simulated $\Delta\Psi_0$ curve as a function of Mg^{2+} concentration based on the Gaussian distribution with a standard deviation in Ψ_0 of 20 mV. Each point is the average from 1000 measures generated randomly **(c)** Simulated standard deviation to the concentration expected (normalized in %) as a function of the number of measurements per concentration and the number of concentrations measured. The SD expected for commercial application (1.5%), is represented by a black line.

Figure 4.11 (a) S13a $\Delta\Psi_0$-[ ], with ai corresponding to NaCl **(a-d)** and KCl concentrations **(e-h)**, are fitted with Eq 4.3 for four devices. Estimated concentrations and standard errors are indicated in each figure.

Figure 4.12 $\Delta\Psi_0$-[ ], with a_i corresponding to $CaCl_2$ **(a-d)** and $MgCl_2$ concentrations **(e-h)**, are fitted with Eq 4.3 for four devices. Estimated concentrations and standard errors are indicated in each figure.

Figure 4.13 (a) 1 µm x 500 nm AFM topographic image on the large pad before incubation 1 night in FBS (rms roughness: 0.4 nm) **(b)** after incubation 1 night in FBS (rms roughness: 1 nm) **(c)** AFM topographic image of the 0D ISFET and contact pads after 1 night insertion in FBS **(d)** Adhesion image related to (c)

Figure 5.1 Electrophoretic mobility µe of PS- liposomes as a function of [$La(NO_3)_3$] taken from reference [2]. Black squares corresponds to PS- (no background electrolyte), red circles to PS- with 100 mM of $NaNO_3$ as a background electrolyte. Inset: Chemical structure of the PS- lipid. In reference [2], quantitative discussion on these curves was mainly related to the concentration at which μ_e=0. Using Eq 5.2, we obtained good fits considering A_i = 3x59mV/log ([La^{3+}]) and a_{i0}=2 x 10^{-5} M/L. The shift in μ_e for the black and red curves look similar to the shifts shown in Fig.3D with 0D nanotransistor biosensors. Quantitatively, it corresponds to a shift in zeta potential of ~ +14 mV, a feasible value if ai0 for $NaNO_3$ is in the range of 10^{-4} M/L. The triple Nernstian slope for trivalent ions may be possible given that a twice Nernstian slope is found for divalent ions. This example shows the potential of biomimetics studies of biomolecules charge compensation with 0D nanotransistor biosensors and vice versa. For example, it was recently suggested that the saturation observed in this figured (fitted with a simple log dependence) may be related to some condensation mechanisms [3, 4].

Figure 5.2 (a) Schematic view of the HSQ-based process for nanofluidics. 900 nm-thick HSQ is first spin-coated. HSQ walls and stairs are written within a unique and short e-beam lithography step (typically 1 mn/chip). HSQ is densified by plasma O_2 and the PDMS microfluidic channel is then aligned and bonded. **(b)** Scanning Electron Microscope (SEM) top views of the HSQ nanochannels and Atomic Force Microscope image topography image of HSQ stairs with a cross section. Channel width W is 3 µm at inlets and outlets and below 100 nm at the nanoconstriction that defines the nanofluidic channel. **(c)** Histogram of nanofluidic channel width measured by SEM for 37 channels. Average width is 97 nm and standard deviation σ = 3.7 nm.

Figure 5.3 Optical microscope images of PDMS-sealed nanofluidics channels under constant pressure of 3 bars at different times.

List of Tables

Introduction

The senses are the key to life in all living organisms. Although this happens in different ways, the pattern of event is always same accounting to responses to the external stimuli by the receptors. The receptors are specialized cells which can convert stimulus into electrical signal in nerve cells. Endeavour to use same principle and construct instrumentation that measure such parameters have resulted in sensors which can measure physical parameters such as temperature and pressure as well as chemical sensing that can be used to measure the chemical component of the species in air and water, and bio-chemical sensing are the subclass of chemical sensing where the reaction is bio-chemical.

The wish to measure stable, accurate, reliable results provided by the instruments and to quantify them has been existed from the beginning of mankind. It's been hundreds and hundreds of years ago, the first devices to quantify physical sensing were developed and used when *Galileo* invented first thermometer around sixteen hundreds. Similarly in the history of electrochemical sensing, *Cremer* in 1906 developed glass electrode also called as ion selective electrodes (ISE) which determines the electric potential that arises between parts of the fluid, located on opposite sides of the glass membrane is proportional to the concentration of H^+ ion [1]. Later in 1909 *Haber* and his student *Klemensiewicz* took up this idea of *Cremer* invention and made the platform towards electro-and bio-chemical sensing applications [2]. In late 1970s *P. Bergveld* [3], introduced the ion sensitive field effect transistors (ISFET) that emerged with dimension below millimeter square combining the properties of metal-oxide semiconductor transistor (MOSFET) replacing gate electrode by an aqueous solution containing charge carriers with glass electrode-like interface with aim to provide highly integrated cheap sensors.

Today, the electrochemical and biochemical sensor plays a vital role in the fields of environmental protection and monitoring, hazardous disease prevention, and industrial processes that are controlled via pH measurements. It is likely the most measured chemical parameter and the one most people hear or talk about. According to the definition of sensor given by International Union of Pure and Applied Chemistry (IUPAC), “chemical sensors are the devices that can transform chemical signal into an analytically useful signal in a selective and reversible way, ranging from the concentration of a specific species component to the total composition of analysis. The chemical information mentioned above, may originate from chemical reaction of the analyte or from the physical property of the system investigated” [4]. ISFETs are termed as chemically modified sensors, where the metal gate and gate oxide of a general MOSFET are replaced by an aqueous solution containing charge carriers with a reference electrode (usually Ag/AgCl) immersed, and an insulating layer appropriate for detecting a specific analyte. The typical structure of MOSFET, and its modified form replacing transistor metal gate by an aqueous solution to show the structure of ISFET are well described in Figure 1a and Figure1b respectively.

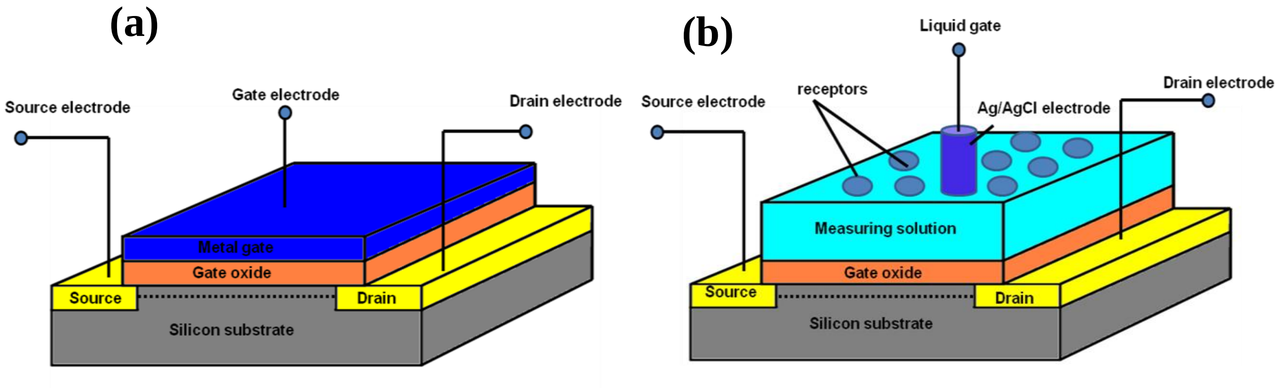

Figure 1 (a) Structure of MOSFET showing the metal gate which is used to modulate the channel conductance **(b)** Structure of an ion-sensitive field effect transistor (ISFET) showing that metal gate of the MOSFET is replaced by a liquid gate. The gate oxide is functionalized with the receptors (charged sites Si-OH, Si-OH^{2+}, Si-O^{-}: blue circles) and directly exposed to the solution containing charged species. When the target species react with the receptors a surface potential builds up that shifts the threshold voltage V$_{th}$. The V$_{th}$ shift depends on the interaction of the target species with the receptors and it is the electrical output of the signal.

Over several years huge efforts has been made in the field of electrochemical research to build chemical sensors with attractive qualities including quick response, low cost, miniaturization, higher sensitivity and selectivity, and appropriate detection limits. So far thousands and thousands of peer-reviewed papers related to electrochemical sensors have been published, showing considerable research effort under this field. In such a vast scope of chemical and bio-chemical sensing, the sensors are driven by both the aspects of its measuring environment and the origin in which it is in. From an analytical point of view, electrochemistry claims electro- and bio-chemical sensing with remarkable detection ability, low cost, experimental simplicity and there is no need of sophisticated instrumentation like optics. A very attractive phenomenon of electrochemical biosensors is the surface chemistry at solid-liquid interface, not an optical path length, and thus choosing very small sample volume, leading itself to miniaturization. By displaying some historical events along the path of the development of the ISFET based sensors; Figure 2 presents an attempt to map out the vast scientific and technological advancements during the past four decades.

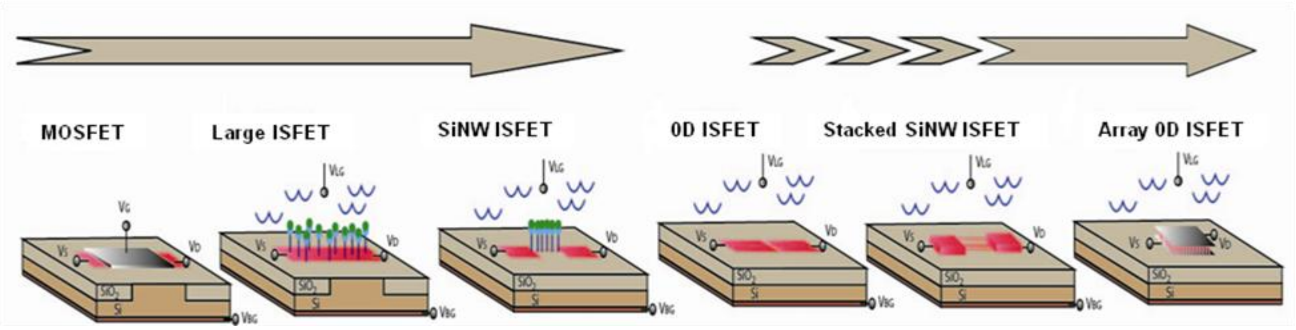

Figure 2 Major historical landmark during the development of ISFET based sensors and eventual perspectives for the future.

Due to wide range of applications especially in areas such as medical diagnostics, monitoring clinical or environmental samples, fermentation and bioprocesses control and testing pharmaceutical or food products, interest in role of sensing towards electronic properties remains unstoppable today. In a daily life, the impact showing their usage become more and more rapid where they continue to meet the economic method of determining numerous analytes [5-7]. So with these fine existing sensing technologies along with the development of new innovative sensor materials including nano- and biological materials [8-11], upgraded data analysis [12], fabrication and miniaturization [13-15], liberty of building new generation sensors such as nanowire or zero-dimensional (0D) sensors [16] with much improved sensitivity and performance are emerging. So, when constructing or developing electrochemical sensors towards some specific application few of their properties can be prioritized and however in order to be feasible for application in medical diagnostics, it would demand sensitivity several orders of magnitude lower. In these cases, response time is limited by transportation of biomolecules to the sensor surface, and hours or even days would be necessary between two consecutive binding events at femto molar sample concentrations [17]. The understanding of silicon nanowire field effect transistor (SiNW FET) sensors operating in electrolyte has been developed these recent years [18, 19], and it has few practical limitations related to the inherent properties of the devices such as drift, low noise, temperature and light sensitivity, and technological limitations such as encapsulation and the need for a stable miniaturized reference electrode. Other features such as the integration of compensation and data processing circuits in the same chip offered still actual perspectives to ISFETs.

The primary focus of this thesis is to study the impact of ultimate integration of nanotransistors on their response when they are immersed in liquid. We call the transistors used in this study as 0D ISFETs or 0D nanotransistor biosensors, because they operate as a single electron transistor (SET) or quantum dot (QD) at high temperature [20]. These 0D transistors were fabricated at NTT Basic research Laboratory, Japan (K.Nishiguchi and A.Fujiwara).

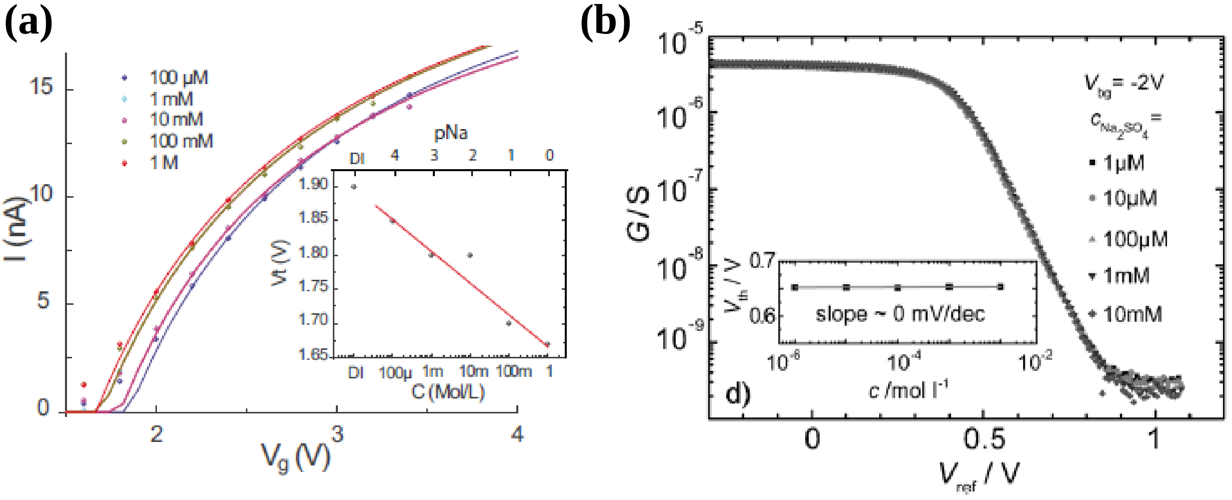

Figure 3 (a) Figure reprinted from reference [21], showing a slope V_T of 59mv/dec for different NaCl concentration for SiNW ISFET with SU8 microbath **(b)** On the opposite the SiNW ISFET showing negligible dependence of V_T as function of Na_2SO_4 salt concentration, Figure reprinted from reference [22].

Previous studies on 0D ISFETs were fabricated with SU8 microbaths [16, 21] showing an unexpected Nernst behavior (see Figure 3a). But for the detailed understanding they were not in the optimal configuration compared to microfluidic channels, because it was difficult to control (the ion concentration in a microdroplet, evaporation and rinsing, etc.). Longer devices such as SiNW based ISFET showed negligible dependence (0 mV / decade) of salt concentration at constant pH [22] (see Figure 3b). Our focus in this thesis was to integrate microfluidic system and understand the behaviour of various salts to the 0D nanotransistor electronic properties and propose perspectives to the emerging field.

This thesis is organized as follows. In Chapter 1 we propose a new technique for PDMS / silicon chip alignment with sub-µm precision that uses no lubricant. In Chapter 2 we address the question of the technological and physical limits for maximum integration of PDMS-based LoCs that includes the critical distance between the microfluidic channel and the electrical contacts below which we observed leakage. We demonstrate a functional 0D nanotransistor biosensor LoC with ultimate integration and discuss the impact of such integration on sensors properties. This study concerns a wide range of sensors and LoCs that require electrical contacts close to a microfluidic channel and ultimate integration. In Chapter 3 we report rupture in the universal pH response of oxide surfaces in liquid that showed monotonic decrease of surface potential with pH to U shape pH response on such 0D nanotransistor biosensors. In chapter 4 we discuss about unique property of ion selectivity measurement of Na^+, K^+, Mg^{2+} and Ca^{2+} in biological serum without specific coating layer on 0D nanotransistor biosensor which may find broad application in medical diagnosis. In Chapter 5 the thesis is concluded with extensive summary and a future outlook.

Bibliography

[1] Cremer, M. Über die Ursache der elektromotorischen Eigenschaften der Gewebe, zugleich ein Beitrag zur Lehre von Polyphasischen Elektrolytketten. — Z. Biol. 47: 56 (1906).

[2] F. Haber und Z. Klemensiewicz. Über elektrische Phasengrenzkräft. Zeitschrift für Physikalische Chemie. Leipzig. 1909 (Vorgetragen in der Sitzung der Karlsruher chemischen Gesellschaft am 28. Jan. 1909).

[3] Bergveld P (1970) Development of an ion-sensitive solid-state device for neurophysiological measurements IEEE Trans. Bio-Med. Eng. BME -17: 70-71.

[4] Hulanicki A, Glab S, Ingman F (1991) Pure & Appl. Chem. 63.1247.

[5] Holford TRJ, Davis F, Higson SPJ (2012) Recent trends in antibody based sensors. Biosensors & Bioelectronics 34:12-24.

[6] Palchetti I, Mascini M (2012) Electrochemical Nanomaterial - Based Nucleic Acid Aptasensors. Analytical and Bioanalytical Chemistry 402:3103-3114.

[7] Perfezou M, Turner A, Merkoci A (2012) Cancer Detection Using Nanoparticle - Based Sensors. Chemical Society Reviews, 41:2606-2622.

[8] Lei J, Ju H (2012) Signal Amplification Using Functional Nanomaterials for Biosensing. Chemical Society Reviews 41:2122-2134.

[9] Liu Y, Dong X, Chen P (2012) Biological and Chemical Sensors Based on Graphene Materials. Chemical Society Reviews, 41:2283-2307.

[10] Sun YF et al. (2012) Metal Oxide Nanostructures and Their Gas Sensing Properties: A Review. Sensors 12:2610-2631.

[11] Silvester DS (2011) Recent Advances in the use of Ionic Liquids for Electrochemical Sensing. Analyst 136:4871-4882.

[12] Ni YN, Kokot S (2008) Does Chemometrics Enhance the Performance of Electroanalysis? Analytica Chimica Acta 626:130-146.

[13] Adibi M, Pirali-Hamedani M, Norouzi P (2011) Copper Nano-composite Potentiometric Sensor. International Journal of Electrochemical Science 6:717-726.

[14] Lin P, Yan F (2012) Organic Thin-Film Transistors for Chemical and Biological Sensing. Advanced Materials 24:34-51.

[15] Scampicchio M et al. (2012) Electrospun Nonwoven Nanofibrous Membranes for Sensors and Biosensors. Electroanalysis 24:719-725.

[16] Clément N, Nishiguchi K, Dufrêche JF, Guérin D, Fujiwara A, Vuillaume D (2013) Water Electrolysis and Energy Harvesting with Zero-Dimensional Ion-Sensitive Field-Effect Transistors. Nanolett 13 (8):3903–3908.

[17] Squires TM, Messinger RJ, Manalis SR (2008) Making it Stick: convection, reaction and diffusion in surface-based biosensors. Nature Biotechnology 26:417–426.

[18] Tarasov A, Wipf M, Stoop RL, Bedner K, Fu W, Guzenko VA, Knopfmacher O, Calame M, Schönenberger C (2012) Understanding the Electrolyte Background for Biochemical Sensing with Ion-Sensitive Field-Effect Transistors. ACS Nano 6 (10):9291–9298.

[19] Wipf M, Stoop RL, Tarasov A, Bedner K, Fu W, Wright IA, Martin CJ, Constable EC, Calame M, Schönenberger C (2013) Selective Sodium Sensing with Gold-Coated Silicon Nanowire Field-Effect Transistors in a Differential Setup. ACS Nano7 (7):5978–5983.

[20] Takahashi Y et al (1995) Fabrication technique for Si single-electron transistor operating at room temperature. Electronics Letters 31(2):136-137.

[21] Clément N, Nishiguchi K, Dufrêche JF, Guérin D, Fujiwara A, Vuillaume D (2011) A silicon nanowire ion-sensitive field-effect transistor with elementary charge sensitivity. Applied Physics Letters 98 (1): 014104.

[22] Oren Knopfmacher et al (2012) Silicon-Based Ion-Sensitive Field-Effect Transistor Shows Negligible Dependence on Salt Concentration at Constant pH. Chem Phys Chem 13(5):1157-1160.

1

PDMS / silicon chip alignment with sub-µm precision

In this Chapter we describe a novel, simple and inexpensive assembly technique with highly accurate alignment of a polydimethylsiloxane (PDMS) layer on a silicon chip for hybrid microfluidic/ electronic applications. When microfluidic system first came into existence in the late 1980s / early 1990s[1, 2], they were fabricated using methods adopted from the manufacturing of microelectronic devices, namely photolithography, wet chemical etching and fusion bonding, as well as the material from this field, namely silicon [3] and glass [4]. In many cases the devices were manufactured using single material, a typical example being a microfluidic channel which was etched into a glass substrate and sealed with a another glass substrate, yielding a monolithic glass chip. In recent years polymers are used extensively as a base material for microfluidic devices in particular thanks to the low cost and easy fabrication process.

The main driver behind this development was the comparative ease of manufacturing of the polymer devices, the use as disposables in the commercial world. Since the need for hybrid device is becoming more noticeable the combination of polymer material with integrated electronic devices opens up the road towards the improved use of biosensors, as in the most cases it includes electronic functions while handling of fluids.

Optically transparent materials, such as glass, epoxy resin, or acrylic resin are widely used for microfluidic devices [5-7]. Among those materials, polydimethylsiloxane (PDMS) is especially effective for biological studies, because of its high biocompatibility, inexpensiveness, flexibility and optical transparency [8, 9]. Microfluidic devices made of PDMS have generally a single layer and are bonded to a glass substrate [10, 11]. However, channels with complex structures are emerging to improve the performance, the functionality and the packing density of the devices [12-16]. In particular, hybrid PDMS microfluidic devices combined with highly integrated sensors on silicon chips [17-20] will require inevitably alignment precision in the micrometer range or lower. Actually, such alignment precision level is only reached for three-dimensional glass structures realized by laminating two or three thin-glass substrates [21, 22]. The tools for automatic alignment are utilizing robotic microhandling and position measurement by optical techniques to achieve a highly accurate alignment [23-25]. However, these tools are not as convenient for devices composed of PDMS substrates, because of the elasticity of PDMS. The deflection caused by the elastic behavior makes it difficult to hold the substrates and to adjust the gap size between them.

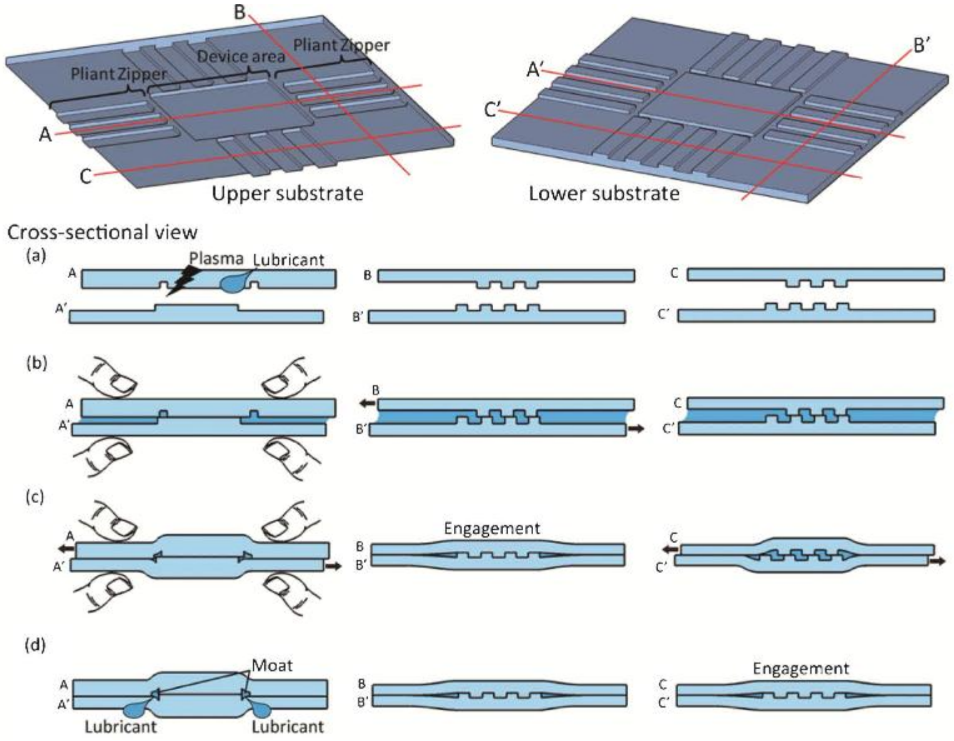

Figure 1.0 Figure reprinted from reference [28] showing novel assembly technique with PDMS-PDMS semi automatic alignment using lubricant.

Furthermore, the sticky surface of the PDMS substrate leads to misalignment when the held substrates are dismounted from the tool. Therefore, free-hand alignment using alignment marks is generally required to assemble microfluidic devices made of laminated PDMS substrates [26]. As a consequence, although PDMS-based technology appears mature, there is still a need for PDMS alignment techniques, by preference simple and inexpensive [27], with micrometric or sub-micrometric precision. Recently, a novel assembly technique with semi-automatic alignment for PDMS substrate has enabled a misalignment average range of less than 1.9 µm [28], although with a 7.9 µm standard deviation (see Figure 1.0). This technique is only available for alignment of two PDMS layers. So far, alignment precision for PDMS/silicon chip in the range of 10 µm has been reported [29]. In that case, shrinkage ratio of PDMS had to be considered (not the case for PDMS-PDMS bonding), which adds another source of misalignment. The optical camera has to be used in sole reflection mode and optimized focus for alignment is only obtained for thin PDMS layers. Nevertheless, lubricant usually used for PDMS alignment [30] induces PDMS deformation for very thin PDMS layers.

Here we propose a new technique based on the electrostatic adhesion force of a 200 µm thick and dense layer of PDMS, that is stronger than its weight, onto a simple metallic cylindrical tool mechanically fixed to an optical microscope. We point out that PDMS shrinkage ratio must be precisely estimated with ppm error for perfect alignment on silicon. Interestingly, this ratio is drastically reduced for thin spin coated PDMS layers. No lubricant coating was necessary with our technique. We evaluated the misalignment error from the patterned silicon chip.

1.1 Principles and Methods

1.1.1 Alignment and bonding tool

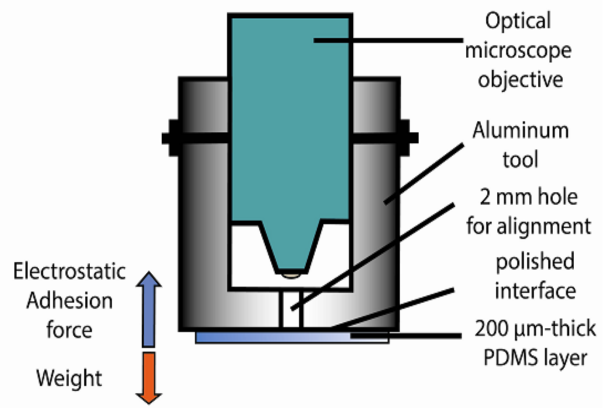

Figure 1.1 Schematic view of the aluminum tool used for PDMS alignment fixed to an optical microscope. The electrostatic adhesion force of a 200 µm-thick layer of PDMS is larger than its

weight. In contrast to usual methods, no lubricant is necessary with this technique.

The alignment tool used in this study is based on the simple observation that adhesion of a 200 µm-thick layer of PDMS to a metallic surface is larger than its weight (Figure 1.1). The inner diameter of the cylinder corresponds to that of optical microscope objective. The outer diameter depends on the sample size (typically 2 or 3 inches). In particular, for large PDMS surfaces, it is important to polish aluminum tool and keep it clean to get high enough electrostatic adhesion. We selected a 5x zoom objective in order to see enough alignment marks and correct precisely tilt angle.

1.1.2 Fabrication

Precise alignment can be done within few minutes using the above described tool. The fabrication process of the thin PDMS layer is slightly different from the conventional process (see section 1.2.2). The only difference is that the ratio of the PDMS curing agent to the base was changed from 1:10 (standard) to 1:3, to ensure that the 200-µm-thick PDMS was dense enough for easy manipulation. Microfluidic channels were fabricated by using conventional soft lithography techniques [31-33].

1.1.3 Alignment process

Figure 1.2 shows the whole alignment process. The lower silicon substrate was patterned with aluminum marks shown in Figure 1.2a. Typically, 150 µm x 150 µm square pads usually used as electrical contacts, were enough for fast positioning of PDMS above the wafer. Smaller patterns (30 µm) were used for precise alignment. The pattern on PDMS (after demolding) matches with the pattern on silicon.

Oxygen (O_2) plasma treatment for permanent bonding was similar to the conventional technique. An oxidation of PDMS and silicon substrates by oxygen plasma treatment (Figure 1.2b) leads to strong intermolecular bonds [34]. PDMS layer was put into contact with the aluminum tool by electrostatic adhesion (Figure 1.2c). Alignment was performed after focus using micrometric lateral and tilt angle positioning (Figure 1.2d). Usually, lubricants, such as water, ethanol, or methanol, are used to reduce the effect of the sticky surface [26]. However, substrate deformation caused by the expanding gas of the lubricant or misalignments during evaporation are typical drawbacks. No lubricant was necessary with our technique.

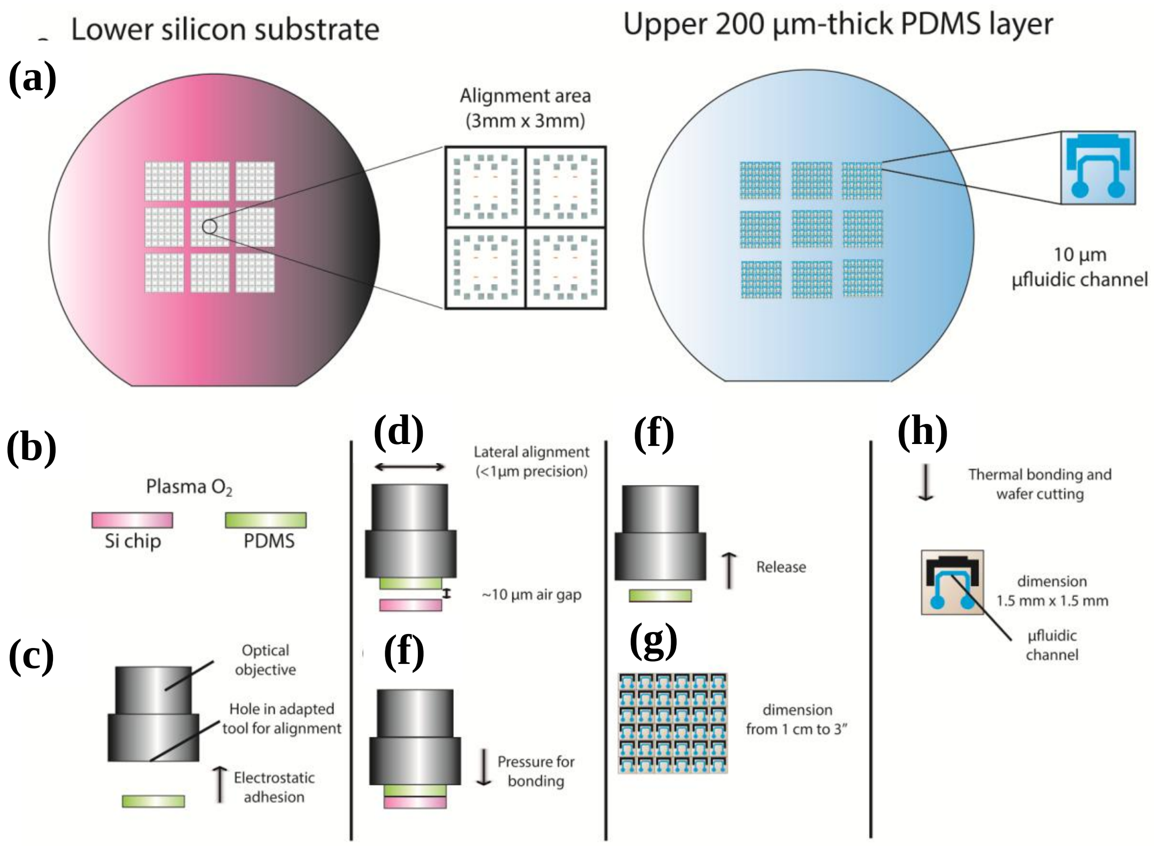

Figure1.2 **(a)** Schematic view of patterned silicon wafer and unmold PDMS layer. **(b)** Both Si and PDMS substrates are exposed to O_2 plasma. **(c)** PDMS layer is put into contact with aluminum tool (usually before mounting the tool). **(d)** PDMS / silicon alignment. **(e)** Vertical displacement of the tool for bonding. **(f)** The tool is released. **(g)** Aligned samples are typically between 1cm and 3inch. **(h)** Chip can eventually be cut into small LoCs after thermal bonding and wafer cutting.

After proper alignment, only a vertical translation was used to put into contact both substrates and the pressure was applied until observation of proper contact between both layers (Figure 1.2e). Then, the tool was released (Figure 1.2f). Because both PDMS and silicon were plasma treated before contact, the bonding strength of both layers becomes larger than the electrostatic force of PDMS / aluminium and PDMS remains attached to the silicon surface. Typical dimensions of both silicon and PDMS substrates vary between 1 cm and 3 inch (Figure 1.2g). After thermal treatment (120 °C) for permanent bonding, silicon wafer can be cut into pieces with a diamond tool.

1.1.4 Shrinkage ratio

Shrinkage of PDMS occurs when it is cured; this is a problem related to the alignment between the PDMS layer and the rigid substrate during the wafer-level processing. S.W. Lee and S.S. Lee have measured experimentally the 2D shrinkage ratio of PDMS for various curing conditions including the temperature, thickness, and mixing ratio of the curing and the diluent. Unfortunately, they have only estimated it for thick PDMS layers (>1 mm). Furthermore, the shrinkage ratio precision was not enough for the alignment precision required in our study. Here, we evaluated the shrinkage ratio of thin PDMS layers rather different from thick PDMS layer [29] that will be discussed in the below section 1.3.

1.2 Experimental details

1.2.1 Alignment tool

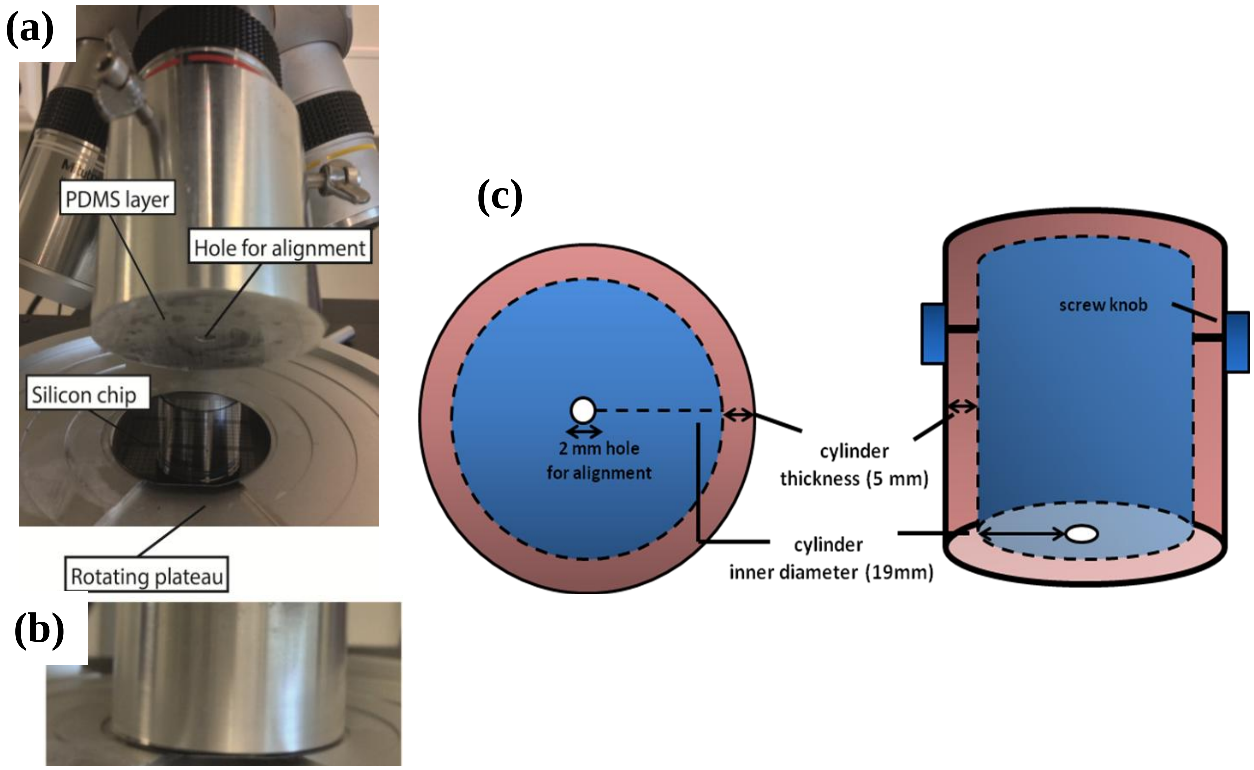

Figure 1.3 Picture of the alignment tool before **(a)** and **(b)** during alignment **(c)** schematic view of tool showing the exact dimension like the diameter of the hole (2mm) at the center for alignment, the cylinder inner diameter (19mm) that fits exactly to the objective of the microscope and the cylinder thickness (5mm).

Figure 1.3 shows the aluminum 2” alignment tool and a schematic view describing the exact dimension of the tool used in this study. It was fixed to a standard optical microscope (Mitutoyo FS110 Inspection Microscope) with large focal length. Optical microscope has two moving parts (i) the precise XYZ stage (translational resolution: 1µm) and (ii) rotating plateau (angular resolution: 0.5°) for tilt angle correction. The aluminium tool grabbing the PDMS layer by electrostatic adhesion is mounted onto the objective of the microscope. The rotating plateau holds the silicon substrate by a double side adhesive tape. The aligning and bonding principle with suggested system is described clearly above. To monitor the aligning process the eyepiece of the microscope is used, and the output is displayed on the monitor.

1.2.2 PDMS device fabrication

Simple schematics for PDMS device fabrication is shown in Figure 1.4. Mixing the two components of PDMS, curing agent to the base (1:3) thoroughly for 10 min and it is then kept inside the desigator connected to vacuum pump for degassing. The uncured PDMS requires the degassing time of 30 min that allows the trapped air bubbles to escape. For PDMS device fabrication of 200 µm thickness, the uncured PDMS was spin-coated on Silicon mold at 300 rpm for 30 sec with an acceleration rate of 100 rpm. It was then cured in two steps: (i) at 65˚C for 20 min in contact with a hot plate, and (ii) in a convection oven at 120 ˚C for one hour. Subjected to separation of PDMS layer from the Si mold is done after removing from the oven and cooled down to room temperature. O_2 plasma treatment before alignment was done at 0.7 mbar, 120 W, for 90 sec. For permanent bonding between Silicon and PDMS, thermal treatment at 120 ˚C for 1hr was carried out.

Silicon mold: S1818 resist (Microposit©) was spin-coated at 2500 rpm with an acceleration of 1000 rpm for 12 s. Silicon was etched using reactive ion etching (RIE). The gases used for the RIE process were SF_6 and O_2. The gas used for passivation was C_4F_8. The flow rates of SF_6, O_2, and C_4F_8 were 450, 45, and 100 standard cm^3 per minute (sccm), respectively. The coil power used was 1000 W. RIE had an approximate etch rate of 4 µm/min. Etching times required to achieve trench depths of 44 µm was 10 min. After etching the wafers, we examined the microstructures on the wafers by optical microscopy. We stripped the remaining photoresist from the silicon wafer by immersing the wafer in EKC 265 at 60 ˚C for 30 min, followed by immersion in acetone and isopropanol for 5 min each. Finally the mold was covered with a 2-µm-thick layer of

C_4F_8 by passivation at a gas flow rate of 220 standard cm^3 / m and a coil power of 1000 W for 60 sec before use.

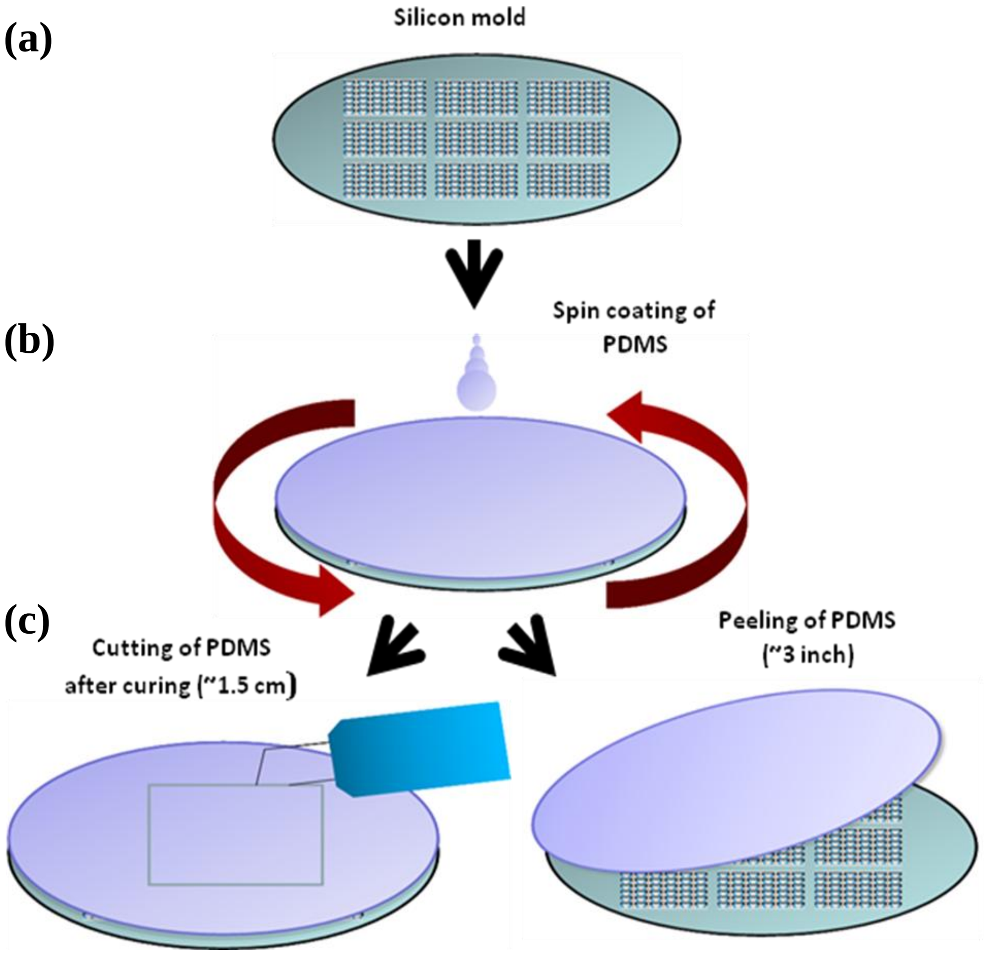

Figure 1.4 (a) Silicon mold prepared by UV lithography and reactive ion etching **(b)** spin coating of PDMS gel on silicon mold **(c)** cutting of PDMS device (~1.5 cm) using knife after curing (or) peeling of entire PDMS devices (3 inch)

1.3 Results and discussion

1.3.1 Shrinkage ratio of PDMS

SW Lee et al [29] have shown a complex method for obtaining 2D shrinkage ratio of PDMS at silicon wafer scale (4 inch) (see Figure 1.5a [29]). A schematic view of the protocol used for PDMS shrinkage ratio estimation for our study is shown in Figure 1.5b. It is obtained after alignment of both layers by evaluation of the misalignment ΔD at corners of 150 µm Al pads located at D ~1 cm from each other to improve sensitivity ([D

+ 2ΔD]/D). Table 1.1 shows the results of the shrinkage ratio obtained at a curing temperature of 120 °C for 1 hr.

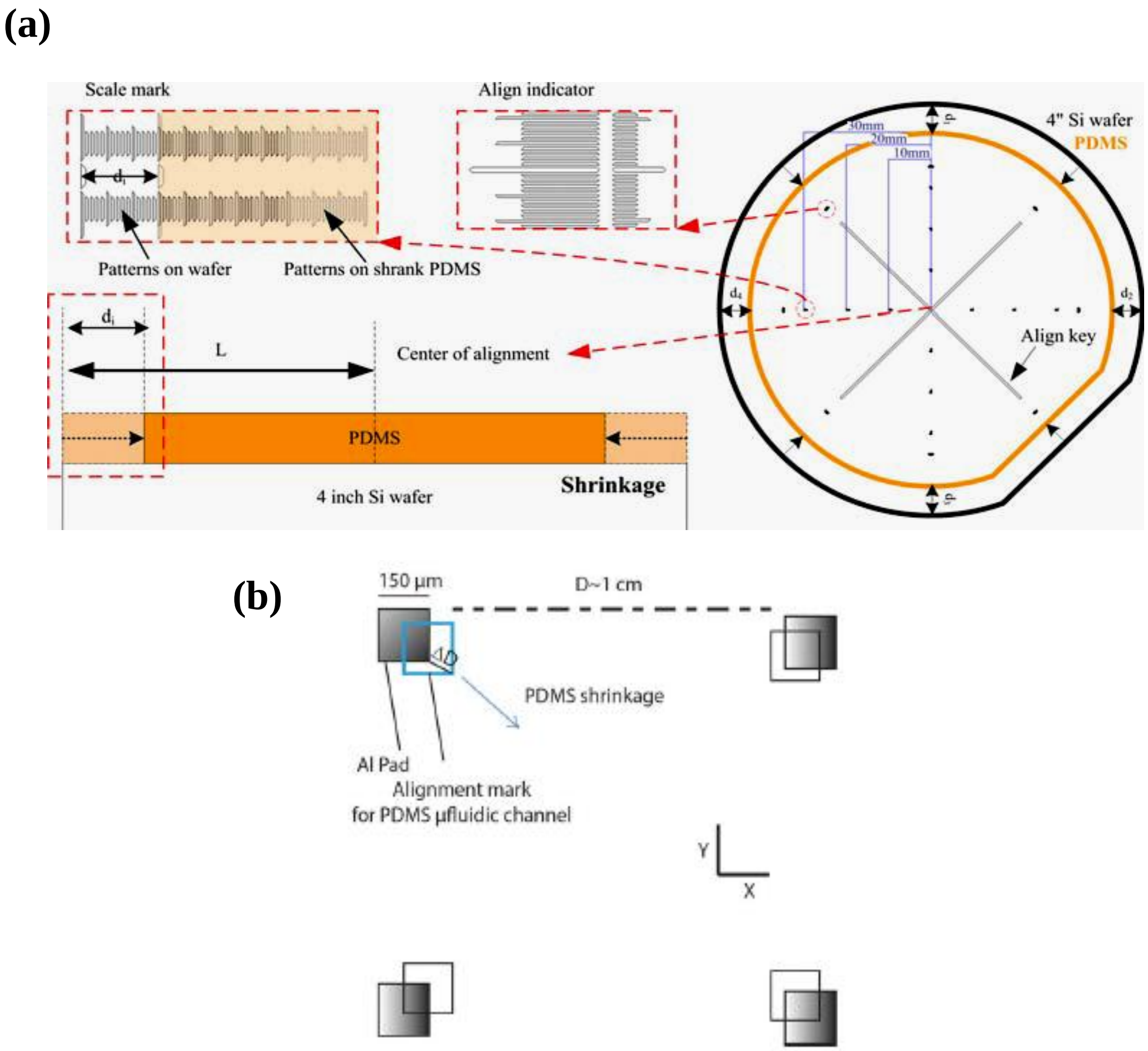

Figure 1.5 (a) schematic view of the measuring method of shrinkage ratio of PDMS (figure adapted from ref [29]) **(b)** Schematic view of the protocol used for shrinkage ratio in our case.

PDMS Thickness	*Curing agent to base ratio*	*Temperature (°C) / time (h)*	*Shrinkage ratio*
200 μm	(3:1)	120/1	1.0223%
200 μm	(10:1)	120/1	1.0263%
1.2[a] mm (ref.29)	(10:1)	100/1	1.94%

Table 1.1 Shrinkage ratios of 200 μm-thick PDMS. [a] An increase in the temperature to 120 °C would have further increased the shrinkage ratio [29].

Interestingly, the shrinkage ratio for our 200 µm thick PDMS layer was only 1.0263% whereas 1.94% was previously reported for 1.2 mm thick PDMS (50% decrease) [29]. The reason why thin, spin coated PDMS has a lower shrinkage ratio might be due to the loss of elasticity after baking on the mold. A reduced shrinkage ratio is surely an advantage for perfect alignment since it implies a reduced sample to sample dispersion. Indeed, no dispersion (less than 1 µm or 1 cm) has been observed with thin PDMS layers. After several iterations, we obtained a ratio of 1.0223%. Such a precise estimation is mandatory for reaching sub - µm misalignment error. This value slightly changes with the curing agent to base ratio (see Table 1.1).

1.3.2 Misalignment error estimation

Misalignment error is obtained from the distance ΔD between the corner of 150 µm aluminum pads and the equivalent pattern on PDMS (Figure1.5). Figure 1.6a and 1.6b show optical microscopy images at different zoom scales of aligned PDMS microfluidic channels (10 mm large) on aluminum electrodes. The average and standard deviation of misalignment error obtained from 36 devices located at 2, 4 and 6 mm from the center are shown in Table 1.2. Close to the center (diameter below 5 mm), alignment and standard deviations, measured with a Leica Microsystem (DM-4000-M), are nearly perfect. These values increase up to 3.6 µm (0.1 µm standard deviation) only in the X direction and at the side of 1.5 cm chips, but remain better than the previously reported misalignment error on silicon (10 µm shown in Figure 1.6c of upper and right align from reference 29) and even on PDMS [28] (1.9 µm with 7.9 µm standard deviation). Further improvement in alignment precision could be obtained by using our alignment tool with a larger optical zoom, but probably misalignment error would be increased far from the center. The misalignment error on the X axis might be due to the non-uniform pressure applied on the PDMS at the bonding stage. Considering the resolution limit of mask patterning for soft lithography, the misalignment range is already highly accurate.

We believe that reproducible sub-micrometric alignment is obtained thanks to the well controlled shrinkage ratio of thin PMDS layers. In usual processes, misalignment occurs just after alignment due to unexpected shock, vibrations and tilt while waiting for the stabilization of the intermolecular bonding. However, with our technique, only a vertical axis displacement was performed for applying pressure and releasing the tool and such an effect has not been observed. The lack of a lubricant is probably the reason.

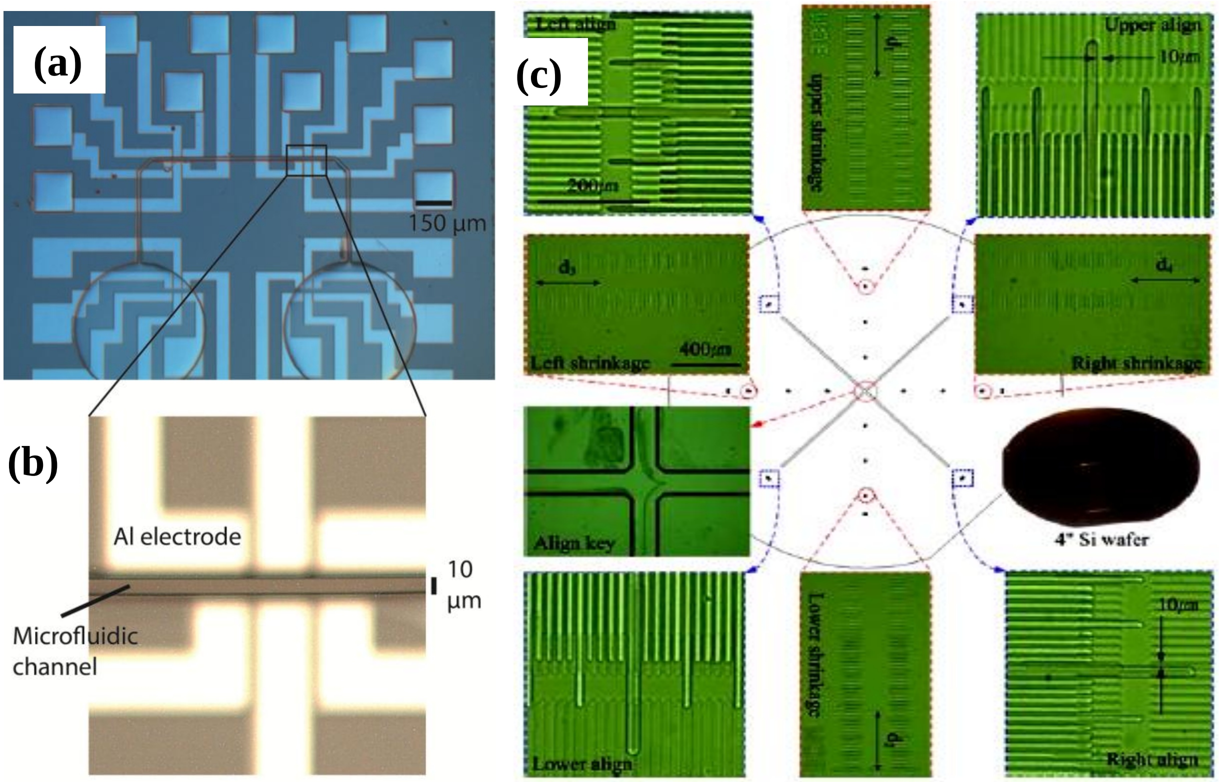

Figure 1.6 **(a)** Optical microscope image of the aligned PDMS microfluidic channel. **(b)** Zoom on Figure a. **(c)** results of alignment between Si and PDMS layer showing misalignment of 10 µm (figure adapted from ref [29]).

PDMS Thickness	*Distance from center*	*2 mm*	*4 mm*	*6 mm*
160 µm	Mean (µm)	0.19	1.66	3.66
	Standard deviation (µm)	0.05	0.12	0.1
350 µm	Mean (µm)	0.32	2.22	4.15
	Standard deviation (µm)	0.03	0.12	0.09

Table 1.2 Mean and standard deviation of PDMS / silicon chip misalignment error.

1.4 Summary

In this chapter, we have shown that thin PDMS layers are of great advantage for precise alignment because shrinkage ratio is reduced by 50% and electrostatic adhesion force is larger than the weight of the PDMS layer. This has been considered for designing a dedicated tool for fast and easy PDMS alignment with high throughput. It will enable the replacement of the resist microbaths [18, 35] aligned on silicon nanosensors with perfectly aligned PDMS microfluidic channels. This technique can also be used for PDMS-PDMS alignment with high accuracy and reproducibility.

Bibliography

[1] Manz A, Graber N, Widmer HM (1990) Miniaturized total chemical analysis systems: a novel concept for chemical sensing. Sensors and Actuators B (1):244 - 248.

[2] Harrison DJ, Fluri K, Seiler K, Fan ZH, Effenhauser CS, Manz A (1993) Micromachining a miniaturized capillary electrophoresis-based chemical analysis system on a chip. Science 261 (5123):895-896.

[3] Wooley AT, Hadley D, Landre P, deMello AJ, Mathies RA, Northrup MA (1996) Functional integration of PCR amplification and capillary electrophoresis in a microfabricated DNA analysis device. Analytical Chemistry 68 (23):4081–4086.

[4] Jacobsen SC, Hergenroder R, Koutny LB, Ramsey JM (1994) Microchip Capillary Electrophoresis with an integrated postcolomn reactor. Analytical Chemistry 66:3472-3476.

[5] Craighead H (2006) Future lab-on-a-chip technologies for interrogating individual molecules. Nature 442:387–393.

[6] Weigl BH, Bardell RL, Cabrera CR (2003) Lab-On-a-Chip for drug development Adv Drug Delivery Rev 55:349–377.

[7] Kurth F, Eyer K, Franco-Obregon A, Dittrich PS (2012) A new mechanobiological era: Microfluidic pathways to apply and sense forces at the cellular level. Curr Opin Chem Biol 16: 400–408.

[8] Leclerc E, Sakai Y, Fujii T (2003) Cell Culture in 3-Dimensional Microfluidic Structure of PDMS (polydimethylsiloxane) Biomedical Microdevices 5 (2):109–114.

[9] Armani D, Liu C, Aluru N (1999) Re-configurable fluid circuits by elastomer micromachining, Orlando, FL

[10] Effenhauser CS, Bruin GJ, Paulus A, Ehrat M (1997) Integrated capillary electrophoresis on flexible silicone microdevices: analysis of DNA restriction fragments and detection of single DNA molecules on microchips. Analytical Chemistry 69 (17):3451–3457.

[11] Seki M, Aoyama R, Hong JW, Fujii T, Endo I (2000) Multiple diagnostic analyses by enzymatic and chemical reaction on a PDMS microchip, Lyon.

[12] Yu M, Wang Q, Patterson JE, Wooley AT (2011) Multilayer Polymer Microchip Capillary Array Electrophoresis Devices with Integrated On-Chip Labeling for High-Throughput Protein Analysis Analytical Chemistry 83 (9):3541–3547.

[13] Thorsen T, Maerkl SJ, Quake SR (2002) Microfluidic Large-Scale Integration Science 298 (5593):580–584.

[14] Gerasopoulos K, McCarthy M, Royston E, Culver JN, Ghodssi R (2008) Nanostructured nickel electrodes using the Tobacco mosaic virus for microbattery applications. Micromech Microeng 18:104003.

[15] Chin LK, Yu JQ, Fu Y, Yu T, Liua AQ, Luo KQ (2011) Production of reactive oxygen species in endothelial cells under different pulsatile shear stresses and glucose concentrations Lab Chip11:1856–1863.

[16] Chin LK, Yu JQ, Fu Y, Yu T, Liu AQ, Luo KQ (2011) Production of reactive oxygen species in endothelial cells under different pulsatile shear stresses and glucose concentrations. Lab Chip 11:1856-1863.

[17] Clément N, Nishiguchi K, Fujiwara A, Vuillaume D (2012) One-by-one trap activation in silicon nanowire transistors. Nature Communications 1:92.

[18] Clément N, Nishiguchi K, Dufrêche JF, Guérin D, Fujiwara A, Vuillaume D (2013) Water Electrolysis and Energy Harvesting with Zero-Dimensional Ion-Sensitive Field-Effect Transistors. Nanolett 13 (8):3903–3908.

[19] Larrieu G, Han XL (2013) Vertical nanowire array-based field effect transistors for ultimate scaling. Nanoscale 5:2437–2441.

[20] Salomon S, Leïchlé T, Dezest D, Seichepine F, Guillon S, Thibault C, Vieu C, Nicu L (2012) Arrays of nanoelectromechanical biosensors functionalized by microcontact printing. Nanotechnology 23:495501–495506.

[21] Grosse A, Grewe M, Fouckhardt H (2001) Deep wet etching of fused silica glass for hollow capillary optical leaky waveguides in microfluidic devices. J Micromech Microeng 11 (3):257–262.

[22] Daridon A, Fascio V, Lichtenberg J, Wutrich R, Langren H, Verpoorte E, de Rooji NF (2001) Multi-layer microfluidic glass chips for microanalytical applications. J Anal Chem 371:261–269.

[23] Howlader MMR, Yamauchi A, Kim TH, Itoh T, Suga T (2004) Wafer Level Surface Activated Bonding Tool for MEMS Packaging. J Electrochem Soc 151(7):G461–G467.

[24] Takagi H, Maeda R (2005) Aligned room-temperature bonding of silicon wafers in vacuum by argon beam surface activation. J Micromech Microeng 15:290–295.

[25] Howlader MMR, Yamauchi A, Suga T (2011) Surface activation-based nanobonding and interconnection at room temperature J Micromech Microeng 21 (2): 025009.

[26] Hosokawa K, Maeda R (2000) A pneumatically-actuated three-way microvalve fabricated with polydimethylsiloxane using the membrane transfer technique. J Micromech Microeng 10:415–420.

[27] http://blogs.rsc.org/chipsandtips/2011/08/17/a-novel-techniquefor-aligning-multiple-microfluidic-devices/.

[28] Mogi K, Fujii T (2013) A novel assembly technique with semi-automatic alignment for PDMS substrates. Lab Chip13:1044-1047.

[29] Lee SW, Lee SS (2008) Shrinkage ratio of PDMS and its alignment method for the wafer level process. Microsystem Technologies 14(2):205-208.

[30] Mogi K, Fuji T (2010) A microfluidic device for stepwise size-based capturing of suspended particles. J Micromech Microeng 20(5):055015.

[31] Fuji T (2002) PDMS-based microfluidic devices for biomedical applications Microelectronic Engineering 61–62:907–914.

[32] Whitesides GM, Abstracts of Papers of the American Chemical Society, 1996, 212, 31-Inor.

[33] Whitesides GM, Ostuni E, Takayama S, Jiang X, Ingber D (2001) Soft lithography in biology and biochemistry. Annu Rev Biomed Eng 3:335–373.

[34] Shantanu Bhattacharya AD, Berg JM, Gangopadhyay S (2005) Studies on surface wettability of poly (dimethyl) siloxane (PDMS) and glass under oxygen-plasma treatment and correlation with bond strength. J Microelectromech Syst14 (3):590– 597.

[35] Clément N, Nishiguchi K, Dufrêche JF, Guérin D, Fujiwara A, Vuillaume D (2011) A silicon nanowire ion-sensitive field-effect transistor with elementary charge sensitivity. Applied Physics Letters 98 (1): 014104.

2

Ultimate Integration of a PDMS based Lab-on-a-Chip with Nanotransistor Biosensors

Lab-on-chip (LoC) technology integrated with heterogeneous components such as electronics and sensors will drive a revolution in medical technology in the years to come. It will enable powerful point-of-care diagnosis and treatment through on-chip sensing, and detection in a cost-effective manner. Biosensors based on field-effect transistors, microelectromechanical resonators, electrochemistry, or radiofrequency have attracted substantial interest for various ionic and biochemical sensing applications.

Improved performance and lower costs of integrated circuits can be achieved by utilizing smaller (nanoscale) device dimensions and larger wafers to increase the number of chips that are processed in parallel. These nanoscale field-effect transistors and electromechanical systems have attracted substantial interest for highly sensitive ionic and biochemical applications [1–11]. Devices with advanced processes, such as zero-dimensional (0D) nanosensors [3, 12, 13], three-dimensional (3D) nanowire arrays [14, 15], and nanoelectromechanical systems coupled to nanofluidics [11] are emerging to enable the further improvement of integration and sensitivity. Although the nanosensors themselves are very small and increasingly complex, coupled electronic and microfluidic devices are typically in the centimeter range [4, 10] which is not optimized for a low-cost process. The primary limitation for these devices is the area required for tubing and electrical contacts, which determines the silicon (Si) area on which the polydimethylsiloxane (PDMS) is bonded.

In addition to reducing size and costs, optimal integration is useful because tiny sensors should require short access leads (i.e., minimal distance between the microfluidic channel and electrical contacts). In this way, these sensors can be operated at the optimal bandwidth for many applications, including enzymatic studies (substrate-enzyme interactions are expected to be up to the mega-Hertz level) [16] or energy harvesting [3]. Although such labs-on-chips (LoCs) could be fabricated with microbaths [3, 12], they are not in the optimal configuration compared to microfluidic channels, which, in turn, are difficult to control (i.e., in terms of the ion concentration in a microdroplet, evaporation, rinsing, etc.).

In this chapter we address the technological and physical limits for the maximal integration of PDMS-based LoCs. The critical distance between the microfluidic channel and the electrical contacts can be reduced to a few tens of micrometers, below which leakage was observed. We demonstrate the fabrication of 1.5 mm × 1.5 mm labs-on-chips, including electrical contacts and tubing. Using these labs-on-chips with zero-dimensional nanotransistor biosensors, we obtained a well-controlled Nernstian response to Na^+, with picoliter-range volumes and a mega-Hertz-range frequency bandwidth. We observed an unexpected possibility for tuning the nanotransistor threshold voltage with the microfluidic channel width, which promises the design of sensors with optimized power consumption. This study concerns a wide range of sensors and LoCs that require electrical contacts close to a microfluidic channel [17–19] and ultimate integration.

2.1 Nanotransistor device fabrication

The nanotransistor biosensors used in this study were fabricated at NTT basic research laboratory, Japan (15 nm diameter and 20 nm long). They operate as single-electron transistors up to liquid nitrogen temperature [20] and as elementary charge-sensitive field-effect transistors at room temperature [21, 22], even in a liquid environment [12]. For these reasons, when these biosensors are operated in liquid, we call them 0D ISFETs or 0D nanotransistor biosensors. The scanning electron micrograph (SEM) and atomic force microscopy (AFM) of 0D nanotransistor is shown in Figure 2.1a and 2.1b respectively.

The 0D ISFETs were fabricated on silicon-on-insulator wafers. A narrow constriction channel, sandwiched between two wider 400-nm channels, was patterned on a 30-nm-thick top Si layer (p-type, boron concentration of 10^{15} cm^{-3}). The length and width of the constriction channel were 35 and 25 nm, respectively. Thermal oxidation was performed at 1100 °C to form a 40-nm-thick SiO_2 layer around the channel. The oxidation process reduced the size of the constriction to about 15 nm, giving final channel dimensions of 20 × 15 nm. Phosphorous ions were implanted 5 µm away from the constriction. A resist mask was used to form highly doped source and drain regions, on which aluminum electrodes were evaporated.

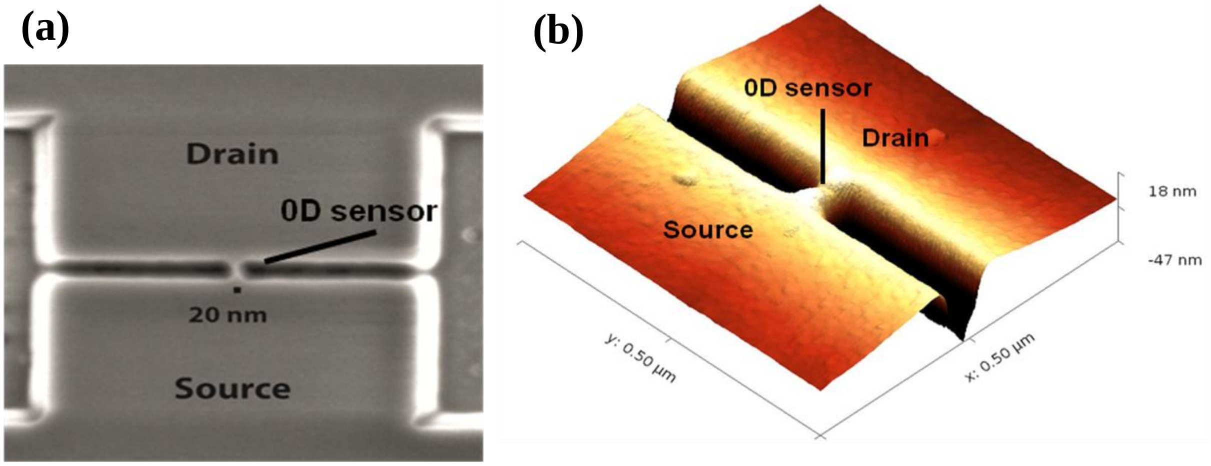

Figure 2.1 (a) Scanning electron micrograph of zero dimensional ion-sensitive field effect transistors **(b)** corresponding atomic force microscopic image.

2.2 Fabrication of PDMS-based millimeter-scale lab-on-chip

2.2.1 General approach

Figure 2.2a shows schematic view of a typical structure for a PDMS-based LoC with nanotransistor biosensors. In our case the LoC would be composed of a patterned Si wafer with 0D nanotransistor biosensors. A PDMS layer, including holes for tubes and microfluidic channels, can be aligned on top of the Si nanotransistor and thermally bonded to the Si wafer.

However, it is extremely difficult to achieve the precise cutting and alignment of a millimeter block of PDMS with an error of a few micrometers. Decreasing the LoC dimensions from the centimeter to the millimeter range through the parallel fabrication of many independent chips required us to use the smallest available tubes and to rethink the entire fabrication process. Our approach is shown in Figure 2.2b. A thin layer of PDMS (PDMS1: thickness 200 µm) was required for the alignment protocol (as previously discussed in chapter 1) and for precisely defining the holes for tubing and electrical contacts close to the microfluidic channel.

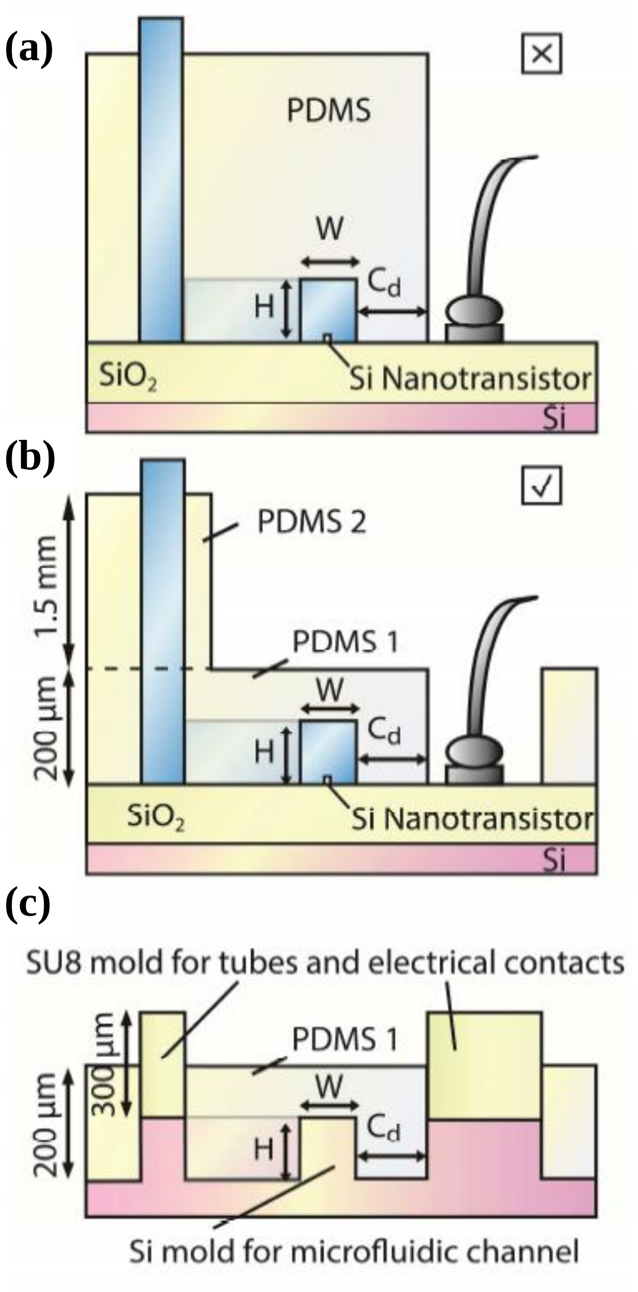

Figure 2.2 (a) Schematic view of a typical PDMS-based LoC with nanotransistor biosensors. Distance C_d between the microfluidic channel and electrical contacts is usually in the millimeter range. **(b)** Schematic view of the proposed approach composed of two layers of PDMS (PDMS1 and PDMS2). This approach allows perfect alignment (precision ± 1 µm) of the microfluidic channel (shown in chapter 1) and a decrease of C_d to a few tens of micrometers. **(c)** Schematic

view of the mold used to fabricate PDMS1. A Si mold is used for the microfluidic channels and a SU8 mold for the electrical contacts and tubing.

2.3 Making holes in PDMS close to the microfluidic channel: drawbacks of conventional and other previously published techniques

2.3.1 Punching method

Precise uniform punching of PDMS1 close to the microfluidic channel (~20 µm error precision required) is extremely difficult even with a 0.33 mm (ID) needle (see Figure 2.3a). Figure 2.3b shows that, although successful, there is a large risk of leakage (PDMS wall below the 60 µm critical distance) due to non-uniformity in PDMS wall. In addition, the time taken for punching all 36 identical LoCs requires minimum 8 hr (20 min for each independent: see Figure 2.6d for more details) as it is a serial process. This sometimes further lead to poor bonding of PDMS1 on Si even after 30 min of UV ozone treatment due to PDMS pollution during the long processing time. Because of the long serial process and the lack of reliability, we didn't further consider this technique.

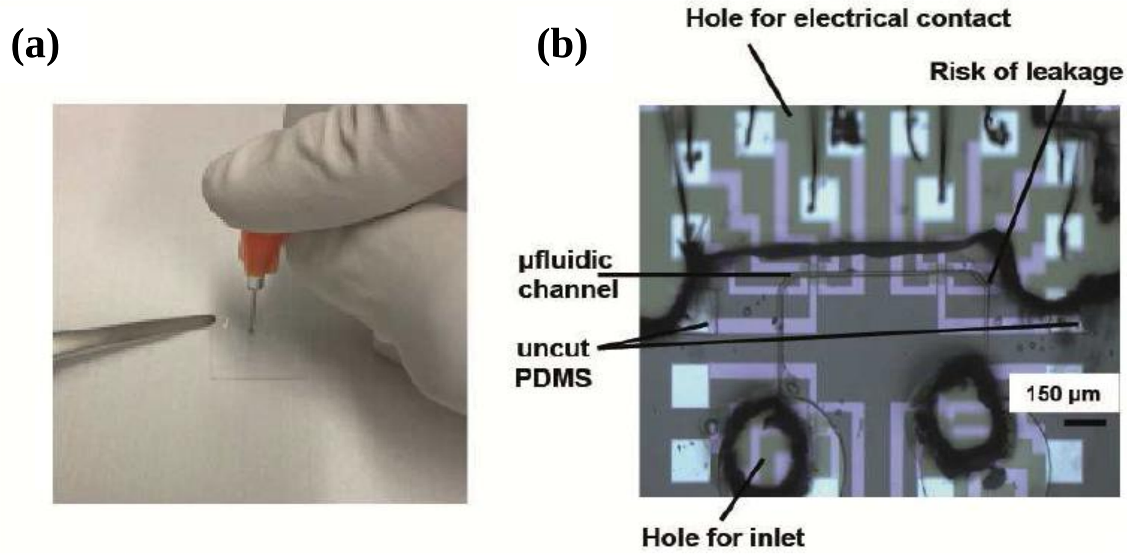

Figure 2.3 (a) Optical picture showing punching of the PDMS1 device with a 0.33 mm (ID) needle. **(b)** Optical microscopic image of the bonded PDMS1 prepared by punching method on the Si nanotransistor biosensor chip. The precision is not enough with this technique. Either PDMS is not perfectly cut on electrical pads or holes for electrical contacts are below the 60 µm critical distance to the microfluidic channel (risk of leakage).

2.3.2 Plasma etching method

Figure 2.4a showing the steps for optical lithography to deposit gold by electron beam evaporation before and after plasma etching of PDMS1. Dry etching of PDMS1 was performed by reactive ion etching in CF_4 / O_2 (37:13 sccm), 150 W, and 150 mT [43] after depositing a gold mask of 100 nm thickness (optical picture shown in Figure 2.4b). We measured a similar etching rate of 20 $\mu m.h^{-1}$ as in [23], leading to a total time of 10 hr plasma etching. However, we noticed simultaneously extensive metal mask etching and non-uniform PDMS etching (see Figure 2.4c). As a consequence, to make holes in a 200 µm-thick PDMS1 layer, multiple photolithographic and etching cycles are required. As a result the surface roughness of the PDMS1 layer becomes poor which is not good to bond the PDMS2 for tubing. Because of the long processing time, the number of lithography and metallization steps, and the unsatisfying final result, we didn't further consider this technique.

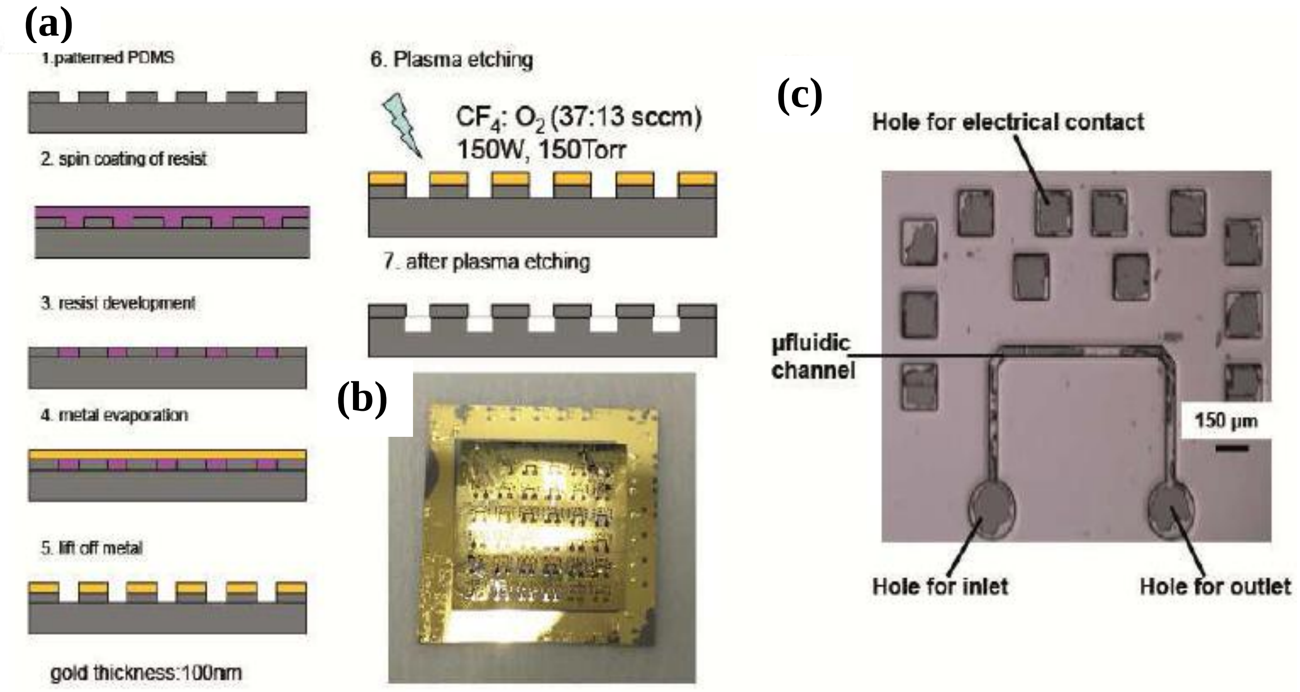

Figure 2.4 (a) Schematics showing optical lithography steps made on patterned PDMS for gold deposition and dry etching with CF_4 / O_2 precursors following the protocol from ref [23]. **(b)** Optical picture showing gold evaporated PDMS1 after metal liftoff. **(c)** Optical microscopy image showing non-uniform PDMS1 layer etching after dry plasma technique.

2.3.3 Two layers mold with 50 µm-thick PDMS

A schematic presentation of the process proposed in [24] is shown in Figure. 2.5a. A two-layer SU8 mold (Shipley) is used to define both microfluidic channels (thin layer) and holes (50 µm-thick layer) in PDMS. Once the mold is done, this technique has the great advantage to be a parallel and reproducible process. However, it requires the use of a very thin PDMS layer (<50 µm) that we found to be too easily deformed and insufficiently robust (easily torn or cut while demolding, see Figure 2.5b), In addition, the PDMS shrinkage ratio during curing has to be considered with extreme precision to reach 1µm alignment precision (as discussed in chapter 1), which is not possible with such thin layer. Given the potential advantages of this parallel technique, we further developed this technique for our application and make it compatible with 200 µm-thick PDMS.

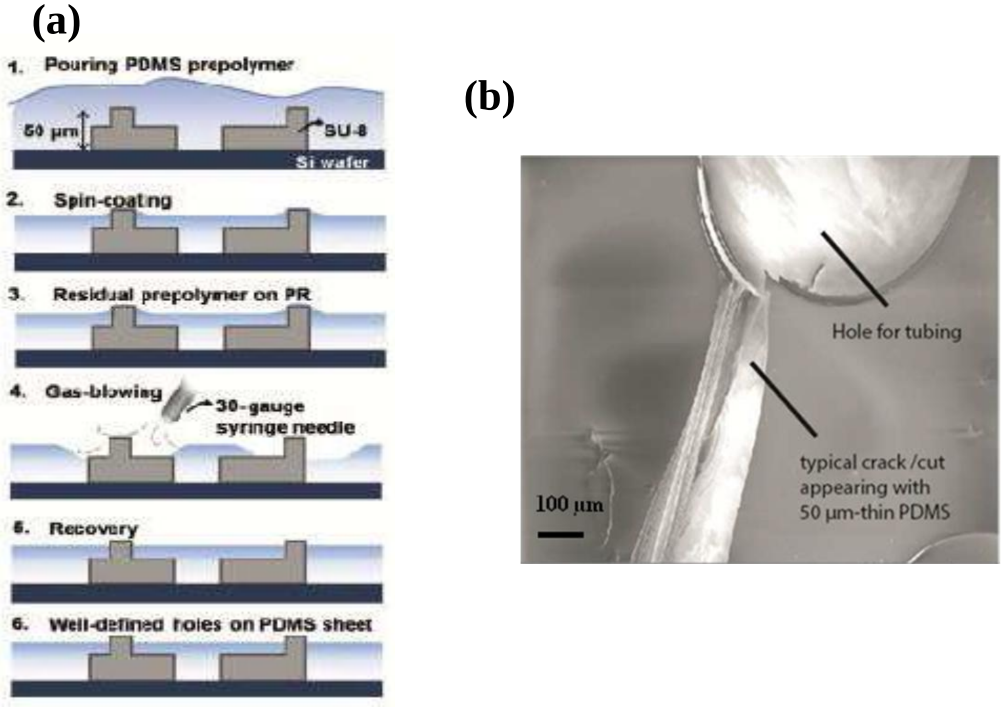

Figure 2.5 (a) Schematics showing the fabrication process for PDMS through-hole membrane using photoresist mold by two step lithography (from ref [44]) **(b)** SEM picture of 50 µm thick PDMS1 showing the cut at the inlet hole after demolding from Si/SU8 mold

2.3.4 Selected approach: 344 µm-thick 2 layers mold with 200 µm-thick PDMS

We adapted the previously reported [24] all-SU8 two-level mold as in the Figure 2.5a, by using a hybrid Si/SU8 mold (see Figure 2.6a) with a very thick second layer. The silicon mold (1st layer, 44 micrometers-thick) is used to provide extremely flat microfluidic channels and to allow a good adhesion of the 2nd layer (as discussed in Chapter 1). A 300-µm-thick layer of SU8 resist was necessary to define holes precisely in the 200 µm-thick PDMS layer. To promote good adhesion between SU8 and Si, we used one layer of SU8

2002 followed by one of SU8 2075. Given the unusual SU8 thickness required for this application, annealing should be performed with at least 1 hr ramps to avoid sole surface baking (the two annealing steps are 65 °C for 30 min and 95 °C for 4 hr for both pre- and post- exposure). As the SU8 remains too sticky for optical lithography, we recommend letting the mold dry for two days at room temperature before exposure for 50s in proximity mode. We recommend to avoid agitation for the development (typically 10h with solution changed at least once) and to perform hard baking at 190°C during 3h with 3h ramps to solidify the structure. The mold was covered with a 2-µm-thick layer of C_4F_8 by passivation at a gas flow rate of 220 standard cm^2 / m and a coil power of 1000 W for 60 sec before use. The 344-µm-thick Si/SU8 layer was sufficiently large to fabricate the holes. The optical picture of the entire 3inch Si/SU8 mold and zoomed in of 1.5cm X 1.5cm of the mold is shown in Figure 2.6c and Figure 2.6b respectively.

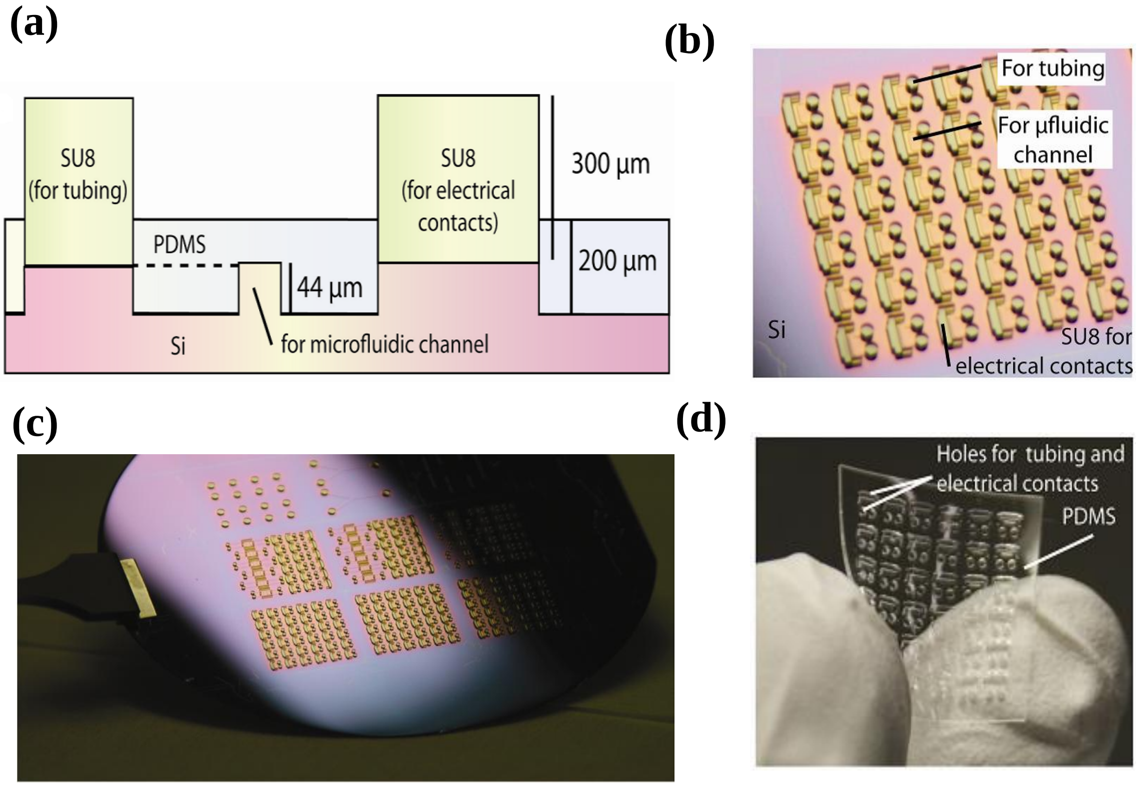

Figure 2.6 (a) Schematic view of the mold used to fabricate PDMS1 same as Figure 2.2c **(b)** Zoom in optical microscopic image of 1.5 mm x 1.5 mm of the mold **(c)** Optical picture of two level Si/SU8 mold **(d)** Optical picture of 200 µm thick 1.4 cm x 1.4 cm PDMS1 with holes for electrical contacts and tubing. It contains 36 independent 1.5 mm x1.5 mm LoCs together.

The ratio of PDMS curing agent to base was changed from 1:10 (standard) to 1:3, to make PDMS1 sufficiently dense for easy manipulation. The uncured PDMS was spin-coated at 300 rpm for 30 s, with an acceleration rate of 100 rpm/s to obtain 200 µm-thick

PDMS1 layer. After spin coating the residual PDMS (see the SEM picture of Figure 2.7a and 2.7b) on the SU8 pattern can be easily removed by blowing with nitrogen gun connected to a syringe nozzle. The PDMS was then cured in two steps: (i) at 65 °C for 20 min in contact with a hot plate, and (ii) in a convection oven at 120 °C for 40 min. Subjected to separation of PDMS layer from the Si mold is done after removing from the oven and cooled down to room temperature. Figure 2.6d shows the optical picture of 1.5cm X 1.5 cm, PDMS1 (200 µm thick) layer with holes for electrical contacts and tubing. A second layer of PDMS (PDMS2, 2 mm in thickness) was used to guide the tube and reduce the mechanical stress at the inlet and outlet.

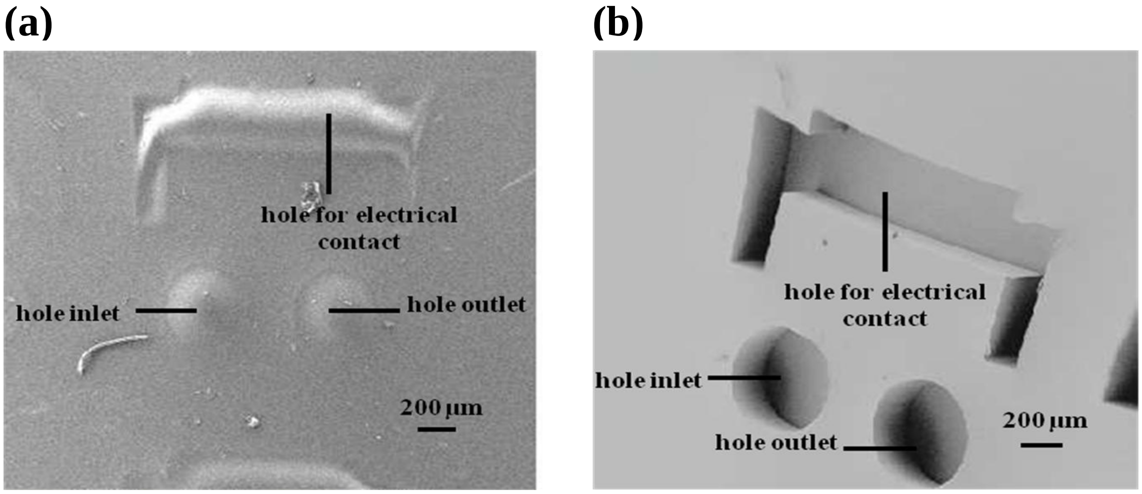

Figure 2.7 (a) SEM picture showing the 200 µm-thick PDMS1 just after demolding from the 2 levels mold. A very thin layer of PDMS remains but can easily be removed from blowing or using a needle after which holes extremely well defined **(b)**

2.4. Alignment and Bonding

Before bonding, the Si chip and PDMS1 were exposed to plasma O_2 at 120 W and 0.7 mbar for 180 s and to UV-ozone for 5 min. After proper alignment and bonding with 1-µm alignment precision (as discussed in chapter1), thermal annealing was performed at 120 °C for 60 min to make permanent bonding. The covered Si wafer was cut into independent LoCs, each measuring 1.5 mm × 1.5 mm. Access holes for connecting the inlet and outlet tubes (PTFE tubing: 0.7 mm/0.3 mm outer diameter [OD]/inner diameter [ID]) were cored into the 2-mm-thick bare PDMS2 by using a 330-µm-ID needle, with an approximate distance between the two holes of less than 1 mm. The plane of PDMS2 was sealed to the plane of PDMS1 under an optical microscope, with uncured PDMS being used as glue.

Figure 2.8a shows schematic view of 1.5 mm x 1.5 mm LoC with PDMS1 showing the Critical distance (C_d) and PDMS2 with tubings for inlet and outlet. One of these chips is shown in Figure. 2.8b after alignment of the first PDMS layer (PDMS1; W = 10 µm) on the Si chip nanotransistor biosensors.

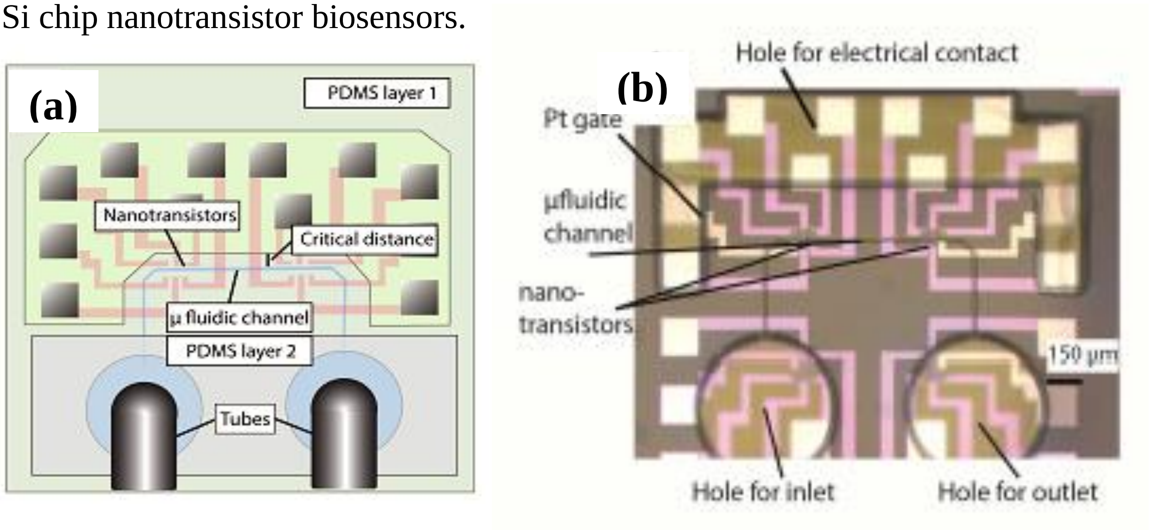

Figure 2.8 (a) Schematic view of 1.5 mm x 1.5 mm LoC with PDMS1 showing the C_d and PDMS2 with tubings for inlet and outlet **(b)** Optical microscopic image of the bonded PDMS1 on silicon nanotransistor biosensor chip.

Holes for electrical contacts are located 150 µm away from the microfluidic channel. The chip width is typically one order of magnitude below that of other equivalent PDMS LoC sensors [2, 4, 6 and 14]. Figure 2.9a showing optical zoomed-in image on Figure 2.8b to show clearly the aligned 10 µm microfluidic channel on 0D nanotransistor biosensors and Figure 2.9b shows picture of packaged 1.5 mm X 1.5 mm independent LoC with wire bonding and tubes connecting the inlet and the outlet.

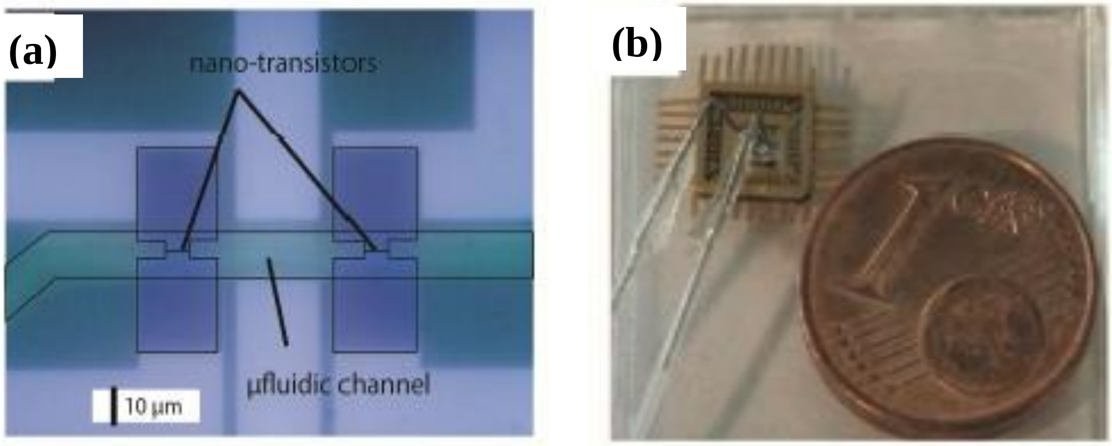

Figure 2.9 (a) Zoom on Figure 2.8b to show aligned 10 µm width microfluidic channel on the 0D ISFETs. **(b)** Picture of the packaged 1.5 mm x 1.5 mm chip.

2.5 Results and discussion

2.5.1 Technological and physical limits for ultimate integration

A major challenge in the ultimately scaled microfluidic system is the leakage due to increased flow rate which is directly proportional to the pressure drop inside the microfluidic channel, so there is always a need to choose the defined PDMS wall distance from the microfluidic channel to the closest contact pads. Leakage due to deformation demonstrated to be an important consideration in low aspect ratio (height to width) channels, and the effect of channel deformation becomes important in a number of common microfluidic applications.

For instance to measure the PDMS deformation, first Hosokawa et al. presented a method for local pressure monitoring in microfluidic devices using a deformable diffraction grating but they did not provide the magnitude of channel deformation with respect to the imposed flow rate [25]. In another work, Holden and his colleagues experimentally determined the bulk PDMS deformation under high pressure by utilizing the variation in fluorescence intensity with channel bulging [26]. They measured the change of PDMS microchannel cross-section as a function of flow rate. Later, Gervais et al., found that PDMS deformation is a very important performance issue in low aspect ratio channels [27]. To quantify the deformation of microchannels under pressure-driven flows, Hardy and his colleagues presented a method that used fluorescence microscopy [28]. They found that the pressure drop decreased up to 35% less than the pressure drop in a rigid wall microchannel and they figured out that as wall thickness decreased, this effect was magnified. Recently, Sollier et al. employed fluorescence microscopy to measure PDMS channel deformation. They found that the PDMS channel deformation is significant in both X and Y directions even at low flow rate, which leads to channel cross-sections higher and wider than expected [29].

To overcome all these challenges, hence in this work we introduce the key parameter of finite PDMS wall distance between the microfluidic channel and the electrical contacts (critical distance C_d) to reach higher integration. Critical pressure study performed for PDMS based microfluidic channels with “infinite” walls have shown that it scales inversely with channel width [30]. As a consequence, no leakage is expected under normal operation condition for channel width below 200 µm. Here we show that, for PDMS walls below 50 µm, critical pressure barely depends on channel width, but wall dimension is the relevant parameter.

The key parameter for ultimate integration requires knowing the smallest distance C_d (Figure 2.2) between the microfluidic channel (width W, height H) and the holes for the electrical contacts. The bonding strength (~1.5 J/m²) and the critical pressure (P_c) to reach PDMS debonding were previously evaluated for a full PDMS layer (no hole: $C_d \sim \infty$) and small microchannel aspect ratio (H << W) [29]. In that case, P_c scaled as $1/W^{3/2}$. Under classical microfluidic operating conditions (liquid flow rate < 100 µL/min), P_c could not be reached in a PDMS microfluidic channel smaller than W = 200 µm that was thermally bonded to a Si substrate.

In our experimental system, we could define a finite PDMS wall with holes for electrical contacts located at a distance C_d from the microfluidic channel (Figure 2.2b and 2.10a, 2.10b), which was tuned from 5 to 200 µm. As it was not straight forward to fabricate precisely such thin PDMS walls, we detailed the fabrication process and the unsuccessful tested approaches above. The inlet pressure was progressively increased until P_c was reached. As the thin PDMS wall was only located at the median part of the pipe (Figure 2.5a), P_c was considered to be half of the pressure drop in the pipe just before leakage appeared. Leakage was easily observed under an optical microscope (Figure 2.10b). Results for a 44-µm-thick microfluidic channel are shown in Figure 2.10c. The presence of a very thin PDMS wall drastically reduced the P_c, which strongly depended on C_d. At C_d > 60 µm, P_c was not achieved up to a flow rate of 1300 µL/min (e.g., there was no PDMS debonding or leakage). The microfluidic channel width dependence was relatively weak. As a first-order approximation, P_c scaled as C_d.

The shear modulus or modulus of rigidity, denoted as µ and equal to 250 kPa for PDMS [31], can be considered as the ratio of shear stress to shear strain (Figure 2.5c, inset):

$$\mu = \frac{F/(y.C_d)}{Z_d/H} \qquad \text{Eq (2.1)}$$

Where F is the lateral force applied on the wall, $F/(y.C_d)$ is the shear stress, and Z_d/H is the shear strain. Assuming that Z_d corresponds to the critical PDMS wall displacement before debonding, we can derive:

$$P_c = C_d Z_d \mu / H^2 \qquad \text{Eq (2.2)}$$

Where $P_c = F/(H.y)$ and H is the microfluidic channel height. This simple equation summarizes the basic physics involved (i.e., shear stress is applied to a hyperelastic material, in a manner similar to pneumatic valves) [32]. From Figure2.10c, P_c varies linearly with C_d, and has almost no dependence with W, in agreement with Eq.2. Fits provided $Z_d \sim 4 \pm 1$ µm, a reasonable value for wall deformation. This equation remained

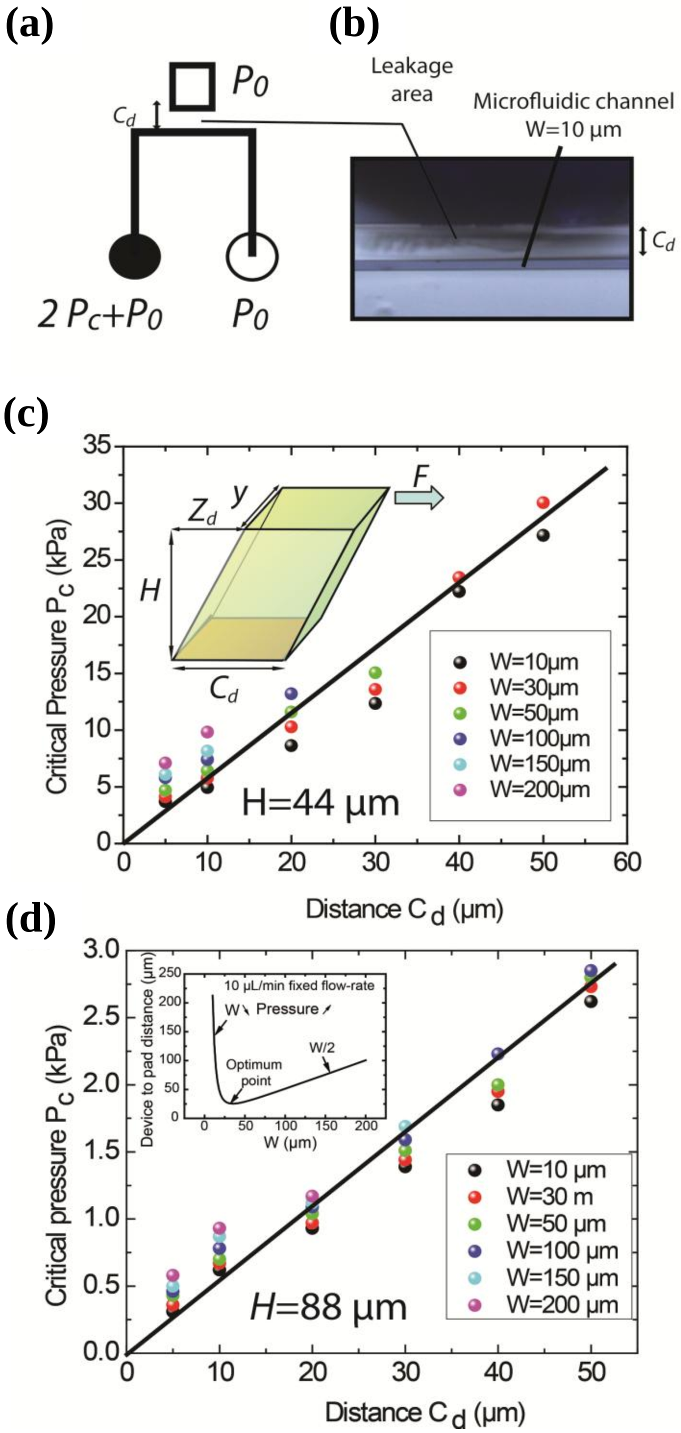

Figure 2.10 (a) Schematic view of the experimental setup used for setting up the critical pressure P_c as a function of C_d. An electrical contact hole at atmospheric pressure P_0 is located at a distance C_d (range: 5-200 µm) from the microfluidic channel. **(b)** Optical microscope image of the experimental setup after leakage. **(c)** Experimental results of P_c (pressure just before PDMS debonding and fluid leakage) as a function of C_d for different channel widths (H = 44 µm). Inset: Schematic view of the PDMS wall deformation under shear stress used to derive Eq 2.1. Debonding area is in orange. **(d)** same as (c), but with H = 88 µm.

valid with $Z_d \sim 2 \pm 1$ µm by changing H from 44 to 88 µm (see Figure 2.10d). For optimal integration ensuring a functional device and normal operation conditions, for example a flow-rate of 10 µL/min (corresponding to 1 min rinsing time of a 15 cm-long PTFE tube with 300 µm inner diameter), there is an optimum value of W to minimize the device to electrical pad distance C_d (W)+W/2 shown in Figure 2.10d, inset. Indeed, at a given flow rate, the pressure is larger in microfluidic channels with small W, but on the other hand the microfluidic channel itself consumes space. An optimal configuration could be W=30 µm and C_d=11 µm, leading to a device to pad distance of 26 µm. Below, we consider a device to pad distance of 200 µm for demonstration of a functional device with ultimate integration with W varying from 10 µm to 200 µm (W=10 µm requires the largest device to pad distance as shown in Figure 2.10d, inset).

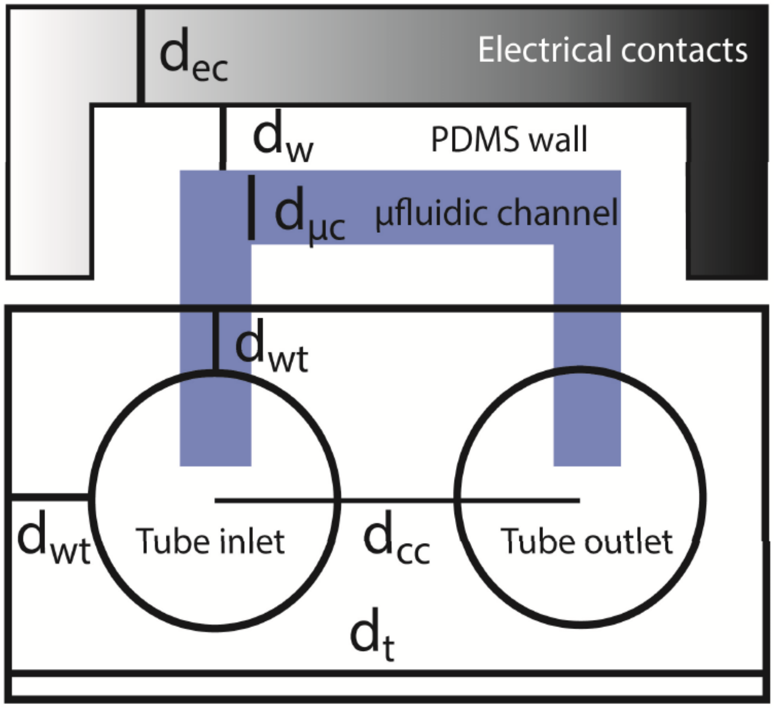

Figure 2.11 Schematic view of the Lab-On-Chip with the distances to be optimized (d_{ec}, d_w, $d_{\mu c}$, d_{wt}, d_{cc}) for ultimate integration.

The ultimate integration is not only related to the microfluidic channel width and its distance to electrical contacts. It includes tubes diameter, the choice of architecture, electrical pads area. We believe that we have optimized the actual structure. Figure 2.11 shows schematic view of the LoC with the distances to be optimized are distance of the electrical contact pads (d_{ec}), distance of the PDMS1 wall near the electrical contacts (d_w), distance of the microfluidic channel ($d_{\mu c}$), distance of PDMS2 wall and the tube (d_{wt}) and distance from the centre of tube inlet to the tube outlet (d_{cc}) for ultimate integration. A configuration with a direct connection of the microfluidic channel between tube inlets and outlets may further lead to a gain in integration. However it is of importance to be able to observe the microfluidic channel and to keep a distance between microfluidic channel and electrical contacts as small as possible (it is difficult to control d_{wt} with µm precision). The main gain in integration may come from reduced commercially available microfluidic tubes in the future. The minimum distance between tubes is also the critical distance ($C_d > 50$ µm). d_{ec} may be reduced down to 50 µm.

2.5.2 Impact of ultimate integration on 0D ISFETs electrical characteristics

2.5.1.1 Picoliter-range droplets in microfluidic channels

Microdroplets offer the feasibility of handling miniature volumes of fluids conveniently, which are suitable for high-throughput measurements. We developed a simple methodology to handle picoliter volumes of analytes inside the microfluidic system with a 10-µm channel width. Discrete volumes of analyte were drawn into the PTFE tube (0.7 mm/0.3 mm OD/ID) by hand with the help of a syringe. The tube was connected to syringe pump (working flow rate limit of 0.1 µL/min, which was the limit of our system), which was used to pump liquid into the microfluidic channel through the inlet. Liquid flow was monitored continuously under the optical microscope. Liquid volume was calculated by considering the length of the droplet inside the channel (~920 µm in Figure 2.12) and the channel dimensions (44 µm × 10 µm). Once the desired droplet with known volume had covered the entire device for the I-V measurement study, the inlet pressure was released, to avoid further movement of the liquid droplet inside the channel.

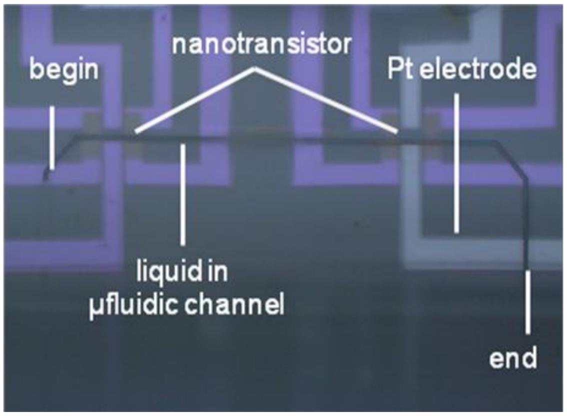

Figure 2.12 Optical micrograph showing 400pL NaCl inside the 10 µm microfluidic channel

2.5.1.2 Ions sensitivity with picoLiter (pL) range volumes

A straightforward advantage of ultimate integration is the possibility of reducing the analyte volume. For clinical diagnosis, using smaller blood volumes minimizes the invasiveness of sample-drawing procedures for patients and reduces blood loss, which is particularly important in geriatric and neonatal patients. In addition, costs are substantially reduced with reduced reagent consumption. Below, we demonstrate the ability of the device to operate with picoliter volumes, focusing on the impact of ionic strength on the electrical response of nanotransistor biosensors.

The role of salt on the transistor properties must be clearly addressed because these biosensors are operated in buffer solutions. The impact of salt on the threshold voltage V_T of a transistor at constant pH is still under debate [3, 4, 12, 34], except for the impact of salt on the Debye screening length L_d (i.e., sensitivity to biomolecules is decreased at large ionic strength e.g., small L_d) [33]. More recently, there have been attempts to detect ions other than protons using miniaturized ISFETs (carbon nanotubes [35], graphene [36], and nanowires [3, 4, 12, 34], which are promising candidates for sensing application) coated with an oxide interface, however with diverging results. Nikolaides et al [37] and Park et al [38] reported a weak non-linear change of the FET resistance upon changing the ion concentration of a KCl and NaCl solution respectively. Using thiol substituted gold films on silicon nanowires with high dielectric constant gate oxide layers (e.g., Al_2O_3 or HfO_2) showed selective Na^+ response of 44mV/dec in NaCl solution and not to H^+, K^+ and Cl^- ionic species [39]. Using 0D ISFETs without a coating layer (e.g., of Si_3N_4 or metal oxide), showing full Nernstian response to NaCl (i.e., slope ~ 60 mV/decade of NaCl concentration) [3, 12] has been discussed. A large dispersion in transistor V_T was obtained, which was attributed to the difficulty of precisely controlling the ion concentration in a 0.5 µL microdroplet [3,12] inside an SU8 microbath (500 µm × 750 µm) fabricated on top of the nanotransistor (no microfluidic channel: see Figure 2.13e for more details).

We expect that using PDMS-based microfluidic channels will suppress the dispersion in ion concentration due to microdroplet evaporation. A schematic view of the device used for electrical measurements is shown in Figure 2.13a. The device includes, on a 1.5 mm × 1.5 mm chip, 0D ISFETs, microfluidic channels with an inlet and outlet, a Pt electrode for liquid gating (The use of a conventional reference electrode limits seriously the application of ISFETs with respect to the small size. Therefore the development of a

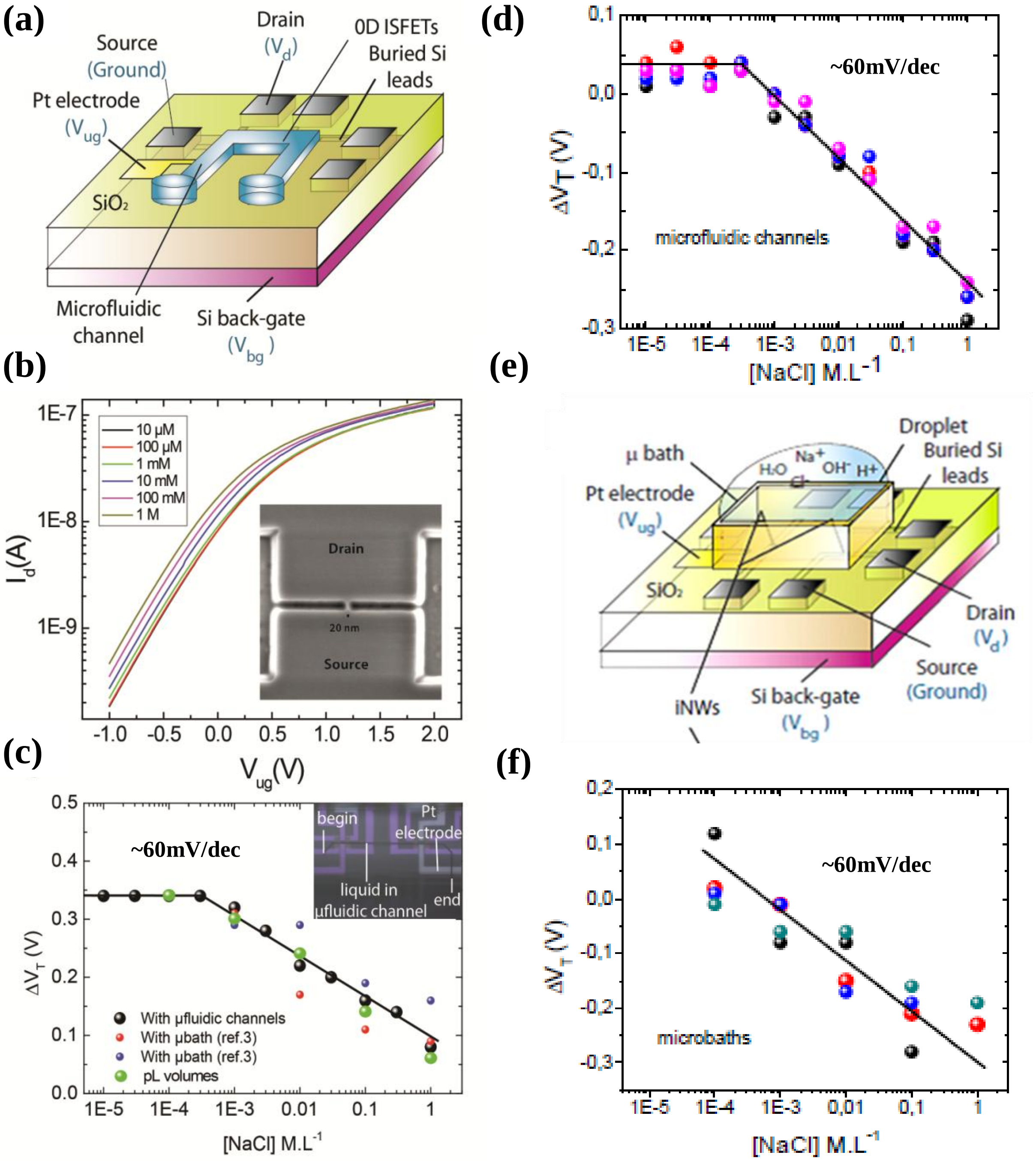

Figure 2.13 **(a)** Schematic view of the electronic connections related to the 0D ISFETs. **(b)** Drain current I_d vs. liquid-gate voltage V_{ug} at different NaCl concentration. V_d = 50 mV, V_s = V_{bg} = 0 V. Inset: scanning electron microscope image of the 0D ISFET (silicon nanowire dimensions: diameter 15 nm, length: 25 nm) **(c)** Variation of the threshold voltage V_T as a function of NaCl concentration at constant pH for the ultimately integrated LoC with PDMS microfluidic channels (black balls for continuous flow and green balls for 400 pL volume) and for microbaths (blue and red balls from ref [3]). Inset: optical microscope image showing the 400 pL NaCl inside the microfluidic channel. **(d)** Variation of 0D ISFET's threshold voltage as a function of [NaCl] for 4 different devices in microfluidic channel and **(e)** Schematic figure of

SU8 microbath on 0D ISFET adapted from reference [12] **(f)** Variation of 0D ISFET's threshold voltage as a function of [NaCl] for microbath.

miniature reference electrode made with the IC-compatible technology is of great interest for the wide-spread use of these sensors), source and drain nanotransistor contacts (four identical nanotransistors are measured simultaneously), and a Si back gate, which can be used to tune the V_T of these nanotransistors (connected to ground).

Figure 2.13b shows the drain current vs. liquid gate voltage I_d-V_{ug} curves for one nanotransistor at different NaCl concentrations and constant pH (5.8 ± 0.2). Variations in the threshold voltage ΔV_T of 0D ISFETs as a function of NaCl concentration were extracted from these curves and plotted in Figure 2.13c. For comparison, data obtained with microbaths (from ref. 3) were added to the graph. We observed a plateau in ΔV_T values at NaCl concentrations below 100 µM and a Nernstian response at NaCl concentrations above 100 µM (slope ~60 mV/dec). This sensing response did not depend on the microfluidic channel widths (see Figure 2.13d).

One advantage of this approach is that using microfluidic channels substantially reduces the average V_T deviation to a linear fit (14.8 mV compared to 36.8 mV for microbaths: see Figure 2.13d and Figure 2.13f), with similar device-to-device V_T dispersion in the microfluidic channel configuration. The remaining dispersion may be an inherent feature of these tiny devices, which have extremely high charge sensitivity in liquid [12]. With a gate capacitor of ~3 aF, a fluctuation of 0.3 elementary charges induced a 15 mV V_T shift. The ion organization in liquid may fluctuate in the position near the very small 20-nm-long transistor. Parallelization of these devices should reduce these fluctuations as the inverse of the number of transistors [40].

A second advantage of the microfluidic channels is that the solution can be changed under continuous flow, without evaporation. This ability increases the number of concentrations that can be measured (with small microbaths, only an order-of-magnitude increase in ion concentration after complete evaporation of previous droplets can ensure a 10% error in ionic strength).

A third advantage of the microfluidic channels is that it is possible to study extremely small volumes. The only limitations to this advantage are the alignment precision of a microfluidic channel on the nanotransistors as well as the distance between the Pt electrode and nanotransistors (liquid should connect both). However, using a 10 µm wide microfluidic channel with 1 µm alignment precision (as discussed in Chapter1) and 150 µm between the Pt gate and the transistor, we could achieve measurements between 200 pL and 600 pL (see Figure 2.13c and Section 2.5.1). In this figure, the sensitivity to NaCl at such small volumes is demonstrated without an increase in the average deviation in V_T (14 mV). This advantage promises great possibilities when these devices are coupled to nanoliter-volume droplets fabricated by digital microfluidics [41–43].

Using microfluidic channels, we reproduced our claim of a Nernstian response to NaCl with uncoated 0D ISFETs [12]. The shift of V_T to lower values with increased NaCl concentration is consistent with the adsorption of Na^+ ions at the SiO_2 interface, whereas Cl^- complexation was suggested in [4]. We will discuss this observation further in a next Chapter.

2.5.3 Impact of microfluidic channel width on the nanotransistors frequency bandwidth

Silicon nanowire (SiNW) devices have attracted increasing attention during the past decade due to their unique capability of probing chemical and biological species, being able to directly determine the binding status of these efficient molecular detectors through some form of electronic readout which has become an active research area for LoC applications.

The mechanism of sensing is based on the changes of sensor conductance in response to the specific binding of (bio) chemical molecules to the sensor inducing a potential change on the gate oxide surface. The detection limit of such sensors is constantly being improved by miniaturizing the dimensions of the nanowires, which results in an increase of the sensor surface control over the nanochannel current. Therefore 0D nanotransistor are perfect candidates for the development of highly sensitive, selective, and label-free sensors for the real time detection of (bio) chemical species. However, when an external charge is in close proximity to the surface of the nanowire, it modifies the charge carrier distribution in the channel, which in turn substantially affects the electrical properties such as conductance and capacitance. Several approaches are therefore used to overcome this problem in nanoscale devices like improving the quality of the device surfaces [44, 45] using frequency domain detection [46] and optimizing the operating regime of the device. Here also, we describe using nanowire biosensors in the frequency domain that can improve sensitivity for detecting biomolecules [45] or pH [47], and enables energy-harvesting applications [3]. Frequency bandwidth is limited by the nanowire length (resistance) and by parasitic capacitances related to access leads and the liquid gate/source. Figure 2.14a (a zoomed version of Figure 2.9a) shows the overlap area

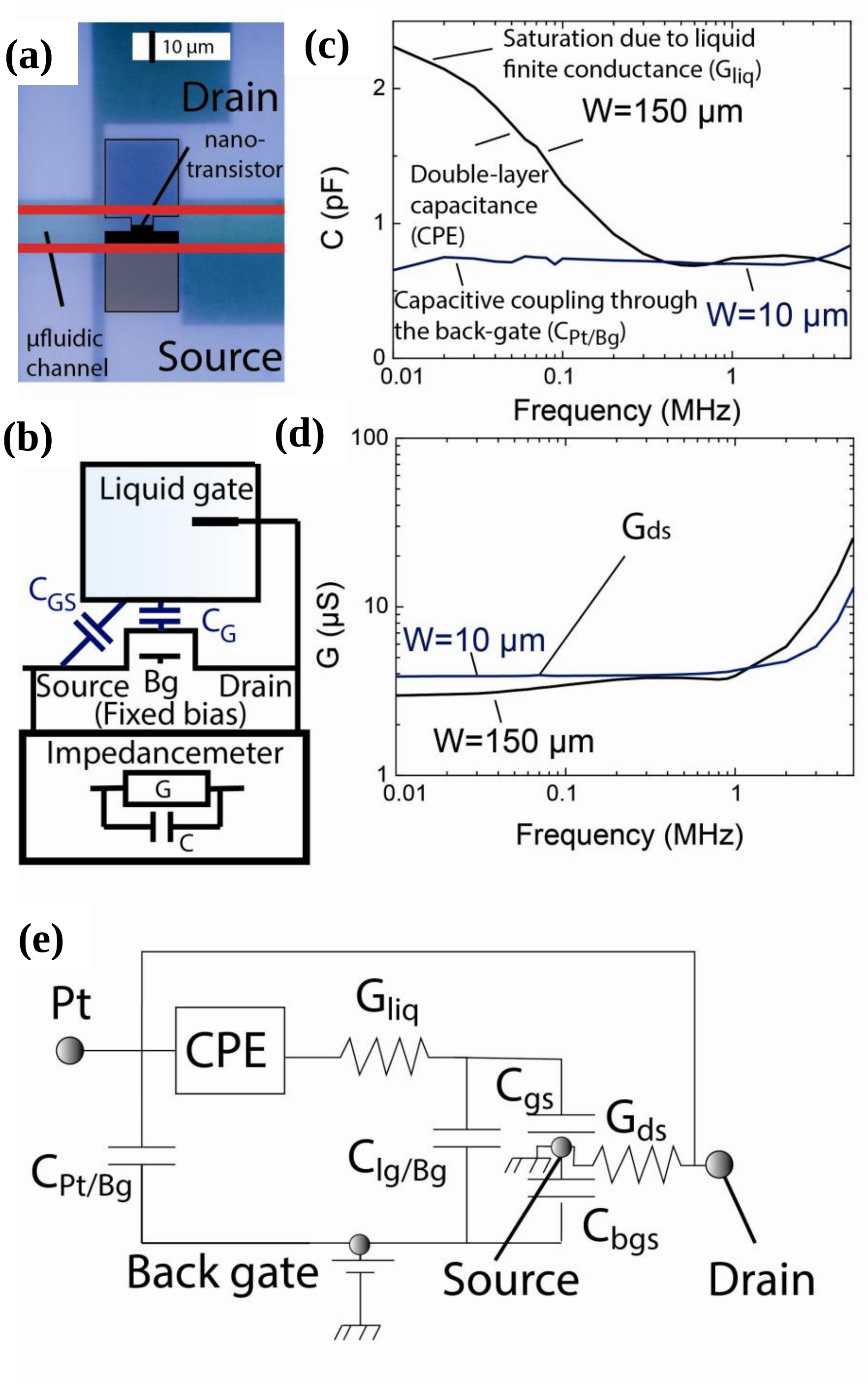

Figure 2.14 (a) Zoomed-out optical microscope image from Figure 2.9a, showing the microfluidic channel limit in red (10-µm-wide microfluidic channel) and the nanotransistor below. Black area indicates coupling between the source and liquid gate. Gray area indicates coupling when the microfluidic channel width exceeds 10 µm. **(b)** Schematic view of the experimental setup for measuring the frequency response of the nanotransistor biosensor. Liquid gate and drain are connected together and biased with DC (+0.1 V) plus AC (0.05 V) signals.

The measured impedance is transposed to that of an equivalent G-C parallel circuit, with G and C the measured conductance and capacitance, respectively. **(c & d)** Measured C and G as a function of frequency for nanotransistor biosensors with microfluidic channel widths of 10 and 150 µm. **(e)** Schematic equivalent circuit derived from the step-by-step approach done in Figure 2.15 CPE, constant phase element representing the double-layer capacitance at the Pt electrode (see Figure 2.15a for its measurement between two Pt electrodes); G_{liq}, conductance of the microfluidic channel; $C_{Pt/Bg}$, capacitance between the Pt and back gate (independent of the presence of liquid); and $C_{lg/Bg}$, capacitance between the microfluidic channel and the back gate. Component values corresponding to asymptotic fits in (d) and (e) are as follows: $G_{liq\_W=150\mu m}$ ~ 60 nS, $G_{liq\_W=10\mu m} < 6$ nS, $C_{Pt/Bg} = 0.8$ pF, $G_{ds} = 4$ µS.

between the microfluidic channel and the transistor. In the impedance measurement, the drain and liquid gate are connected to the back-gate voltage, which has a fixed bias (Figure 2.14b). Due to the tiny dimensions of the transistor, we expect the liquid-gate capacitance C_G (aF range [13]) to be much smaller than the liquid gate/source capacitance C_{GS}.

Figure 2.14c and 2.14d show the capacitance C and conductance G, measured with an impedancemeter, as a function of frequency for two microfluidic channel widths. For the 150-µm-wide channel, the capacitance response was bumpy and conductance was nonconstant. With the 10 µm-wide channel, an ideal flat response was observed up to few mega-Hertz. Figure 2.14e shows a proposed equivalent circuit to fit the measured impedance.

The double-layer capacitance at the Pt/liquid interface is at the origin of the large slope observed in Figure 2.14c, as a similar slope was observed for the capacitance measured between two Pt electrodes (Figure 2.15a). The equivalent circuit is the so-called constant phase element (CPE) [48], which corresponds to an imperfect capacitor whose admittance is $(j\ A\ \omega)^m$ with independent frequency constants A and m ($0 < m < 1$). The finite liquid conductance G_{liq} tends to reduce the capacitance slope at low frequency (Figure 2.14c) and shift the position of the capacitance bump to lower frequency. G_{liq} is related to the ionic strength (Figure 2.15c) or the smaller microfluidic channel section (Figure 2.15e). The bump is not observed for W = 10 µm (Figure 2.14c) because the bump is shifted toward too low of frequencies. The remaining “stray” capacitance measured at 1 MHz (~0.8 pF) refers to capacitive coupling between the Pt gate and the source via the not-heavily-doped back gate [49] (see Figure 2.15c and 2.15e for direct measurements of the capacitive coupling between the Pt electrode and the back gate). Similar stray capacitances have been extracted for contact leads with a device coupled to an inductance capacitance resonator [50]. These results point to the importance of

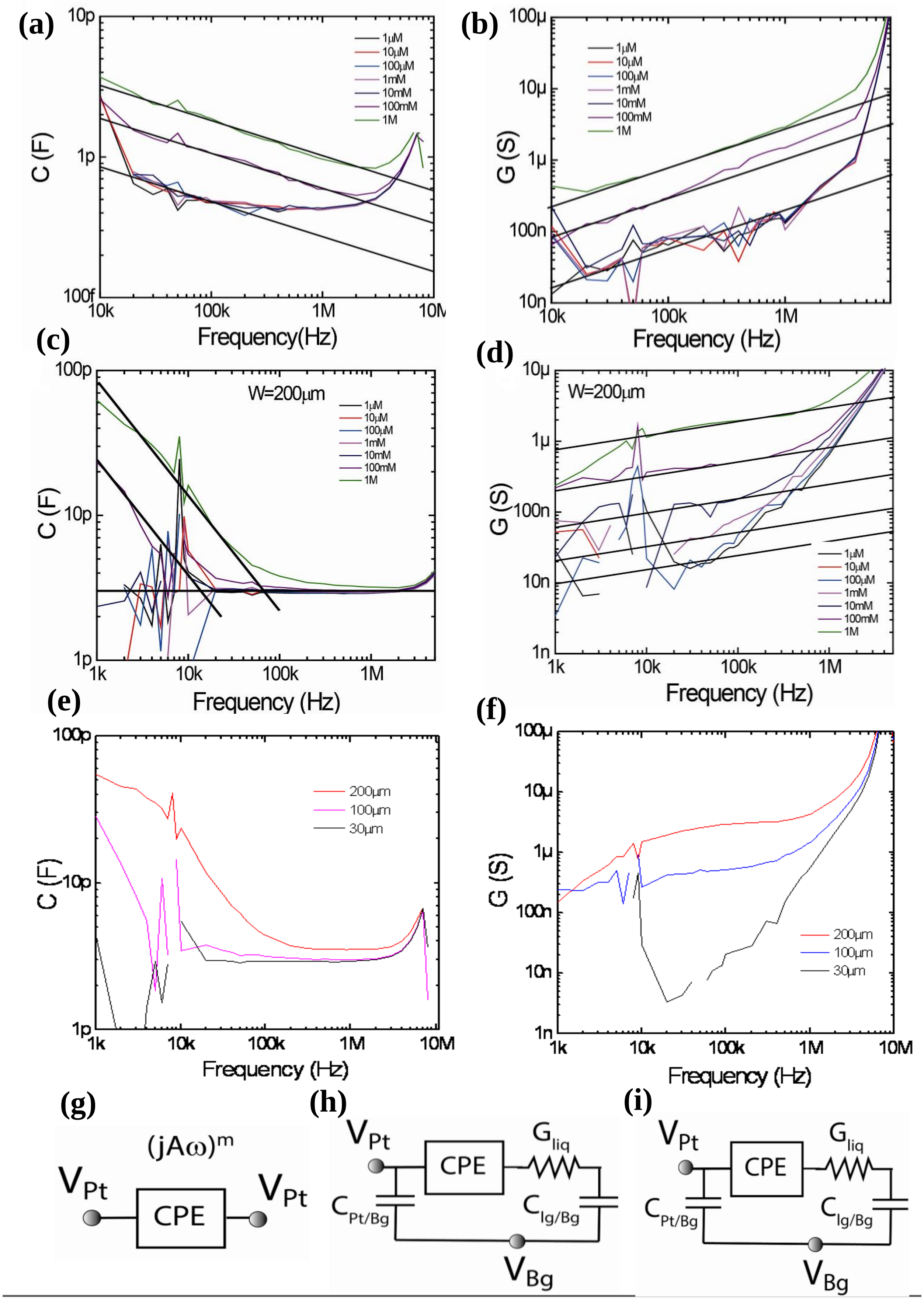
(a)
10p
1p
100f
C (F)
10k
100k
1M
10M
Frequency(Hz)
1µM
10µM
100µM
1mM
10mM
100mM
1M
(b)
100µ
10µ
1µ
100n
10n
G (S)
Frequency (Hz)
(c)
100p
10p
1p
C (F)
W=200µm
1k
10k
100k
1M
Frequency (Hz)
(d)
10µ
1µ
100n
10n
1n
G (S)
W=200µm
(e)
100p
10p
1p
C (F)
200µm
100µm
30µm
1k
10k
100k
1M
10M
Frequency (Hz)
(f)
100µ
10µ
1µ
100n
10n
1n
G (S)
200µm
100µm
30µm
Frequency (Hz)
(g)
(jAω)^m
V_Pt
CPE
V_Pt
(h)
V_Pt
CPE
G_liq
C_Pt/Bg
C_lg/Bg
V_Bg
(i)
V_Pt
CPE
G_liq
C_Pt/Bg
C_lg/Bg
V_Bg

Figure 2.15 Measured capacitance C and conductance G with the impedancemeter (G, C parallel equivalent circuit) **(a & b)** between two Pt electrodes inside the microfluidic channel. Results are nicely fitted with a constant phase element (CPE) with m=0.75, $A=3\times10^{-11}$ [at 1M], $A=2\times10^{-11}$ [at 0.1M], $A=8\times10^{-12}$ [at < 0.1M] shown in **(g)**. **(c & d)** between a Pt electrode inside the 200 µm microfluidic channel and the back-gate. Results are nicely fitted with a constant phase element (CPE), with m=0.2, $A=2\times10^{-7}$ [at 1M], $A=5.5\times10^{-8}$ [at 0.1M], $A=1.5\times10^{-8}$ [at 10^{-2}M], $A=4.5\times10^{-9}$ [at 10^{-3}M], $A=2\times10^{-9}$ [at 1µM] shown in **(h)**. **(e & f)** between a Pt electrode inside the microfluidic channel and the back-gate for 3 different microfluidic channel widths.

ultimate integration that is, the smallest distance between the electrical contacts and the microfluidic channel as well as the reduction in microfluidic channel width. The increase of conductance G at high frequency could come from the contribution of the dielectric loss (imaginary part of the capacitance times the frequency). Previously, the frequency bandwidth of such nanotransistor biosensors had been limited to tens of kilo-Hertz [12, 40]. With ultimate integration of the PDMS-based LoC with 10-µm microfluidic channels, a clean frequency response can be achieved up to few mega-Hertz. Including a resonance circuit with a radiofrequency-compatible connection could extend this response to the giga-Hertz range [50].

2.5.4 Impact of microfluidic channel width on the nanotransistors electrical properties

Microfluidic channel scaling had an unexpected impact on the electrical properties of the nanotransistor. As the microfluidic channel width decreased, the V_T of the nanotransistor biosensor increased (Figure 2.16a and 2.16b) with 1/W dependence. This effect led to a remarkable shift of 0.7 V between the 200- and 10-µm-wide channels, which did not depend on the ionic strength (Figure 2.17a). In typical metal-oxide semiconductor transistors, V_T can be tuned via the work function of the metal gate, to optimize the biasing conditions for low power consumption. This tuning is not possible with nanotransistor biosensors that have liquid gates (Pt or Ag/AgCl electrodes). Using the back-gate voltage V_{bg} to shift the V_T can be useful, but affects all devices. Thus, the ability to tune V_T by the microfluidic channel width could offer a very useful advantage.

We propose an underlying mechanism for our observation. As PDMS was exposed to plasma O_2 before bonding to the substrate, some of the OH interfacial sites become negatively charged when hydrated. These fixed surface charges induce a zeta (ξ) potential at the PDMS/liquid interface (see Figure 2.16c), which is usually negative at pH values greater than 2 [51]. The 1/W dependence of V_T could be explained by a simple capacitive coupling situation, analogous to that of flash memories (see Figure 2.17b). However, this

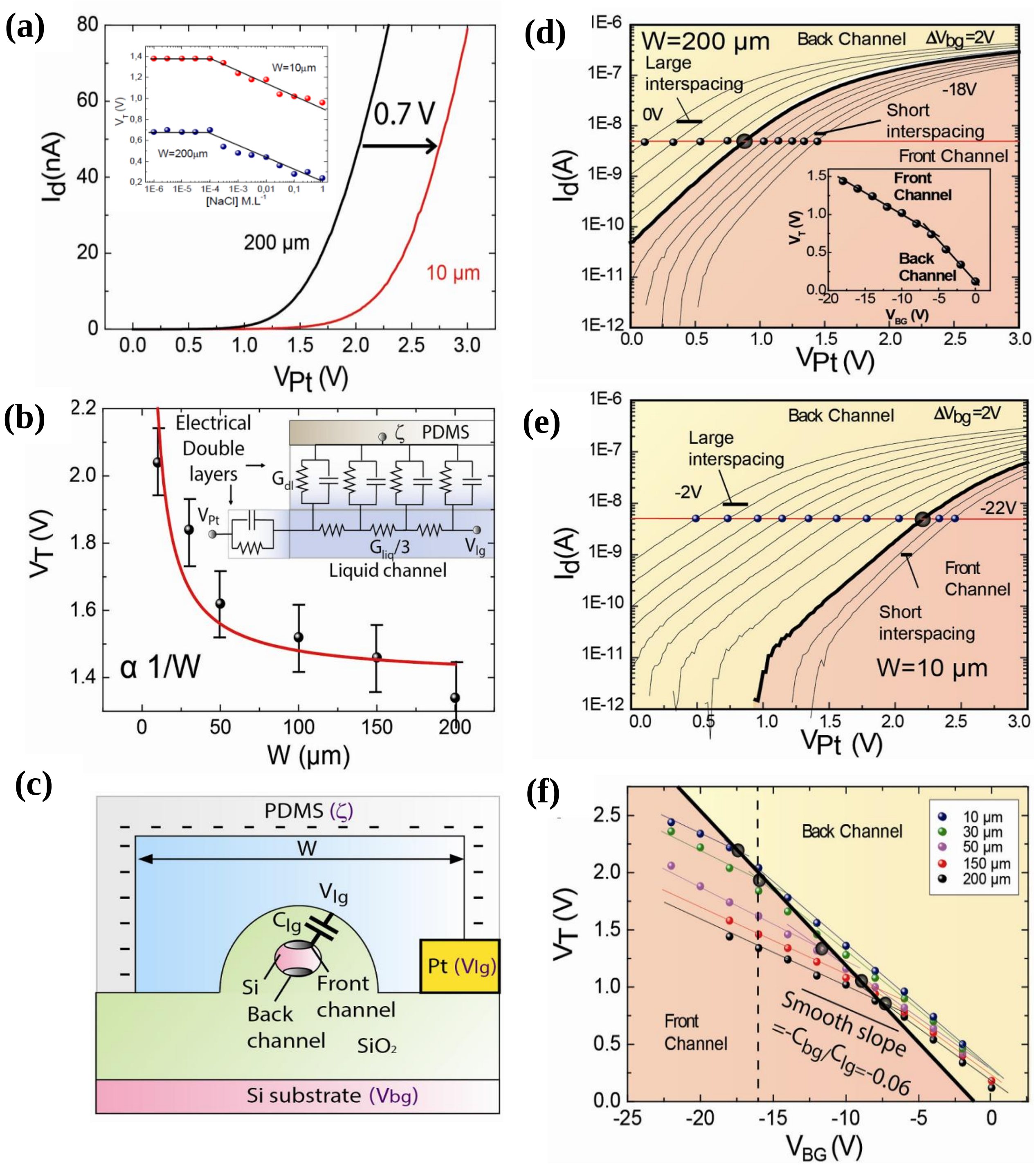

Figure 2.16 **(a)** Drain current-liquid gate nanotransistor characteristics for microfluidic channel widths of W = 10 µm and W = 200 µm. In both cases, V_{bg} = -16 V, to be in the usual front-channel operation mode. Inset: Variation of 0D ISFETs threshold voltage as function of [NaCl] for two different microfluidic channel widths W = 200 µm and 10 µm. **(b)** Threshold voltage V_T (measured at I_d = 5 nA) plotted as a function of microfluidic channel width W. The error bar, which is larger than the error related to ionic strength, corresponds to the typical dispersion in V_T between 0D ISFETs when a large microfluidic channel width is used. Inset: Schematic equivalent circuit. ζ, zeta potential at the PDMS interface; and $G_{liq/3}$, third of the conductance of

a fraction of the microfluidic channel length. **(c)** Schematic cross-sectional view of the PDMS device, with negative charges at the interface (ξ potential) and the nanoscale transistor with electrons that can be in the front or back channel. **(d)** I_d–V_{lg} for different V_{bg} values from 0 to -18 V, by steps of ΔV_{bg} = 2V. Beige color indicates the back-channel operation mode (large interspacing between I_d–V_{lg} curves). Peach color corresponds to front-channel operation. W = 200 µm. **(e)** Similar curve as (d), but with W = 10 µm. **(f)** V_T–V_{bg} curve for all microfluidic channel widths obtained from the V_T at each V_{bg}, as indicated in (d) and (e). Dashed line indicates the biasing conditions for (a) (front-channel mode).

explanation considers the liquid as a simple capacitor, in which the capacitance between the ξ potential and the transistor scales as 1/W. This explanation is not consistent with the usual double-layer capacitance, which does not depend on W and strongly depends on ionic strength (not observed in Figure 2.17a). For these reasons, we propose an equivalent circuit (inset in Figure 2.16b) to describe the voltage loss along the entire microfluidic channel. In this circuit, the CPE is replaced by a capacitance in parallel with a resistance for simplicity [52]. The microfluidic channel conductance G_{liq} (Figure 2.16e) should be spread into finite elements to account for coupling to the ξ potential along the channel. When G_{liq} was spread into three elements, a nice fit with Pspice simulation (Orcad) was obtained (see Figure 2.17c). A semiempirical equation can also be derived:

$$V_T = V_{T0} + \frac{A\xi}{G_{liq}} = V_{T0} + \frac{B\xi}{W} \qquad \text{Eq (2.3)}$$

where V_{T0} is the threshold voltage for a large microfluidic channel, and A is a constant. As G_{liq} = A.W and is proportional to a section of the microfluidic channel, Eq 2.3 shows that ΔV_T scales as 1/W (because ξ should be independent of W). Equation 2.3 should not depend on the experimentally measured ionic strength (see Figure 2.17b). However, V_{T0} is related to the Nernst potential because all resistors in the equivalent circuit will be affected in the same way. The effect of integration may be considered as opposite to expectations of a reduced V_T for low power consumption, but p-type nanotransistor biosensors could benefit from this finding.

A closer look at the electrical characteristics reveals another difference between large (Figure 2.16d) and small (Figure 2.16e) microfluidic channels. When the channel width was decreased to 10 µm (Figure 2.16e), the electrons were always in the back channel (schematic view in Figure 2.16c) unless a large negative back-gate voltage was applied. This conclusion was obtained by considering the I_d -V_{Pt} curves for different values of V_{bg}. When electrons are in the back channel (low –V_{bg}), a given variation of V_{bg} leads to a large shift of V_T (large interspacing) compared to when electrons are in the front channel (strong –V_{bg}) [13, 53]. The transition from the front to the back channel is obtained from the change of slope in the V_T–V_{bg} curve (Figure 2.16d, inset). The smooth slope (front-channel mode) provides a quantitative value of the C_{bg}/C_{lg} ratio ~ 0.06, close to our previously reported value with microbaths [13] and to the value estimated for a classical Si nanowire biosensor [54]. Figure 2.16f generalizes this observation through a plot of V_T–V_{bg} for all microfluidic channel widths. There was a progressive shift in the front- to back-channel transition to a more negative V_{bg} when the microfluidic channel width was decreased. The ratio C_{bg}/C_{lg} barely depends on the microfluidic channel width.

It was recently suggested that the signal-to-noise ratios of biosensors can be increased by 50% by removing electrons from the front channel and applying bias on the back gate [55]. This finding was attributed to coupling between the liquid and back gate. Using small microfluidic channels, such enhanced sensitivity can be effective without applying any V_{bg} because the electrons are located at the back channel.

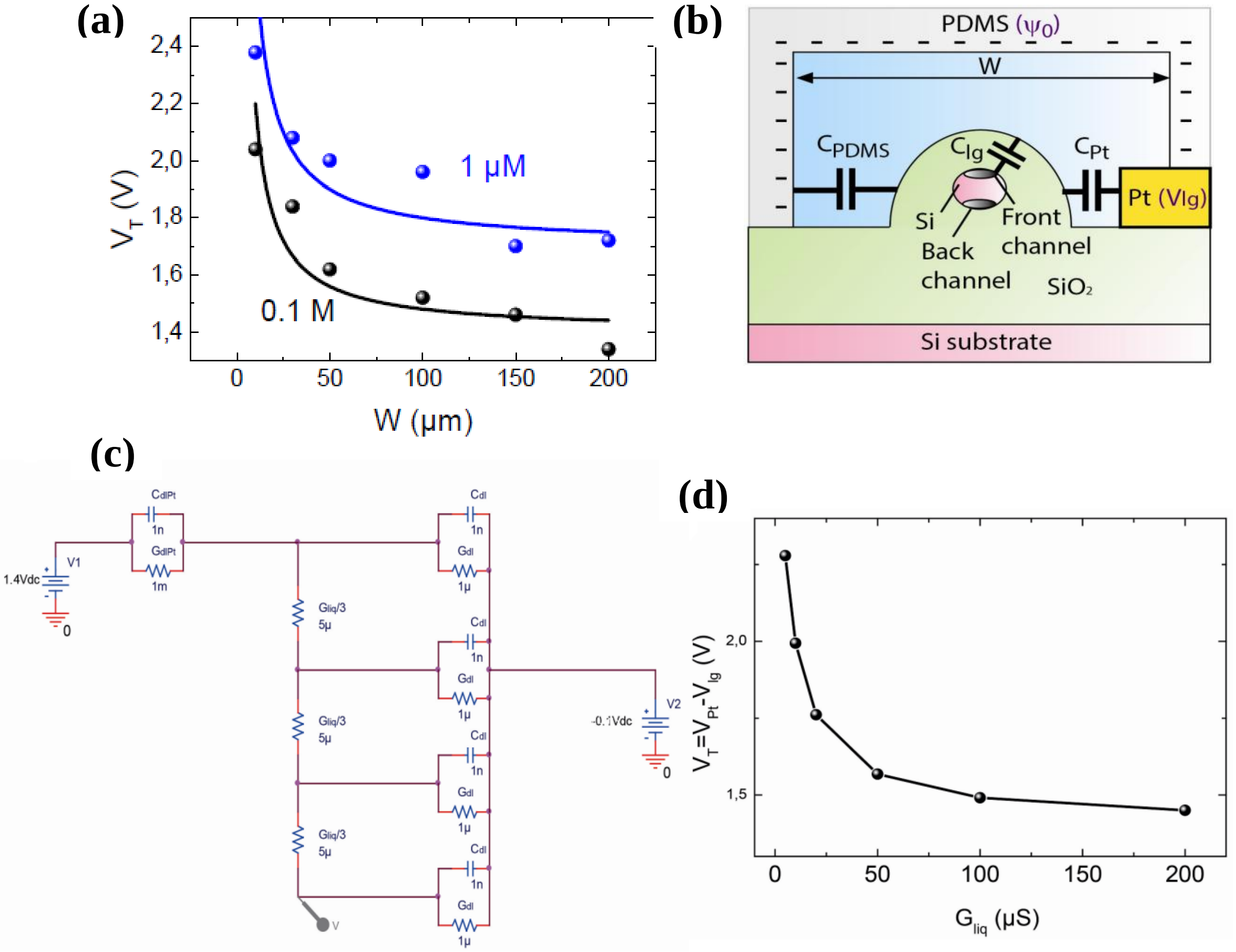

Figure 2.17 (a) Figure 2.16b is plotted with an additional ionic strength (1 µM) to highlight the small impact of ionic strength on the observed effect. **(b)** Schematic cross section view of the device composed of PDMS with negative charges at interface (potential Ψ_0), the nanoscale

transistor with electrons that can be either in front- or back-channel and capacitive coupling C_{PDMS}, C_{Pt} to the device **(c)** Schematic equivalent circuit proposed in Figure 2.16b inset. By playing with the value of G_{liq} using Orcad Pspice simulator, we see that V_{Pt}-V_{lg} α $1/G_{liq}$, that led us to the semi-empirical law (Eq 2.3) that fits nicely experimental results (Figure 2.16b).

2.6 Summary

Maximum integration of PDMS-based LoCs with nanosensors can reduce costs and analyte volumes while allowing high-frequency operation. In this study, the limit of integration was set by the critical distance between the microfluidic channel and the holes for the electrical contacts. We demonstrated one of the smallest LoC with nanotransistor biosensors to date, with a gain in chip width of about one order of magnitude compared to previous reports, which was close to our predicted physical limit.

To highlight the possibility of using such LoCs for functional devices, we used 0D ISFET sensors. We successfully reproduced the controversial Nernstian response to NaCl with uncoated 0D ISFETs [3, 4, 12 and 34] and reduced the standard deviation in the results compared to the microbath approach. Volumes as low as a few hundred picoliters could be measured with unchanged NaCl response. We demonstrated the importance of scaling the electrical contacts and microfluidic channel width for optimal frequency response of these sensors up to a few mega-Hertz. We observed the back-channel operation of our devices with microfluidic channels, even without back-gate bias, which was recently suggested as the optimal configuration for such biosensors. Finally, we uncovered the possibility of tuning the V_T of nanotransistor biosensors with the microfluidic channel width. This possibility would allow power consumption by these sensors to be optimized.

Overall, the results of this study offer the promise of parallel sensor fabrication at the wafer scale with optimized integration and fabrication costs. The impact of this study is not limited to nanotransistor biosensors, but could also be of interest for all LoCs that require electrical contacts close to a microfluidic channel.

Bibliography

[1] Patolsky F, Zheng G, Lieber CM (2006) Fabrication of silicon nanowire devices for ultrasensitive, label-free real-time detection of biological and chemical species. Nature Protoc 1(4):1711-1724.

[2] Stern E, Klemic JF, Routenberg DA, Wyrembak PN, Turner-Evans DB, Hamilton AD, Lavan DA, Fahmy TM, Reed MA (2007) Label-free immunodetection with CMOS-compatible semiconducting nanowires. Nature 445:519-522.

[3] Clément N, Nishiguchi K, Dufrêche JF, Guérin D, Fujiwara A, Vuillaume D (2013) Water Electrolysis and Energy Harvesting with Zero-Dimensional Ion-Sensitive Field-Effect Transistors. Nanolett 13 (8):3903–3908.

[4] Tarasov A, Wipf M, Stoop RL, Bedner K, Fu W, Guzenko A, Knopfmacher O, Calame M, Schönenberger C (2012) Understanding the Electrolyte Background for Biochemical Sensing with Ion-Sensitive Field-Effect Transistors. ACS Nano 6 (10):9291–9298.

[5] Mannik J, Heller I, Janssens AM, Lemay SG, Dekker C (2008) Charge Noise in Liquid-Gated Single-Wall Carbon Nanotube Transistors. Nano Lett 8 (2):685–688.

[6] Ohno Y, Maehashi K, Yamashiro Y, Matsumoto K (2009) Electrolyte-Gated Graphene Field-Effect Transistors for Detecting pH and Protein Adsorption. Nano Lett 9 (9):3318–3322.

[7] Heller I, Chatoor S, Männik J, Zevenbergen M, Oosting JB, Morpurgo AF, Dekker C, Lemay SG (2010) Charge Noise in Graphene Transistors. Nano Lett 10 (5):1563–1567.

[8] Arlett JL, Paul MR, Solomon JE, Cross MC, Fraser SE, Roukes ML (2007) BioNEMs: Nanomechanical Systems for Single-Molecule Biophysics. Lect. Notes Phys. 711:241-270.

[9] Arlett JL, Myers EB, Roukes ML (2011) Comparative advantages of mechanical biosensors. Nature Nanotechnology 6:203-215.

[10] Waggener PS, Tan CP, Craighead HG (2010) Microfluidic integration of nanomechanical resonators for protein analysis in serum. Sensors and Actuators B 150 (2):550-555.

[11] Barton RA, Ilic B, Verbridge SS, Cipriani BR, Parpia JM, Craighead HG (2010) Fabrication of a Nanomechanical Mass Sensor Containing a Nanofluidic Channel. Nano Lett 10 (6):2058–2063.

[12] Clément N, Nishiguchi K, Dufrêche JF, Guérin D, Fujiwara A, Vuillaume D (2011) A silicon nanowire ion-sensitive field-effect transistor with elementary charge sensitivity. Applied Physics Letters 98 (1): 014104.

[13] Clément N, Nishiguchi K, Fujiwara A, Vuillaume D (2011) Evaluation of a Gate Capacitance in the Sub-aF Range for a Chemical Field-Effect Transistor With a Si Nanowire Channel. IEEE Transactions on Nanotechnology 10 (5):1172-1179.

[14] Rigante S, Livi P, Rusu A, Chen Y, Bazigos A, Hieremann A, Ionescu AM (2013) FinFET integrated low-power circuits for enhanced sensing applications. Sensors and Actuators B 186:789-795.

[15] Buitrago E, Badia MFB, Georgiev YM, Yu R, Lotty O, Holmes JD, Nightingale AM, Guerin HM, Ionescu AM (2014) Electrical characterization of high performance, liquid gated vertically stacked SiNW-based 3D FET biosensors. Sensors and Actuators B 199:291-300.

[16] Mu L, Droujinine IA, Rajan NK, Sawtelle SD, Reed MA (2014) Direct, Rapid, and Label-Free Detection of Enzyme–Substrate Interactions in Physiological Buffers Using CMOS-Compatible Nanoribbon Sensors. Nano Lett 14 (9):5315–5322.

[17] Zhao J, Hasmi A, Xue W (2012) A compact lab-on-a-chip nanosensor for glycerol detection. Applied Physics Letters 100 (24):243109.

[18] Nikolic-Jaric M, Romanuik SF, Ferrier GA, Bridges GE, Butler M, Sunley K, Thomson DJ, Freeman MR (2009) Microwave frequency sensor for detection of biological cells in microfluidic channels. Biomicrofluidics 3(3):034103.

[19] Grenier K, et al. (2009) Integrated broadband microwave and microfluidic sensor dedicated to bioengineering. IEEE Trans MTT 57(12):3246-3253.

[20] Takahashi Y, et al. (1995) Fabrication technique for Si single-electron transistor operating at room temperature. Electron Lett 31(2):136−137.

[21] Nishiguchi K, Inokawa H, Ono Y, Fujiwara A, Takahashi Y (2004) Multilevel memory using an electrically formed single-electron box. Applied Physics Letters 85(7):1277-1279.

[22] Clément N, Nishiguchi K, Fujiwara A, Vuillaume D (2012) One-by-one trap activation in silicon nanowire transistors. Nature Communications 1:92.

[23] Balakrisnan B, Patil S, Smela E (2009) Patterning PDMS using a combination of wet and dry etching. J Micromech Microeng 19: 047002.

[24] Kang JH, Um E, Park JK (2009) Fabrication of poly(dimethylsiloxane) membrane with well-defined through-holes for three-dimensional microfluidic networks. J Micromech Microeng 19(4):045027.

[25] Hosokawa, K., Hanada, K., Maeda, R., J. Micromech. Microeng. 2002, 12, 1.

[26] Holden, M. A., Kumar, S., Beskok, A., Cremer, P. S., J. Micromech. Microeng. 2003, 13, 412–418.

[27] Gervais, T., El-Ali, J., Gunther, A., Jensen, K. F., Lab. Chip. 2006, 6, 500–507.

[28] Hardy BS, Uechi K, Zhen J, Pirouz Kavehpour H (2009) The deformation of flexible PDMS microchannels under a pressure driven flow. Lab Chip 9(7): 935-938.

[29] Sollier E, Murray C, Maoddi P, Di Carlo D, Lab. Chip. 2011, 11, 3752–3765.

[30] Wu GW, Shih WP, Hui CY, Chen SL, Lee CY (2010) Bonding strength of pressurized microchannels fabricated by polydimethylsiloxane and silicon,” Journal of Micromechanics and Microengineering 20:115032.

[31] Lötters JC, Olthuis W, Veltink PH, Bergveld P (1997) The mechanical properties of the rubber elastic polymer polydimethylsiloxane for sensor applications. J Micromech Microeng 7:145-147.

[32] Thorsen T, Maerkl SJ, Quate SR (2002) Microfluidic large-scale integration. Science 298 (5593):580-584.

[33] Stern E, Wagner R, Sigworth FJ, Breakers R, Fahmy TM, Reed MA (2007) Importance of the Debye Screening Length on Nanowire Field Effect Transistor Sensors. Nano Lett 7(11):3405-3409.

[34] Upadhyay S, Frederiksen R, Lloret N, DeVico L, Krogstrup P, Jensen JH, Martinez KL, Nygard J (2014) Indium arsenide nanowire field-effect transistors for pH and biological sensing. Applied Physics Letters 104:203504.

[35] M. Kruger, M. R. Buitelaar, T. Nussbaumer, C. Schçnenberger, Appl. Phys. Lett. 2001, 78, 1291 –1293.

[36] W. Fu, C. Nef, O. Knopfmacher, A. Tarasov, M. Weiss, M. Calame, C. Schçnenberger, Nano Lett. 2011, 11, 3597 – 3600.

[37] M. G. Nikolaides, S. Rauschenbach, S. Luber, K. Bucholz, M. Tornow, G. Abstreiter, A. R. Bausch, Chem Phys Chem 2003, 4, 1104 –1106.

[38] I. Park, Z. Li, A. P. Pisano, R. S. Williams, Nanotechnology 2009, 21, 015501 –015 509.

[39] Wipf et al. (2013) Selective sodium sensing with gold-coated silicon nanowire field-effect transistors in a differential setup. ACS Nano 7(7): 5978-5983.

[40] Clément N, Han XL, Larrieu G (2013) Electronic transport mechanisms in scaled gate-all-around silicon nanowire transistor arrays. Applied Physics Letters 103:263504.

[41] Liu Y, Banerjee A, Papautsky I (2014) Precise droplet volume measurement and electrode-based volume metering in digital microfluidics. Microfluidics Nanofluidics 17(2):295-303.

[42] Srinivasan V, Pamula VK, Fair RB (2004) An integrated digital microfluidic lab-on-a-chip for clinical diagnostics on human physiological fluids. Lab Chip 4: 310-314.

[43] Lapierre F, Pirret G, Drobecq H, Melnyk O, Coffinier Y, Thomy V, Boukherroub R (2011) High sensitive matrix-free mass spectrometry analysis of peptides using silicon nanowires-based digital microfluidic device. Lab Chip 11(9):1620-1628.

[44] Li J, Vitusevich SA, Petrychuk MV, Pud S, Offenhäusser A, Danilchenko BAJ, Appl. Phys. 2013, 114 (20), 203704.

[45] Rajan NK, Routenberg DA, Chen J, Reed M A, IEEE Electron Device Lett. 2010, 31 (6), 615−617.

[46] Zheng G, Gao XPA, Lieber CM (2010) Frequency domain detection of biomolecules using silicon nanowire biosensors. Nano Lett 10(8):3179-3183.

[47] Li J, Pud S, Petrychuk M, Offenhausser A, Vitusevitch S (2014) Sensitivity Enhancement of Si Nanowire Field Effect Transistor Biosensors Using Single Trap Phenomena. Nano Lett 14 (6):3504-3509.

[48] Zoltowski P (1998) On the electrical capacitance of interfaces exhibiting constant phase element behaviour. J Electroanal Chem 443 (1):149-154.

[49] Cristoloveanu S, Hemmert PLF, Izumi K, Celler K, Assaderaghi F, Kim YW (2001) Silicon-on-Insulator Technology and devices' The electrochemical society ISBN 1-56677-309-1.

[50] Nishiguchi K, Yamaguchi H, Fujiwara A, Van der Zant HSJ, Steele GA (2013) Wide-bandwidth charge sensitivity with a radio-frequency field-effect transistor. Applied Physics Letters 103:143102.

[51] Kirby BJ, Hasselbrink EF (2004) Zeta potential of microfluidic substrates: 1. Theory, experimental techniques, and effects on separations. Electrophoresis 25: 187-202.

[52] Jovic VD, Jovic BM (2003) EIS and differential capacitance measurements onto single crystal faces in different solutions Part I: Ag (111) in 0.01 M NaCl. J Electroanal Chem 541:1-11.

[53] Fujiwara A, Horiguchi S, Nagase M, Takahashi Y (2003) Threshold Voltage of Si Single-Electron Transistor. Jpn J Appl Phys 42 (1):2429-2433.

[54] Paska Y, Stelzner T, Assad O, Tisch U, Christiansen S, Haick H (2012) Molecular Gating of Silicon Nanowire Field-Effect Transistors with Nonpolar Analytes. ACS Nano 6 (1), 335-345.

[55] Pud S, Li J, Sibiliev V, Petrychuck M, Kovalenko V, Offenhäusser A, Vitusevitch S (2014) Liquid and Back Gate Coupling Effect: Toward Biosensing with Lowest Detection Limit. Nano Lett 14 (2):578-584.

3

U-shape pH response with Zero-Dimensional Nanotransistor Biosensors

The pH measurement is one of the most commonly tested parameter in chemical and biochemical processes. Since the first use of glass electrode to study pH [1] (see Figure 3.1a for the schematic view), the technology and methods have extended the scope of pH detection. In the next few upcoming decades, we will likely see the flourishing technologies that allow us to control and better monitor our foods [2], drinking water [3], air we breathe and even drugs that we consume using new screening techniques that strictly rely on biosensors [8].

Surface charging in liquid is a central point to many applications including genome sequencing [4], biomedical diagnosis [5], printed electronic displays [6], giant osmotic power harvesting under salinity gradients [7] or drug delivery [8]. Typically, a surface such as silicon oxide (or glass) is negatively charged at neutral pH due to deprotonated silanol groups (Si-O$^-$). When it is in contact with a solution containing ions, positive ions are attracted to the surface, forming an immobile layer and a diffuse layer (typically in the nm range). The surface potential (Ψ_0), is well described by the site binding model (SBM: see the following section 3.1) that predicts a pH-dependent density of charged sites at liquid / oxide interface arising from protonation or deprotonation of -OH surface functional groups [9, 10]. This model leads to a monotonic decrease of Ψ_0 with increased pH as shown in Figure 3.1b. Since the introduction of the pH concept [11] and its measurement ability with a pH glass electrode, a selective and reliable electrode toward H^+ [1], few basic concepts have generally stood the test of time.

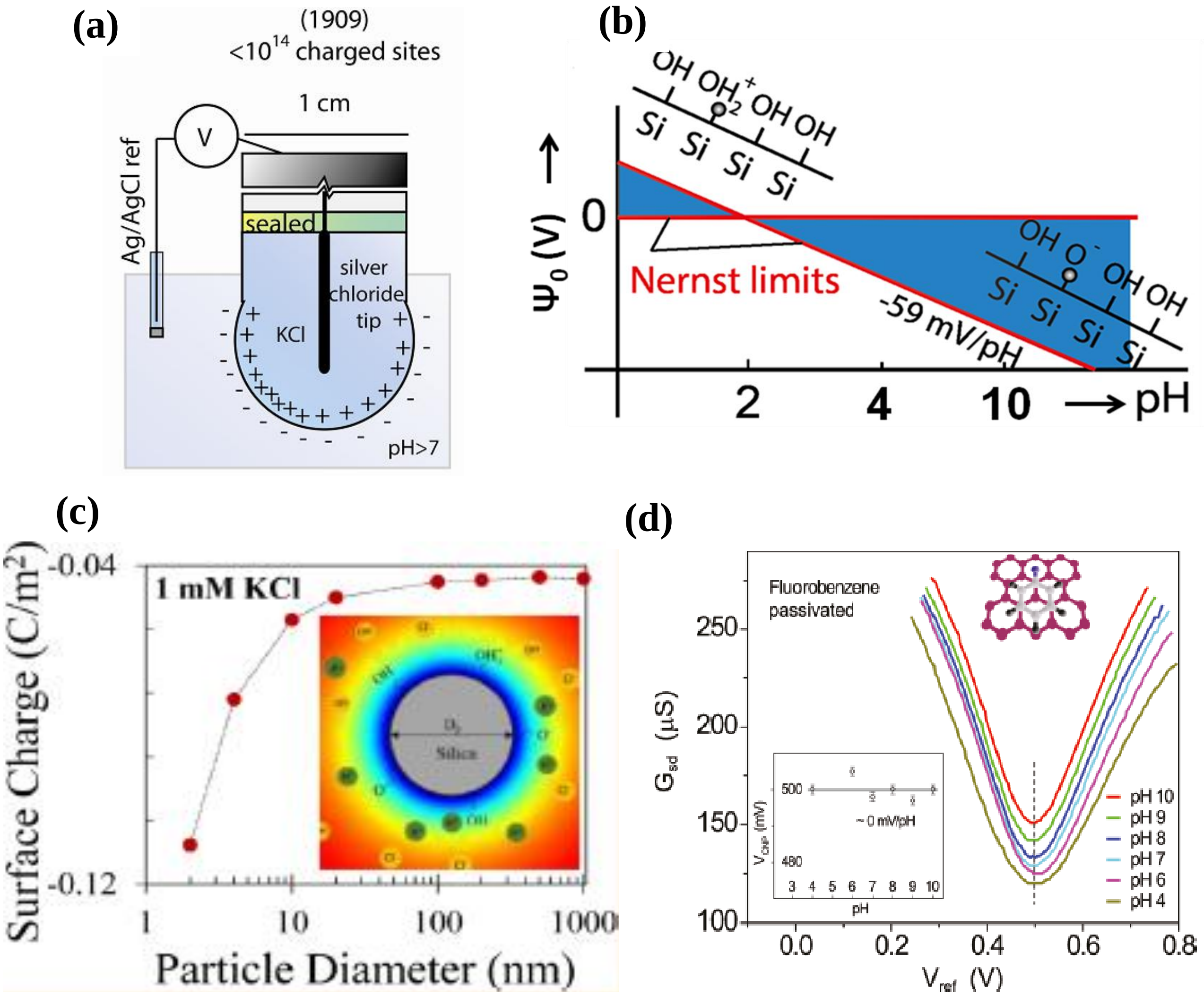

Figure 3.1 (a) Schematic view of pH glass electrode (GE) **(b)** plot showing universal monotonic decrease of surface potential Ψ_0 with pH, The point zero charge pH value is set to PZC =2 as usual for SiO_2 **(c)** Figure reprinted from reference [15]. Plot showing magnitude of surface charge density (σ) increases with decrease in particle diameter for fixed background salt concentration and pH **(d)** Figure adapted from reference [17]. The absence of charge sites in graphene surface showing flat pH response, substantially reduced sensitivity of ~ 0 mV/pH.

First, the universal monotonic decrease of surface potential Ψ_0 with pH has been challenged, but not contradicted. In particular, smaller and smaller ion sensors were studied [12-15], with the interesting observation of surface charge density increase for nanometric silica nanoparticles [15] (see Figure 3.1c). Various materials have been tested. Using a pH inert layer [16] or when the sensor itself is composed with a material without dangling bonds (high-quality graphene [17] or carbon nanotubes [18] for example), the absence of charged sites provides a flat pH response (Ψ_0~0) shown in Figure 3.1d. Other relevant challenges to the usual surface potential picture have emerged from micro- and nano- fluidics fields. It is now accepted that the densities of surface and diffuse charges are not only set by oxides intrinsic properties (dissociation constants K and total density of sites σ), but can be tuned either by a large transverse electric field [19] or by reducing the thickness of liquid channel to few nanometers [20] so as to modify protons concentration. However, so far, when both parameters are fixed, the universal pH response has not been contradicted.

In this Chapter, using a nanoscale transistor (25 nm long and 15 nm wide) with apparently no or only few effective charged surface functional groups, we show rupture in the universal monotonic pH response of oxides. We used PDMS based millimeter square LoC for this study and the fabrication has already described in Chapter 2. Before going into detail study, we will first discuss site-binding model (SBM) [9] proposed for SiO_2 surface in liquid containing charge carriers derived for conventional ISFETs by Bosse, de Rooij, and Bergveld [21] and also discuss the detailed plot of surface potential Ψ_0 as function of pH, estimate the density and the number of sites on 0D ISFETs.

3.1 Liquid/ Oxide interface based on SBM

When a silicon oxide surface is in contact with an electrolyte solution, surface hydroxyl groups (Si-OH) are built up at the oxide / liquid (electrolyte) interface. These hydroxyl groups are charged depending on the pH value of the solution. The pH value, at which the surface is neutral, is called the point of zero charge (pH_{pzc}) (pH_{pzc} = 2 for SiO_2) [9, 10, 21]. At a pH lower than pH_{pzc}, the oxide surface is positively charged and at a pH higher than pH_{pzc} the surface is negatively charged. Consequently, at physiological pH value (pH ~ 7), the net surface charge of silicon oxide is negative.

In this section, the relationships between the surface potential ψ_0 and the pH value of the solution, the total surface charge density σ_0 and the concentration of ions in the electrolyte are considered. Usually, the ISFET operation is explained by so-called site-binding theory, which relates the interface potential to the concentration of the hydrogen ions in the analyzed solution [9, 10]. According to this theory, the ions present in the solution react with surface charged active sites at the dielectric surface creating hydrogen-active site pairs as shown in Figure 3.2a and consequently changing the total value of the active site charge at the insulator surface. This, in turn, influences the transistor channel current through the variation of the V_{th}. Moreover, the active sites might react not only with the hydrogen ions but also with other ions present in the measured solution, the so-called disturbing ions.

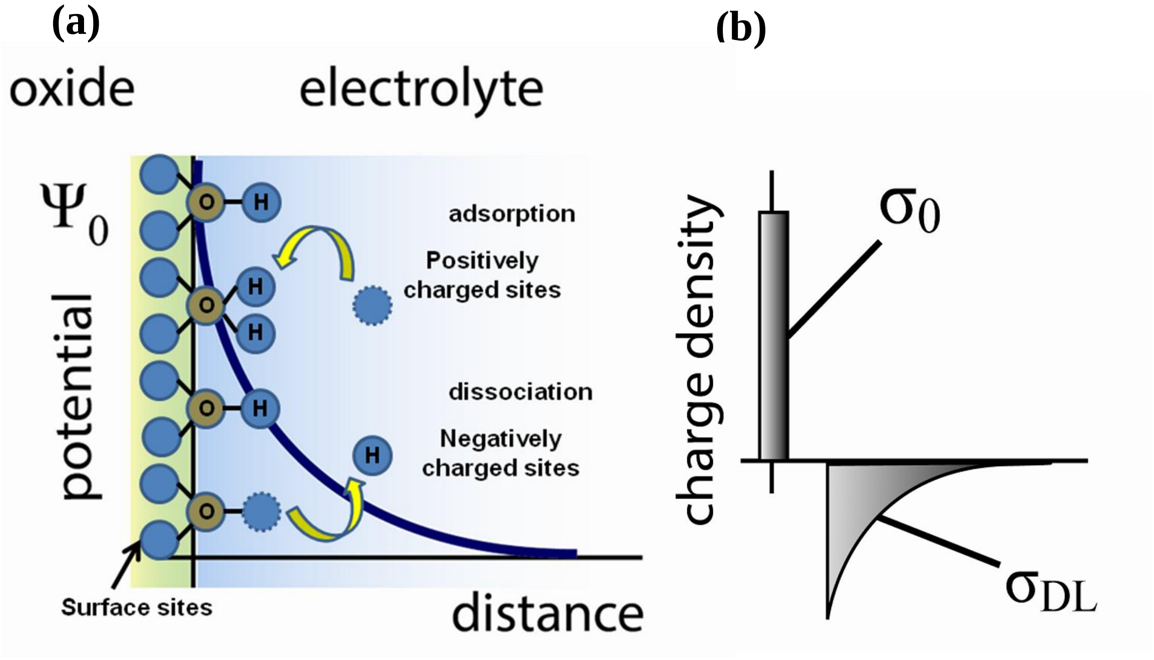

Figure 3.2 **(a)** Schematics illustrate the acid-base equilibrium (chemical reaction) on SiO_2 surface and the potential distribution of double layer formed at a solid material that immersed in an electrolyte solution **(b)** charge distribution at an oxide-electrolyte solution interface.

All these chemical reactions occurring at the phase boundary are reversible and described by the dissociation constant K. Because of the binding of the ions with the active sites, the gradient of ion concentration is created in the electrolyte and, according to the Gouy–Chapman–Stern theory [10]; the so-called double layer is established at the dielectric–electrolyte border as it is shown in Figure 3.2b. The double layer consists of the diffuse layer and the Helmholtz layer. The Helmholtz layer comprises the layer of adsorbed hydrogen ions and the common plane of adsorbed anions and cations [10]. We use the version of the site-binding model (SBM) [9], derived for conventional ISFETs by Bousse, de Rooij, and Bergveld [21]. It provides a relationship between the surface potential Ψ_0 and the pH value of the bulk solution. The amphoteric character of the OH surface groups of SiO_2 can be expressed by two equilibrium constants for the deprotonation (K_a) and the protonation (K_b) reaction:

$$SiOH \leftrightarrow SiO^- + Hs^+, K_a = \frac{\nu_{SiO^-} a_{Hs^+}}{\nu_{SiOH}} \quad \text{Eq (3.1)}$$

$$SiOH_2{}^+ \leftrightarrow SiOH + Hs^+, K_b = \frac{\nu_{SiOH} a_{Hs^+}}{\nu_{SiOH_2{}^+}} \quad \text{Eq (3.2)}$$

With ν being the density of sites of one particular species, $a_{Hs}{}^+$ the activity of the surface protons (see Eq 3.1). The active surface sites are either neutral (SiOH), positively (protonated, $SiOH^{2+}$), or negatively charged (deprotonated, SiO^-). The total density of these sites N_s is

$$N_s = \nu_{SiOH} + \nu_{SiO^-} + \nu_{SiOH_2{}^+} \quad \text{Eq (3.3)}$$

The protonated and deprotonated groups generate the total surface charge density σ_0

$$\sigma_0 = q\left(\nu_{SiOH_2{}^+} - \nu_{SiO^-}\right) \quad \text{Eq (3.4)}$$

Eq 3.5 can be rewritten using Eq 3.2- Eq 3.4 as

$$\sigma_0 = qN_s\left(\frac{a_{Hs}{}^2 - K_aK_b}{a_{Hs}{}^2 + a_{Hs}K_b + K_aK_b}\right) \quad \text{Eq (3.5)}$$

Combining Eq 3.1-3.7, an explicit relationship between the bulk proton activity $a_{Hb}{}^+$ and the surface potential Ψ_0 can be derived [21]

$$a_{Hb^+} = \exp\left(\frac{q\psi_0}{kT}\right)a_{Hs^+} \quad \text{Eq (3.6)}$$

$$a_{Hb^+} = \exp\left(\frac{q\psi_0}{kT}\right)\frac{C_{dl}\psi_0K_b + \sqrt{\left(K_bC_{dl}\psi_0\right)^2 + 4K_aK_b\left(q^2N_s{}^2 - C_{dl}{}^2\psi_0{}^2\right)}}{2\left(qN_s - C_{dl}\psi_0\right)} \quad \text{Eq (3.7)}$$

This equation is used to get Ψ_0-pH (indeed we get pH-Ψ_0 and then replot the graph).Typical literature values for SiO_2 interface are pK_a=6, pK_b=-2, $N_s = 5\times10^{18}$ m^{-2}, pH_{pzc}=2 (pH at point zero charge= (pK_a+pK_b)2).

To get simulations for Figure 3.8b, we use the following equations:

$$\nu_{SiOH} = N_s\left(1 + a_{Hs}{}^+ / K_b + K_a / a_{Hs}{}^+\right) \quad \text{Eq (3.8)}$$

$$\nu_{SiO^-} = K_a\nu_{SiOH} / a_{Hs}{}^+ \quad \text{Eq (3.9)}$$

$$\nu_{SiOH_2{}^+} = \nu_{SiOH}a_{Hs}{}^+ / K_b \quad \text{Eq (3.10)}$$

3.2 U-shape pH response with 0D nanotransistor biosensors

3.2.1 Historical evolution: glass electrode to 0D ISFET pH sensors

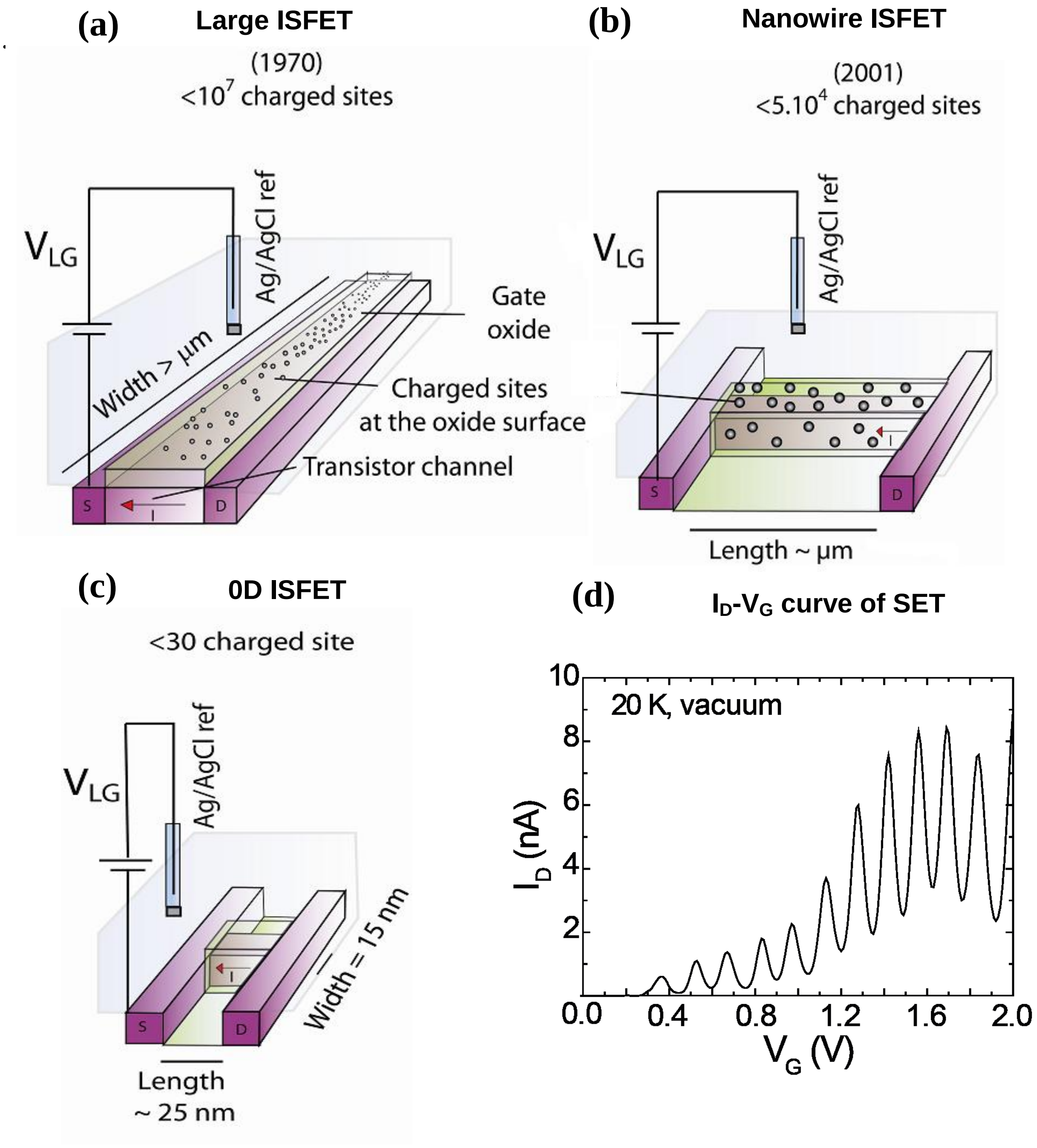

Figure 3.3 (a) Schematic view of ion-sensitive field-effect transistor (ISFET) **(b)** the nanowire ISFET and **(c)** the 0D ISFET proposed in this study **(d)** Drain-current (I_D) versus gate voltage (V_G) curve showing typical oscillations of a single-electron transistor (SET) or quantum dot at “elevated” temperature when liquid gate is replaced by a polysilicon gate.

The tiny transistors used to explore the pH response of nanometric probes are silicon nanotransistor biosensors in the family of ion-sensitive field-effect transistors (ISFETs). These devices initially emerged with dimensions below millimeter square, combining the properties of a transistor with a glass electrode-like interface (schematics of pH glass electrode and large ISFET shown in Figure 3.1a and 3.3a), with the aim to provide highly integrated and cheap chemical biosensors [22]. At the beginning of the 2000s, these ISFETs were drastically scaled with width below 100 nm, the so-called nanowires (NWs, schematics shown in Figure 3.3b) used for highly sensitive biosensing [12, 13]. NWs active length has recently been scaled down to 200 nm [14], but still a monotonic pH response was observed. Devices used in this study are extremely scaled with 15 nm diameter and 25 nm length (schematics shown in Figure 3.4d). We call our device as 0D ISFET or 0D biosensor, not only because of its nanometric dimensions, but also because it operates as a single-electron transistor (SET) or quantum dot at high temperature when the liquid-gate is replaced by a polysilicon gate [23]. Figure 3.4 shows drain-current (I_D) vs gate voltage (V_G) curve showing typical oscillations of a single-electron transistor (SET) or quantum dot at “elevated” temperature, which led to the appellation 0D ISFET or 0D biosensor.

3.2.2. Ψ_0 - pH response of large nanoribbon ISFET

We have integrated together with the 0D ISFET, on the same wafer, a reference device (large ISFET). Both transistors were fabricated with identical technological processes, including the thermal 1000 °C silicon oxidation step (already discussed in Chapter2, and for more information see appendix). The large ISFET is a 10 µm - wide, 7 µm - long, 40 nm-thick silicon nanoribbon transistor. The scanning electron microscopic (SEM) image of a nanoribbon transistor is shown in Figure 3.4a. At pH below 6, we used HCl and above 8, we used NaOH, with pH solutions strictly prepared in laboratory, controlled with a pH meter and inserted via microfluidic channels on top of the device. This is to avoid complex solutions with too many ions (commercially available), here we started with 1M HCl and made serial dilution to get successive values between pH 0 to pH 6 and equivalently starting with 1M NaOH to get values between pH 14 to pH 8.

Figure 3.4b shows the plot of surface potential Ψ_0 versus pH response of the large ISFET, is well fitted with the SBM [9] considering typical parameters for a SiO_2 sensing layer, e.g., pK_a = -2, pK_b = +6 dissociation constants of SiOH into $SiOH^{2+}$ and SiO^-, respectively and a total density of sites $N_s = 5x10^{18}/m^2$. The pH response of this large ISFET is within the usual Nernst limits for pH sensors with slopes between zero and -59 mV/pH the maximum theoretical sensitivity for Ψ_0. Figure 3.4c shows drain-current (I_D) versus $V_{Ag/AgCl}$ at different pH values. The threshold voltage V_{th} is determined from $V_{Ag/AgCl}$ at a fixed $I_d = I_{th}$. For SiO_2, it is usually considered that the point zero charge (PZC: total surface charge = 0) is at pH=2. Threshold voltages V_{th} were converted into surface potential via $\Psi_0 = V_{th}(PZC)-V_{th}$.

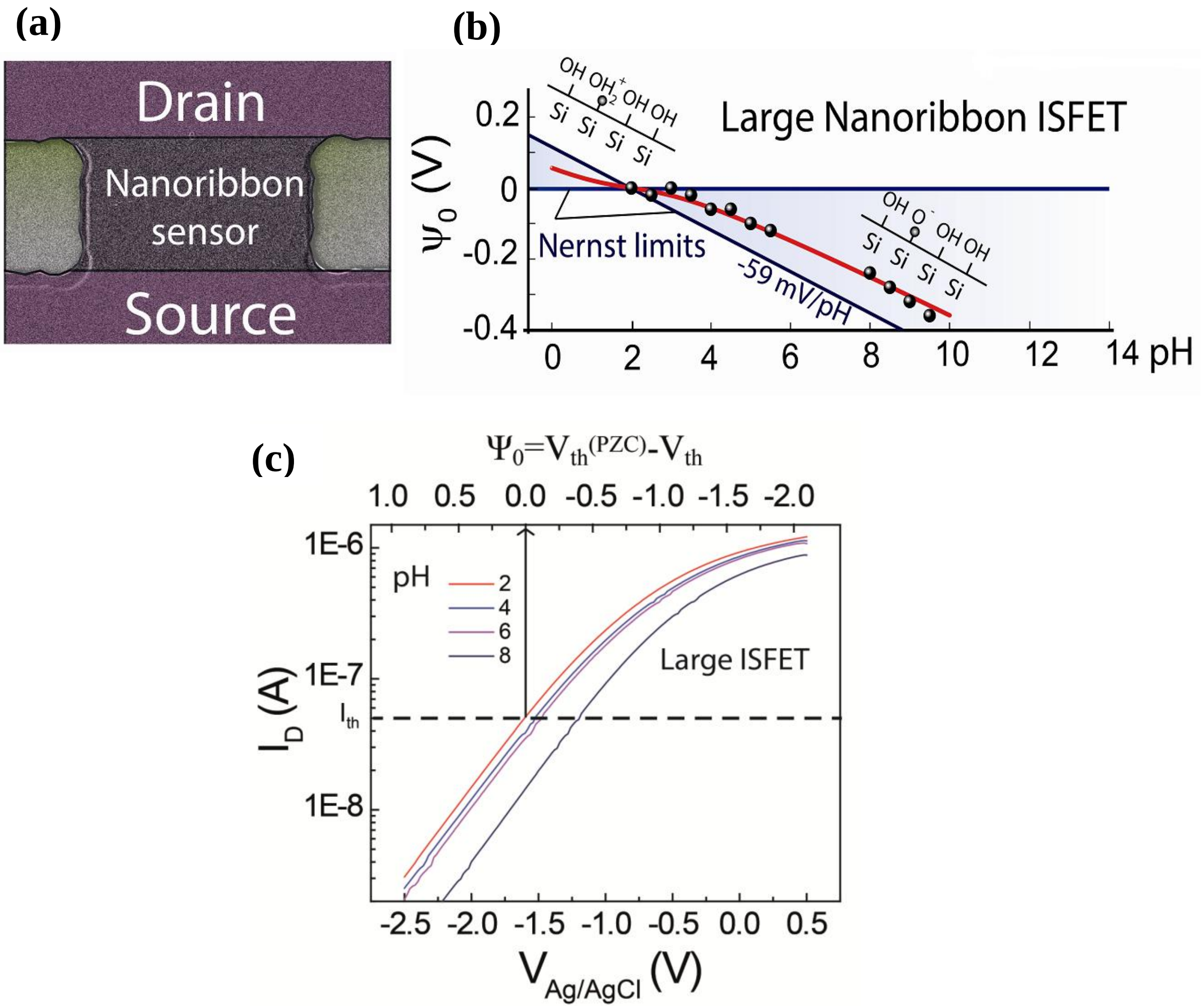

Figure 3.4(a) Scanning Electron Microscope (SEM) image of a nanoribbon ISFET (W= 10 µm, L= 7 µm, thickness = 40 nm) used as a reference sample to extract the properties of our hydrated thermal SiO_2 and to illustrate conventional pH response obtained with the Site Binding Model (SBM). **(b)** Plot of the surface potential Ψ_0 versus pH for the large ISFET. Solid black balls represent experimental data points whereas red line is the theoretical fit with SBM (red) and blue lines are theoretical borders of SBM often called Nernst limits for pH sensors shown in Figure 3.1a, 3.3a and 3.3b. The measured threshold voltage V_{th} were converted to surface potential via $\Psi_0=V_{th}$ (PZC)-V_{th} **(c)** raw transistor characteristics (drain-current - $V_{Ag/AgCl}$ at different pH values for the large nanoribbon ISFET) and extraction of Ψ_0. The point zero charge pH value is set to PZC=2 as usual for SiO_2.

3.2.3. Ψ_0 - pH response of the 0D ISFET

At the opposite, we discovered for 0D ISFETs (SEM picture of which is shown in Figure 3.5a) an unexpected U-shape response that breaks the usual Nernst limits and monotonic response of pH sensors. Figure 3.5b shows plot of surface potential Ψ_0 versus pH for the 0D ISFET, and Figure 3.5c shows drain-current (I_D) versus $V_{Ag/AgCl}$ curve at different pH values. The threshold voltage V_{th} is determined from $V_{Ag/AgCl}$ at a fixed $I_d = I_{th}$. At first order approximation, it can be seen as two back-to-back curves composed of a plateau and a slope of ~ ±59 mV/pH with a symmetry axis at pH = 6 (pH range of DI water).

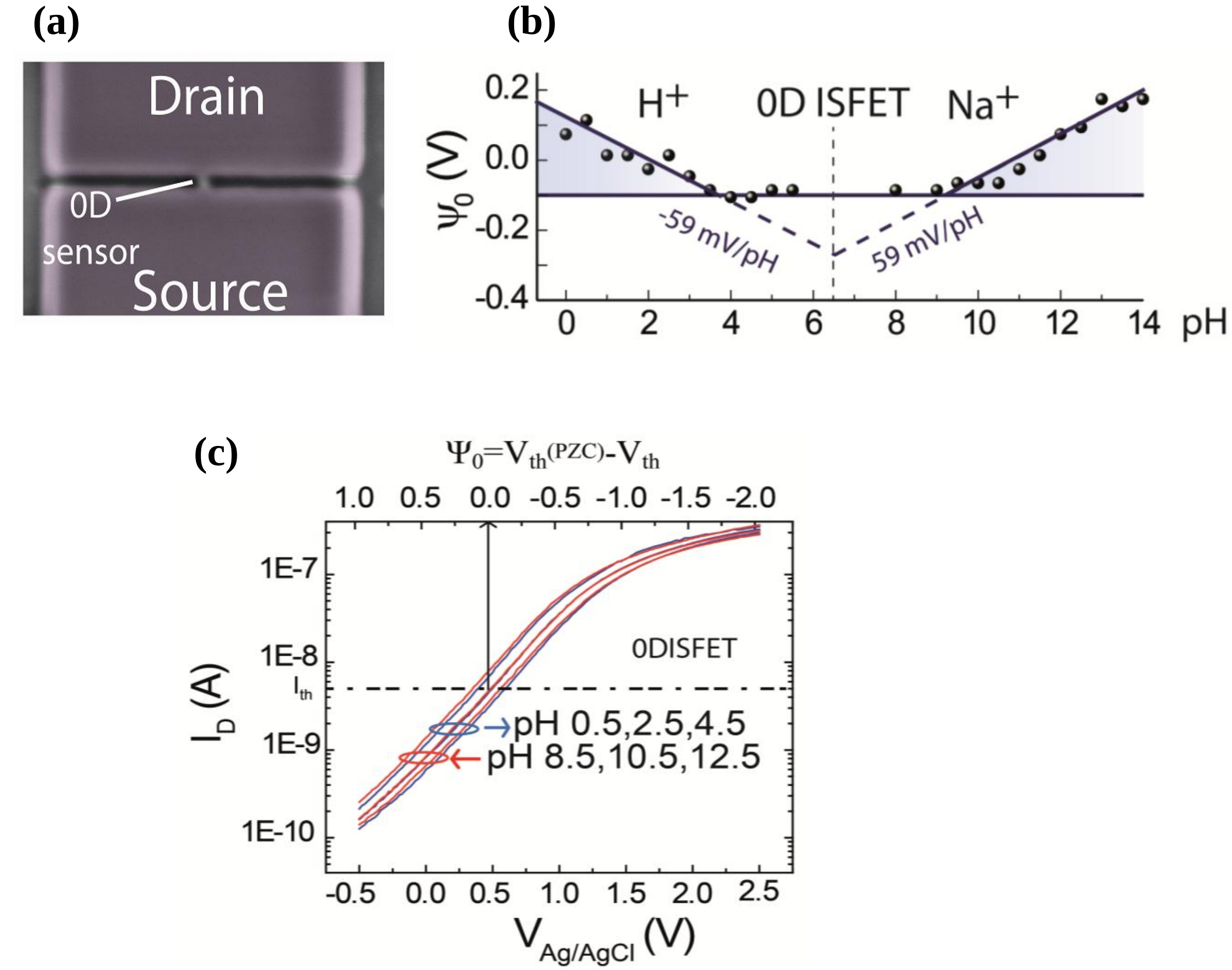

Figure 3.5 (a) Scanning Electron Microscope (SEM) image of 0D ISFET (after thermal oxidation, silicon channel width W = 15 nm and length L= 25nm are obtained) **(b)** Plot of the surface potential Ψ_0 versus pH for the 0D ISFET. Solid black balls represent experimental data points with a U-shape curve. Blue lines are asymptotic guides for eyes. Shaded areas in Figure are used to highlight the rupture in concept between conventional and 0DISFET devices. Due to uncertainty in exact pH value near pH=7, point are not represented in this pH range **(c)** drain-

current (I_D) versus $V_{Ag/AgCl}$ curve at different pH values for 0D ISFET. From the curve threshold voltage V_{th} were converted to surface potential via $\Psi_0=V_{th}$ (PZC)-V_{th}

This result, obtained reproducibly with four identical 0D ISFETs measured as shown in Figure 3.6a to 3.6d, cannot be fitted with the SBM considering dissociation of SiOH into SiO^- because at pH > pK_b = +6, surface charge should be negative (SiO^- sites), resulting in a negative Ψ_0 (see Figure 3.8 for simulations) as found for the large ISFET. The presence of Na^+ ions from NaOH could eventually bind to the SiO^- sites resulting in a reduced density of negatively charged sites [24], but not in a positive Ψ_0, unless a complex overcharging mechanism with electrostatically attracted Na^+ ions occurs.

The U-shape pH response and Ψ_0 mainly > 0 suggest that 0D ISFETs are a new type of sensors, only sensitive to cations (H^+ or Na^+) as it is clearly shown in Ψ_0 versus pH plot. It is a unique opportunity to address the contribution of weakly electrostatically bound cations and cation's complexes in surface potential without a correlated complex contribution of the site binding model. Below in the following section 3.4 and 3.5, we discuss the number of charged sites and a possible "nanoscopic" picture of surface functional groups on top of the nanotransistor.

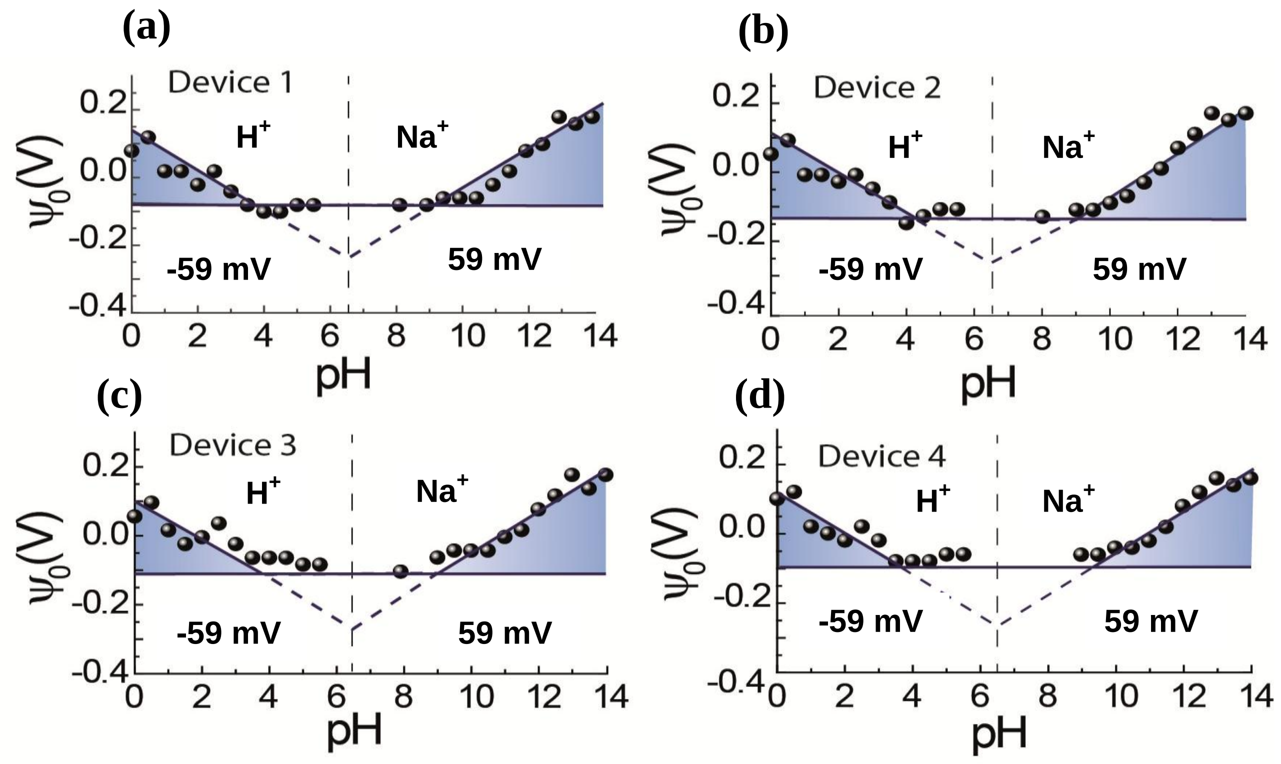

Figure 3.6 (a)-(d) Plot of the surface potential Ψ_0 versus pH for four identical device of 0D ISFET measured simultaneously showing similar results. It is seen that two back-to-back curves composed of a plateau and a slope of ~ ±59 mV/pH with a symmetry axis at pH = 6.

3.3. Understanding the U-shape pH response:

3.3.1. Discussion on the number of charged sites on 0D ISFET

Figure 3.7a is a schematic representation of the nanotransistor interface showing the partly hydrated counter Na^+ ions and the various surface functional groups that may cover silica surface (SiO_2) for NaOH at pH ≥ 8. Figure 3.7b shows estimation of the density of SiOH, SiO^- and $SiOH_2^+$ sites and their number on 0D ISFET's SiO_2 sensing layer as a function of pH based on the SBM using $pK_a = -2$, $pK_b = +6$ and a total density of sites between $N_s = 5x10^{18}$ m^{-2} (black line) and $N_s = 10^{16}$ m^{-2} (blue line) for SiOH groups. Black lines in Figure 3.7b shows the density and the number (more relevant for this nanoscale sensor) of SiOH, SiO^- and $SiOH_2^+$ sites at the SiO_2 / liquid interface as a function of pH estimated with the SBM using Eq 3.8, 3.9 and 3.10, the density found for the large silicon nanoribbon transistor fabricated with same thermal oxidation process. The probability of having $SiOH_2^+$ sites is negligible except at very low pH. The number of SiO^- sites is also low (between few and hundreds of sites) but should be enough to observe the universal monotonic pH response predicted by the SBM (variation of Ψ_0 induced by these charged surface functional groups at pH = 10 is estimated to be ~ -320 mV see Figure 3.8b).

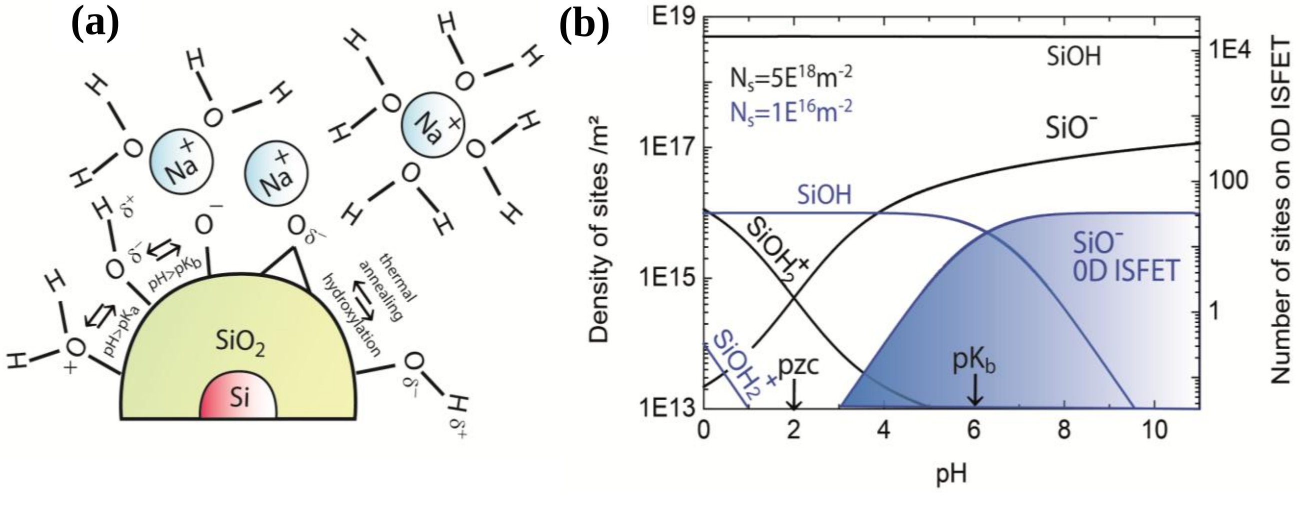

Figure 3.7 (a) Schematic cross section view of the 0DISFET showing typical surface functional groups at the surface of SiO_2, and Na^+ counter ions (for NaOH, at pH ≥ 8) **(b)** Estimation of the density of SiOH, SiO^- and $SiOH_2^+$ sites and their number on 0DISFET's SiO_2 sensing layer as a function of pH based on the SBM using $pK_a = -2$, $pK_b = +6$ and a total density of sites $N_s = 5x10^{18}$ m^{-2} and $N_s = 10^{16}$ m^{-2}. Because we don't observe the monotonic pH response, the later value of N_s is considered as an upper estimation for 0D ISFETs. When N_s is low (e.g $N_s = 10^{16} m^{-2}$), the SBM predicts a reduction of [SiOH] with pH, leading to $N_s = [SiO^-]$ at high pH. The SiO_2 sensing layer area is $2.75x10^{-15}$ m² (35 nm-thick SiO_2 gate oxide).

Because we don’t observe the universal monotonic pH response, and instead observe a full-Nernstian response to Na^+ at pH > 9 (strictly speaking, best fit corresponds to a super-Nernstian response that will be discussed briefly in the next chapter), we suggest that either the device is insensitive to charged surface functional groups or their density is low enough so their contribution in surface potential remains in the measurement noise. In the second hypothesis, a maximum density N_s=10^{16} m^{-2} (see Figure 3.8c) can be extracted from the standard deviation of ~30 mV to the Nernstian response (upper estimation). This corresponds to 30 SiO^- sites at maximum shown in Figure 3.7b or 3.8a on the nanotransistor.

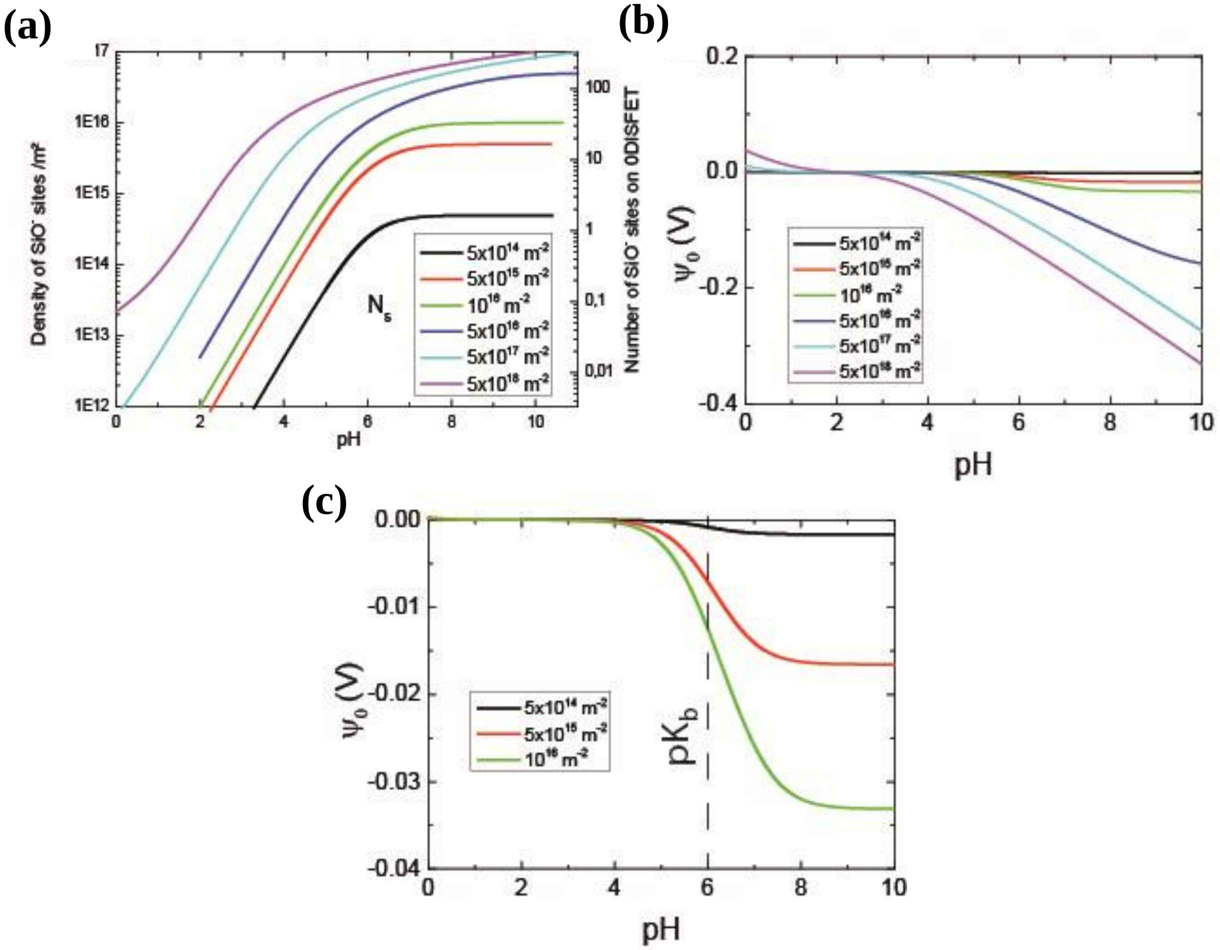

Figure 3.8 (a) Density of SiO^- sites and their number on the 0DISFET’s SiO_2 sensing layer as a function of pH based on the SBM using $pK_a = -2$, $pK_b = +6$ and different densities N_s of available sites (corresponds to [SiOH] at pH=2). The SiO_2 sensing layer area is 2.75×10^{-15} m² (35 nm-thick SiO_2 gate oxide) **(b)** Estimation of the surface potential Ψ_0 as a function of pH for different N_s. **(c)** zoom on (b) for lowest N_s. A density of 10^{16} m^{-2} corresponds to only 30 SiO^- sites at maximum on the 0D ISFET (see c) resulting in a shift of 30 mV that could’nt be clearly distinguished in experimental datas. Above N_s =10^{16} m^{-2}, we believe that we would have detected the signal arising from SiO^- sites (ex 400 mV for $N_s = 5\times10^{18}$ m^{-2}).

3.3.2. Drift measurement on 0D ISFET

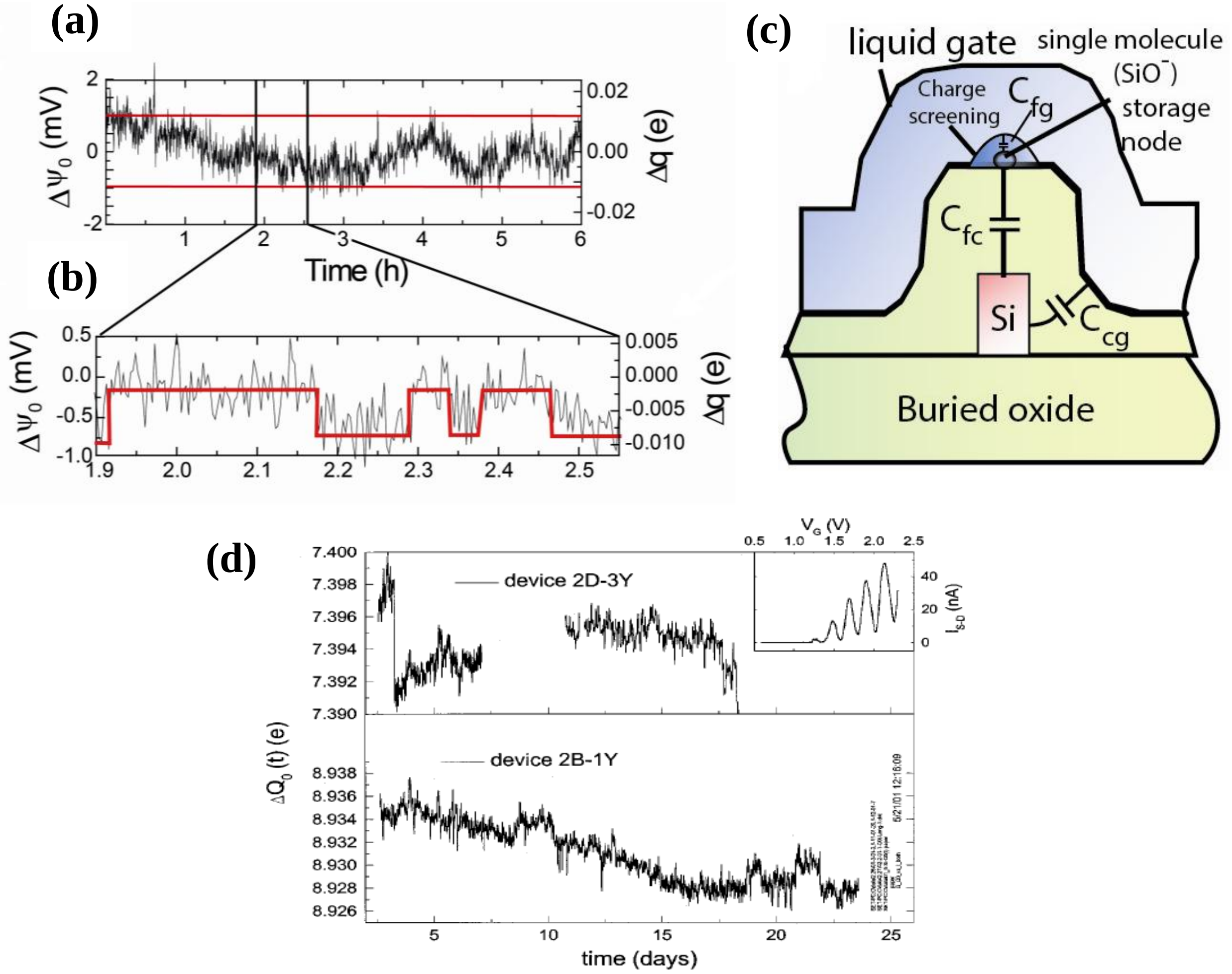

Figure 3.9 (a) Time-dependent fluctuation of Ψ_0 and equivalent charge fluctuation Δq across the gate capacitor as a function of time for a device without defect. Transconductance $g_m = 7.8\text{x}10^{-9}$S, gate capacitance C_g = 2aF, current drift is below 1% (range 2.67-2.69 nA), gate voltage V_g = 0V. **(b)** Zoom from Figure (a) with a red line as a guide for eyes to highlight discrete events. The amplitude could correspond quantitatively to the equivalent charge fluctuation induced by the reversible transition of a single SiOH site into SiO^- site **(c)** Schematic cross-section of a single molecule memory in liquid-gate showing capacitive coupling with the various elements (C_{cg}, C_{fc} and C_{fg}) **(d)** Figure adapted from reference 26. Measurement of long-term drift in Q_0 (t) as a function of time showing stability of ΔQ_0 (t) < 0.01e, under vacuum and at temperature below 0.1 K

To further discuss the number of charged sites, we also performed drift measurements. Indeed, a common feature (drawback) of ISFETs is the surface potential drift that is attributed to the slow charging state change of surface or buried -OH sites [25]. Figure 3.9a shows the time-dependent fluctuation of the 0D ISFET surface potential for 6 hours at pH=6. We observe a strong suppression of drift corresponding to Δq=0.025 equivalent elementary charge e over the whole period of time, only one order of magnitude larger than the value measured by other groups (see Figure 3.9d) with similar devices under vacuum and at temperature below 0.1 K [26]. We consider variation of input charge as:

$$\Delta q = C_{cg}.\Delta V_{th} \qquad \text{Eq 3.11}$$

where C_{cg} is capacitance between the liquid gate and the silicon channel, and ΔV_{th} the variation of threshold voltage induced by this variation of charge across the gate capacitance. We used Eq 3.11 to obtain Δq in Figure 3.9a, 3.9b, and 3.10b respectively. Discrete events shown in Figure 3.9b (Δq ~ 0.008 e) seem to be superimposed to the intrinsic low-frequency noise fluctuation [27, 28] and residual thermal drift. It could quantitatively correspond to a reversible chemical reaction at single bond level (SiOH ↔ SiO^-), with SiO^- charged sites strongly screened by the double layer capacitance. Figure 3.9c shows schematic cross-section of a single molecule memory in liquid-gate showing capacitive coupling with the various elements. N.Clement et al. [28] shown previously that Δq ~ e where e is the elementary charge when a single-electron is trapped / detrapped near the electron channel in the sub-threshold region. This leads to C_{cg} ~ 2aF from Figure 3.10b, typical value for these devices. If we consider the fluctuation of a single chemical bond, we have to consider its partial screening from the double layer capacitance. By analogy with a single-electron memory reported in reference 40 (see schematic Figure 3.10a), we propose a representation for the single molecule memory (discussed above in Figure 3.9c). In both cases, the variation of an elementary charge in the storage node induces a variation of threshold voltage ΔV_{th}:

$$\Delta V_{th} = \frac{e}{C_{fg} + \left(1 + C_{fg}/C_{fc}\right)C_{cg}} \qquad \text{Eq 3.12}$$

where C_{fg} is the capacitance between the storage node in single electron or single molecular memory and the liquid gate, C_{fc} is the capacitance between the storage node in single electron or single molecular memory and the silicon channel. The main difference between the single-electron memory and the single molecule memory is the magnitude of capacitance C_{fg}. Indeed, in the single-electron memory configuration $C_{fc} >> C_{fg}$, but in the single-molecule memory configuration $C_{fg}/C_{fc} \sim \varepsilon_{water}.t_{ox}/(\varepsilon_{SiO2}.r_H) \sim 1/117$, where ε_{ox} is the relative dielectric permittivity of SiO_2, ε_{rwater} is the relative dielectric permittivity of water, r_H is the Helmoltz radius (3.5 nm) and t_{ox} is the gate oxide thickness (~20 nm). The table below summarizes the main differences.

	Single-electron memory	Single-molecule memory
C_{cg}	2 aF	2 aF
Remark	$C_{fc}>>C_{fg}$	C_{fg}/C_{fc}~117
ΔV_{th}	~q/C_{cg}	~$q/117C_{cg}$ ~$0.008\ q/C_{cg}$

Table 3.1 Table summarizes the main difference between the single-electron and single-molecule memory.

As a comparison, the equivalent-charge amplitude fluctuation for a single-electron trapping/detrapping in a defect near the electron channel (e.g. dangling bond in SiO_2 gate oxide) is much larger because of screening by the liquid gate is weak (see Figure 3.9c, 3.10a) [27, 29].

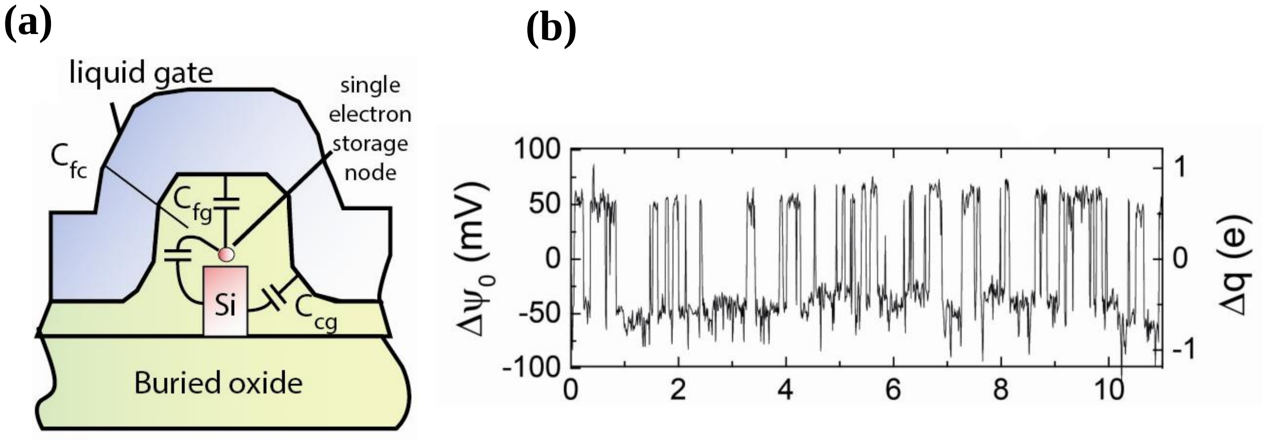

Figure 3.10 (a) Schematic cross-section of a single electron memory in liquid-gate showing capacitive coupling with the various elements (C_{cg}, C_{fc} and C_{fg}) **(b)** time domain electrical characteristic when a single active defect is near the channel with single-electron trapping / detrapping (large fluctuation amplitude) with 60% current fluctuation (100 pA-160 pA). V_g = -0.96 V, $g_m = 4.65x10^{-10}$ S, C_{cg} = 2 aF.

The low density of charged sites on these 0D nanotransistors could be related to the presence of the two neighboring source and drain contacts (see the SEM picture of OD ISFET). During the high temperature thermal oxidation process, oxidation rate / stress is different between the large pads and the nanoconstriction where large stress occurs [23]. In other words, both oxides are not necessarily identical. Secondly, source and drain are electron reservoirs, which may tend to attract cations at the interface [19]. As a consequence, the presence of large contacts near the nanotransistor may affect hydroxylation [30] or dissociation kinetics, leading to a reduced density of charged surface functional groups on the nanotransistor. Also, siloxane and silanol groups (as shown in the schematics of Figure 3.7a) contain negative dipoles that tend to attract cations. A more detailed "nanoscopic" picture would require a chemical analysis at nanoscale, beyond abilities of actual state of the art equipments such as NanoFTIRs [31]. Extended border discussions on the "nanoscopic" picture including additional experiments are discussed in the following section below.

3.4. Broader discussion on the "nanoscopic" picture of 0D ISFET

3.4.1. Pattern-dependant oxidation

The pattern-dependent oxidation (PADOX) process, in which the oxidation is strongly affected by the initial structural size and shapes that, has been extensively studied since the first fabrication of the silicon single-electron transistor with this technique [32]. Figure 3.10a and 3.10b shows a simulation of the stress and strain map around the nanoconstriction taken from paper [41]. The characteristic features of PADOX are mainly determined by the oxidation-induced strain and by the oxidation below due to oxygen diffusion through the buried oxide layer, by which the silicon on the oxide is pushed upward due to dilatation with oxidation [33]. As far as the application of 0D nanotransistor biosensors is concerned the oxide strain may play a significative role in the surface chemistry around the nanoconstriction, which may lead to a reduced density of charged surface functional groups with more silanol or siloxane groups than expected for standard SiO_2.

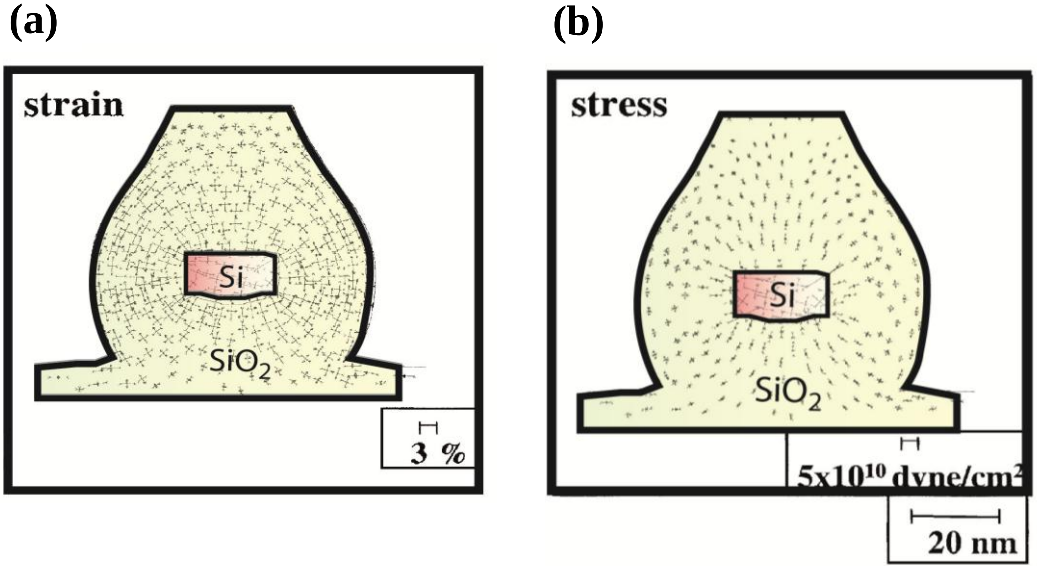

Figure 3.11 (a) Strain and **(b)** stress obtained from the simulation of dry oxidation at 1000°C for 80 mn. Figure adapted from the above mentioned reference [41]. Colors have been added for clarity.

3.4.2. Hypothesis of siloxane bonds at the nanoconstriction

It is known that after a thermal annealing at 1000°C, SiO_2 surface is mainly covered by siloxane groups (Si-O-Si) and is hydrophobic (from reference 30 the distribution plot of surface charge groups as function of temperature is shown in Figure 3.12c). It can be rehydroxylated (SiOH sites) with plasma O_2 and hydration. We confirmed this behavior with contact angle measurements, and the optical picture of which before and after plasma is shown in Figure 3.12a and 3.12b respectively. Such measurements can only be performed at macroscopic scale (~ mm²) droplet and can't provide informations on eventual pattern-dependent chemistry at nanoscale as described in Figure 3.12c and 3.12d showing its schematic view.

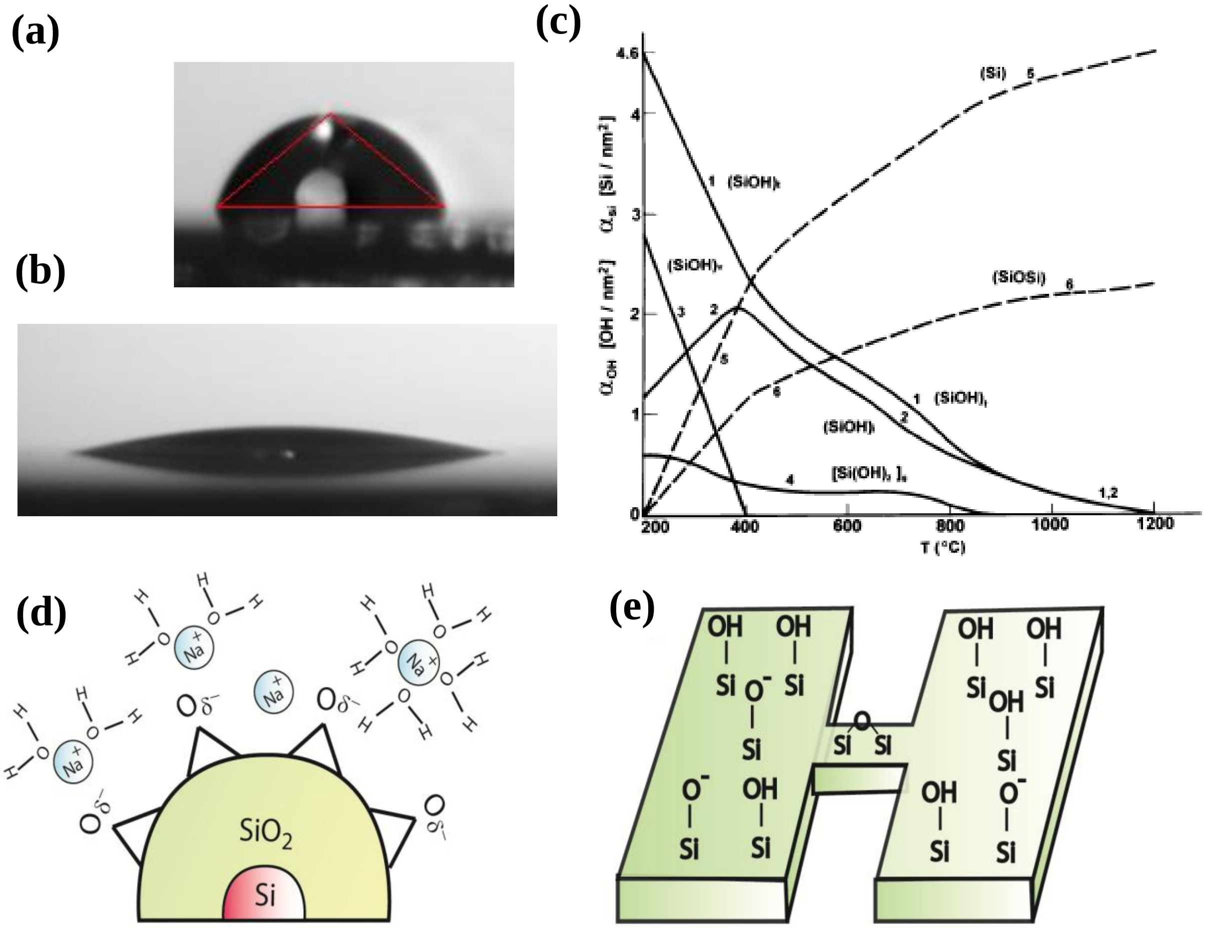

Figure 3.12 (a) Contact angle (~74°) at the end of the device fabrication, before insertion in a lab-on-chip **(b)** Contact angle (~14°) after plasma O_2 at 120 W and 0.7 mbar for 180 s, a step necessary for PDMS-based lab-on-chip fabrication (as discussed in Chapter1 and Chapter2). **(c)** Distribution plot of surface charge groups as a function of temperature. Figure adapted from reference 30 **(d)** Schematic cross section view of the 0D ISFET in the hypothesis of unhydroxylated silica at the nanoconstriction (fully covered with siloxane bonds). The charge of

siloxane bond is neutral but strong dipoles tend to attract cations **(e)** Schematic 3D view of the 0D ISFET's SiO_2 interface showing a proposed pattern-dependent surface chemistry with mainly silanol groups on large access leads and siloxane groups on top of the nanoconstriction.

Using an Atomic Force Microscope (AFM) in peak-force mode (see Figures 3.13a, 3.13b and 3.13c), we obtained the adhesion map on the nanotransistor. The adhesion is related to the presence of a water meniscus between the tip and the surface. It is therefore related to hydrophobicity. Each pixel is 1 nm. If a local hydrophobic zone would have been located only at the nanoconstriction, one would have expected a clear contrast at the nanoconstriction on the adhesion image. At this stage, there is no clear evidence (without topography cross-talk) of such hydrophobic zone and therefore a coverage with siloxane bonds at the nanoconstriction.

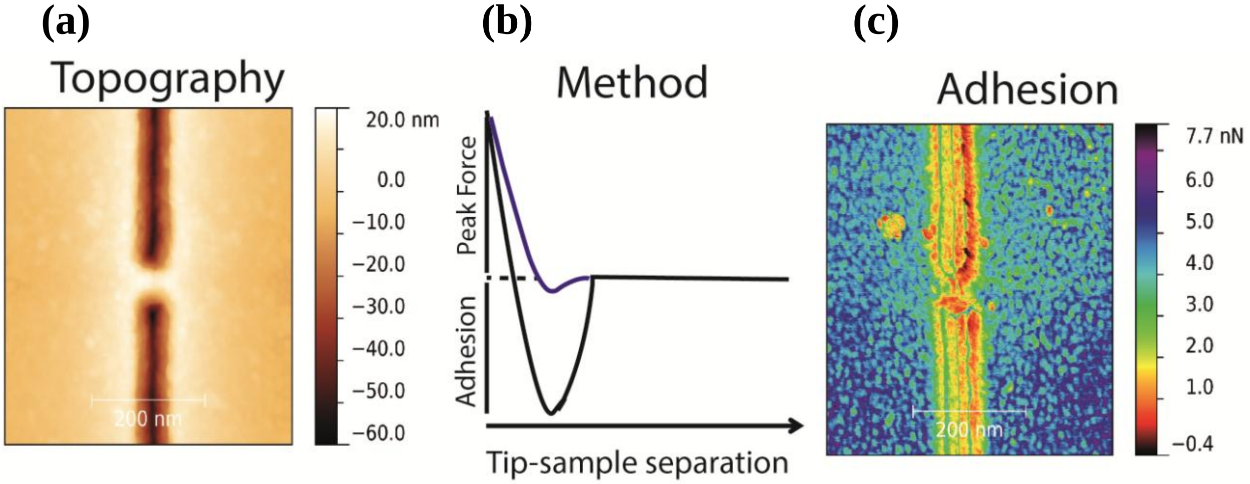

Figure 3.13 (a) Topography AFM image of the 0D ISFET. **(b)** Schematic graph of a typical force-distance curve done with an AFM. **(c)** Using Peak-force AFM (Brüker), at each pixel, a force-distance curve is done, which allows plotting the adhesion map, each pixel is 1 nm.

3.4.3. Hypothesis of Field-effect charge attraction from "Normally-on" neighboring MOSFETs

A. Fujiwara et al. [34] have shown that the threshold voltage of such silicon single electron transistor is significantly larger than the threshold voltage of the same structure without constriction. In other words, the two un-doped large silicon pads facing the nanoconstriction can be seen as "Normally-on" series MOSFETs. This structure has the great advantage to avoid the problem of dopants diffusion in such small devices. Figure 3.14a illustrates the shift of threshold voltage, measured in liquid, for both the large nanoribbon and the 0D ISFET. Figure 3.14b illustrates the consequence of this observation in a capacitive attraction of cations near the surface. Unlike µm-long silicon nanowires, this capacitive cation attraction may affect the electric field map in liquid around the nanoconstriction, with a potential impact on surface chemistry or overcharging effects. However, the SiO_2 oxide thickness is large (~35 nm) and according to a recent theoretical study [35], the field-effect control of surface charge property would be negligible in our device, in particular because we don't apply large biases (10 V). At pH > 2, large pads have also negative charges at the surface that may affect electric field in liquid around the nanoconstriction.

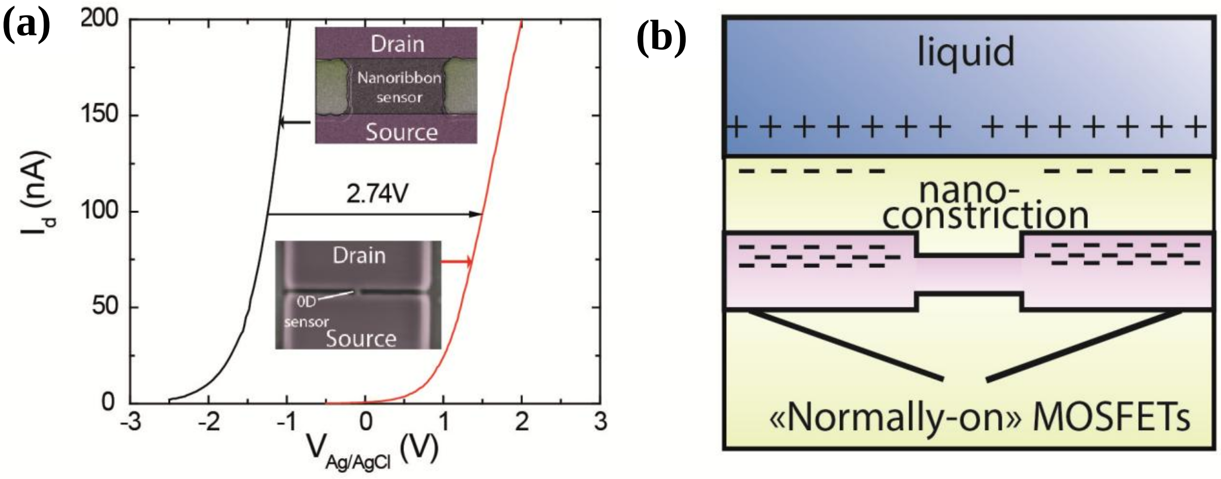

Figure 3.14 **(a)** I_d-$V_{Ag/AgCl}$ curves for a silicon nanoribbon transistor and a 0D ISFET showing the shift of threshold voltage to higher voltages for the smallest device **(b)** Simplified schematic cross-section view of the two "large" MOSFETs in the "on" state (accumulation of electrons in the channel) whereas the nanoconstriction is at its threshold voltage.

3.4.4. Hypothesis of a different pK_b at the nanoconstriction

Another alternative to a small density of charged sites would be a different value of pK_b for SiO_2 at the nanoconstriction (see Figure 3.15a) as a result of stress in oxide (from Figure 3.11) or the presence of the two large pads (as discussed in the previous section 3.5.3). Value of pK_b (sometimes defined as pKa depending on the way the equation is written) is typically between 6 and 6.8 [4, 35]. In case of pK_b shifted to higher values, the constriction would be mainly covered by silanol bonds. Silanol bonds can also attract cations from their intrinsic dipole as shown in schematic Figure 3.15b. The unexpected full Nernstian response near pH ~ 7 with SiO_2 oxide for a 200 nm-long active zone [14] was not discussed, but could be explained at the opposite by a strong shift of pK_b to lower values. This could be related to the increase in the density of negatively charged sites due to the small nanowire radius (similar to the observation with silica nanoparticles [15]).

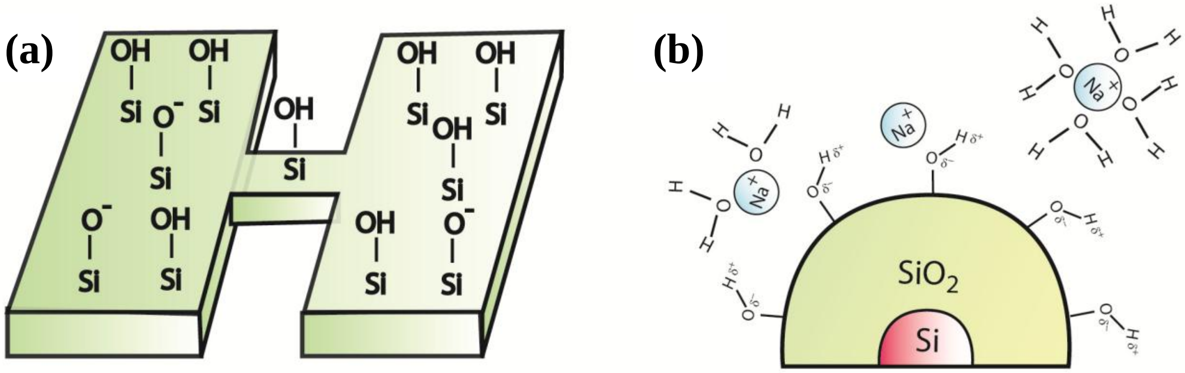

Figure 3.15 (**a**) Schematic 3D view of the 0DISFET's SiO_2 interface showing a proposed pattern-dependent surface chemistry with mainly silanol and SiO^- groups on large access leads and silanol groups on top of the nanoconstriction **(b)** Schematic cross section view of the 0D ISFET in the hypothesis of silica with large pK_b at the nanoconstriction (fully covered with siloxane bonds). The charge of silanol bond is neutral but strong dipoles tend to attract cations.

3.4.5. Discussion on above hypotheses

The aim of this section "Broader discussion on the "nanoscopic picture" was to provide all elements of discussion to the scientific community to help us explain our results. It seems that overcharging effect is likely at the origin of the U-shape pH response and super-Nernstian characteristics. Also, as discussed above the density of sites N_s is likely lower at the nanoconstriction than on the large pad, but we can't reach an exact picture of surface functional groups because several hypotheses are plausible. State of the art equipment such as peak force AFM couldn't allow us to conclude on this specific point in this study. Answer may come in the future with progress in chemical images at nanoscale with a nano-FTIR with molecular resolution!

3.5. Summary

Using 0D nanotransistor biosensors (25nm long and 15nm wide) we have shown a rupture in the universal monotonic response to U-shaped pH response, with apparently few charged surface functional groups at the nanoconstriction region. The surface potential Ψ_0 mainly greater than zero suggest that 0D ISFETs are a new type of sensors, only sensitive to cations of H^+ and Na^+ in the acid-base solutions due to presence of few SiO^- sites. Although a "nanoscopic picture" of the 0D nanotransistor biosensors surface chemistry is not fully achieved yet, we have evidenced from the U-Shape pH response and drift measurements that there are likely only few charging sites at the maximum on top of the nanotransistor. This doesn't discard presence of negative dipoles at the surface. In the next chapter we will go deeper in the mechanism on cation sensing and will propose an application.

Bibliography

[1] Cremer, M. Über die Ursache der elektromotorischen Eigenschaften der Gewebe, zugleich ein Beitrag zur Lehre von Polyphasischen Elektrolytketten.-Z. Biol. 47: 56 (1906).

[2] Xiansheng K, Jing S (2014) Design and implementation of food intelligent monitoring system based on pH sensors. J. Chem. Pharm. Res. 6(7): 1662-1666.

[3] Arun Arora, Application of biomedical sensors for monitoring of drinking water, Imperial college London http://www3.imperial.ac.uk/pls/portallive/docs/1/35091697.PDF

[4] Rothberg JM et al (2011) An integrated semiconductor device enabling non-optical genome sequencing Nature 475:348–352.

[5] Marban E et al (1980) Free calcium in heart muscle at rest and during contraction measured with Ca^{2+} sensitive microelectrodes Nature 286:845-850.

[6] Comiskey B, Albert JD, Yoshizawa H, Jacobson J (1998) An electrophoretic ink for all-printed reflective electronic displays. Nature 394:253-255.

[7] Siria A et al (2013) Giant osmotic energy conversion measured in a single transmembrane boron nitride nanotube. Nature 494:455-458.

[8] Hood JD, Bednarski M, Frausto R, Guccione S, Reisfeld RA, Xiang R, Cheresh DA (2002) Tumor Regression by Targeted Gene Delivery to the Neovasculature. Science 28 (296):2404-2407.

[9] Yates DE, Levine S, Healy TW (1974) Site-binding Model of the Electrical Double Layer at the Oxide/ Water Interface. Chem. Soc., Faraday Trans. 70:1807-1818.

[10] van Hal REG, Eijkel JCT, Bergveld P (1996) A general model to describe electrostatic potential at electrolyte oxide interfaces. Adv. Colloid. Sci 69:31-62.

[11] Sørensen, S. P. L. (1909). "Enzymstudien. II: Mitteilung. Über die Messung und die Bedeutung der Wasserstoffionenkoncentration bei enzymatischen Prozessen". Biochemische Zeitschrift (in German) 21:131-304.

[12] Cui Y, Wei Q, Park H, Lieber CM (2001) Nanowire Nanosensors for Highly Sensitive and Selective Detection of Biological and Chemical Species. Science 293 (553 3):1289-1292.

[13] Stern E et al (2007) Label-free immunodetection with CMOS-compatible semiconducting nanowires. Nature Letters 445:519-522.

[14] Tian B, Cohen-Karni T, Qing Q, Duan X, Xie P, Lieber CM (2010) Three-Dimensional, Flexible Nanoscale Field-Effect Transistors as Localized Bioprobes. Science 329 (5993):830-834.

[15] Barisik M, Atalay S, Beskok A, Qian S (2014) Size Dependent Surface Charge Properties of Silica Nanoparticles. Phys. Chem. C 118 (4):1836–1842.

[16] Nakajima H, Esashi M, Matsuo T (1982) The Cation Concentration Response of Polymer Gate ISFET. J. Electrochem. Soc. 129(1):141-143.

[17] Fu W et al (2011) Graphene Transistors Are Insensitive to pH Changes in Solution. Nano Letters 11 (9):3597-3600.

[18] Larrimore L et al (2006) Probing Electrostatic Potentials in Solution with Carbon Nanotube Transistors. Nano Letters 6 (7):1329-1333.

[19] Schasfoort RBM, Schlautmann S, Hendrikse J, van den Berg A (1999) Field-Effect Flow Control for Microfabricated Fluidic Networks Science 286:942-945.

[20] Duan C, Majumdar A (2010) Anamolous ion transport in 2-nm hydrophilic nanaochannels. Nature Nano. 5:848-852.

[21] Bousse L, de Rooij NF, Bergveld P (1983) Operation of chemically sensitive field effect sensors as a function of the insulator-electrolyte interface," IEEE Transactions on Electron Devices, 30 (10):1263-1270.

[22] Bergveld P (1970) Development of an ion-sensitive solid-state device for neurophysiological measurements IEEE Trans. Bio-Med. Eng. BME -17: 70-71.

[23] Takahashi Y et al (1995) Fabrication technique for Si single-electron transistor operating at room temperature. Electronics Letters 31(2):136-137.

[24] Shchukarev A, Rosenqvist J, Sjoberg S (2004) XPS study of the silica-water interface. J. Electron Spectroscopy 137:171-176.

[25] Bousse L, Bergveld P (1984) The role of buried OH sites in the response mechanism of inorganic-gate pH-sensitive ISFETs. Sensors and Actuators 6:65-78.

[26] Zimmerman NM, Hube WH (2001) Excellent charge offset stability in a Si-based single-electron tunneling transistor. Applied Physics letters 79:3188-3190.

[27] Clément N, Nishiguchi K, Dufrêche JF, Guérin D, Fujiwara A, Vuillaume D (2011) A silicon nanowire ion-sensitive field-effect transistor with elementary charge sensitivity. Applied Physics Letters 98 (1): 014104.

[28] Clément N, Nishiguchi K, Fujiwara A, Vuillaume D (2012) One-by-one trap activation in silicon nanowire transistors. Nature Communications 1:92.

[29] Li J, Pud S, Petrychuk M, Offenhäusser A, Vitusevich S (2014) Sensitivity Enhancement of Si Nanowire Field Effect Transistor Biosensors Using Single Trap Phenomena. Nano Letters 14 (6):3504-3509.

[30] Zhuravlev LT (2000) The surface chemistry of amorphous silica. Zhuravlev model. Colloids and Surfaces 173:1-38.

[31] Huth F, Schnell M, Wittborn J, Ocelic N, Hillenbrand R (2011) Infrared-spectroscopic nanoimaging with a thermal source. Nature Materials 10:352-356.

[32] Takahashi Y et al. (1994). IEEE IEDM Tech. Digest, 938-940.

[33] Nagase M, Fujiwara A, Yamazaki K, Takahashi Y, Murase K, Kurihara K (1998) Si nanostructures formed by pattern-dependent oxidation Microelectron. Eng. 41/42:527-530.

[34] Fujiwara A, Horiguchi S, Nagase M, Takahashi Y (2003) Threshold Voltage of Si Single-Electron Transistor. Jpn. J. Appl. Phys. 42:2429-2433.

[35] L.-H. Yeh et al (2012) Ion Concentration Polarization in Polyelectrolyte-Modified Nanopores. J. Phys. Chem. C 116 (15):8672-8677.

[36] Quesada-Perez M et al (2002) Electrophoretic mobility of model colloids and overcharging: Theory and experiment. Mol. Phys. 100:3029-3039.

[37] Bestemzn K et al (2004) Direct observation of charge inversion by multivalent ions as a universal electrostatic phenomenon. Phys. Rev. Lett. 93:170802.

[38] Kubickova A et al (2012) Overcharging in biological systems: reversal of electrophoretic mobility of aqueous polyaspartate by multivalent cations. Phys. Rev. Lett. 108 (18):186101.

[39] Lenz O, Holm C (2008) Simulation of charge reversal in salty environments: Giant overcharging? Eur. Phys. J. E 26:191-195.

[40] Guo et al (1997) Fabrication and characterization of room temperature silicon single electron memory. J. Vac. Sci. B 15(60):2840-2843.

[41] Uematsu M et al (2004) Two dimensional simulation of pattern-dependant oxidation of silicon nanostructures on silicon-on-insulator substrates. Solid-State Electronics 48:1073-1078.

4

Cation selectivity and Super Nerntzian sensitivity with 0D Nanotransistor Biosensors: Application to Blood Ionogram

In recent years the great progress in low cost, highly sensitive bio-detection and miniaturization of silicon-based nanosensors explore its application prospects in various fields. The outline of which is shown in the schematic Figure 4.1. Here, we show some of the main challenges to be improved in medical diagnosis and therapy towards biomedical application, using 0D nanotransistor in electrical biosensing technology with the aim to provide reliable and selective analysis of cation in the serum or blood which showed super Nerntzian sensitivity.

In order to reach high sensitivity and selectivity, a widely accepted concept is the use of ion-selective membranes for ion-selective measurements performed either with ion-selective electrodes (ISE) or with optical sensor devices (optodes). A review has listed more than 350 molecules tested for their selectivity [1]. The membrane composition usually contains several molecules with precisely defined concentrations. Although functional, this selective membrane concept suffers from several drawbacks. Extensive use of ISE may deposit or scoured with fine scratches on the membrane which lead to slow or reduced response (lower slope) and unstable results. Also prolonged immersion of the crystal membrane in aqueous solutions will eventually cause a build up of oxidation products on the membrane surface and thus inhibit performance and shorten the active life. In addition to molecules complexity and eventually non bio-compatibility; the main problems are durability (single-use in optode systems), the need of a specific membrane for each ion tested and interferences from other ions.

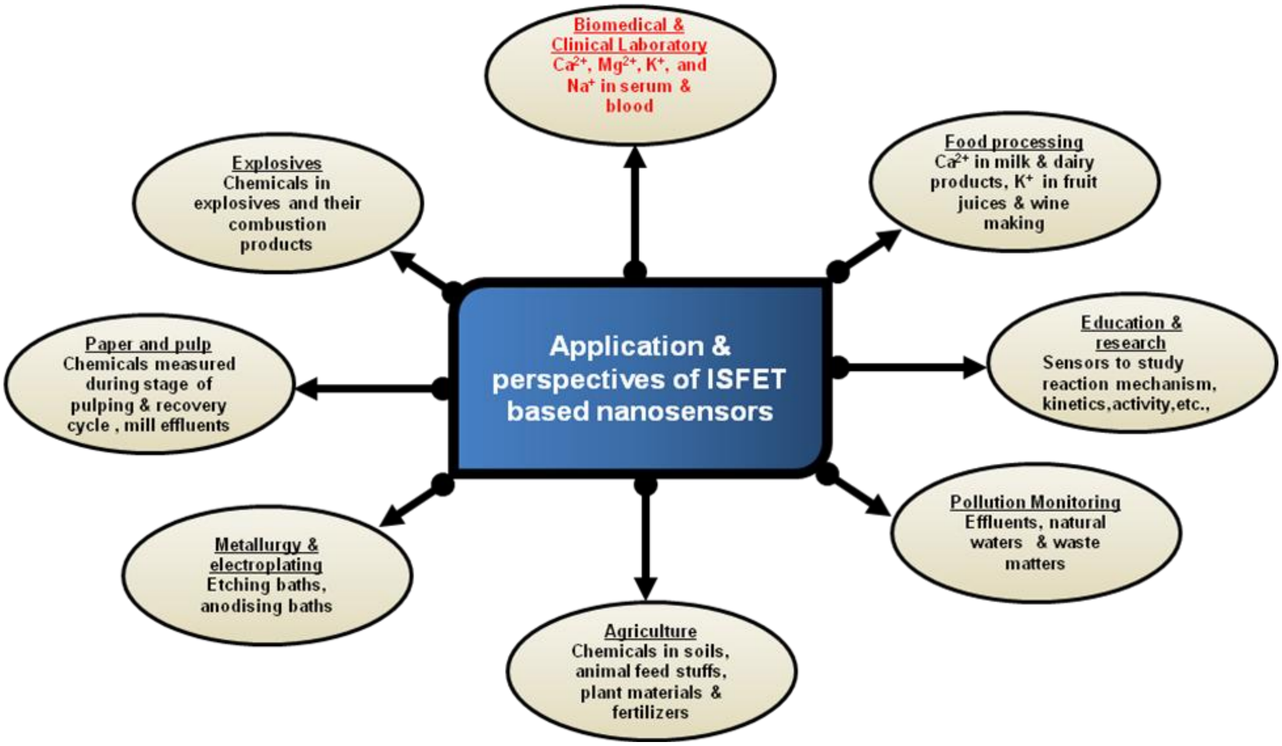

Figure 4.1 Schematic figures highlighting the use of ISFET based nanosensors in various applications of which we have shown super Nerntzian sensitivity of Na^+, K^+ Ca^{2+}, and Mg^{2+} in serum using our 0D ISFETs. This can be proof of principle towards biomedical field.

The other main concept is the so-called Nernst limit, where Ψ_0 has a maximum slope of 59 mV / log (a_i), where a_i is the ion activity. This 59 mV / decade limit is also the well-known inverse sub-threshold slope limit of transistors or diodes. It is derived from Poisson-Boltzmann equation in both site binding and semiconductor physics models and is equal to kT. ln(10) / ze where k is the Boltzman constant, T the temperature and z.e the charge of mobile particles / ions with e the elementary charge. As a result, sensitivities for multivalent ions are smaller than those for monovalent ions, which make selective detection of the former in the presence of the latter difficult. This problem cannot be solved using capacitive amplification of the Nernstian slope [2]. For this reason, some commercial biomedical systems include both ISE and optode systems for detection of monovalent and divalent ions, respectively (see Figure 4.2). This Nernst limit has been broken with specific membranes [1, 3]. For example, using natural polyether antibiotics with carboxyl groups [1], an apparent twice Nernstian response for divalent ions has been observed. It is potentially caused by the coexistence of primary and interfering ion complexes in ISE membranes [4]. To date, these “super Nernstian” ion-selective electrodes require better theoretical understanding to improve selectivity and reproducibility [4].

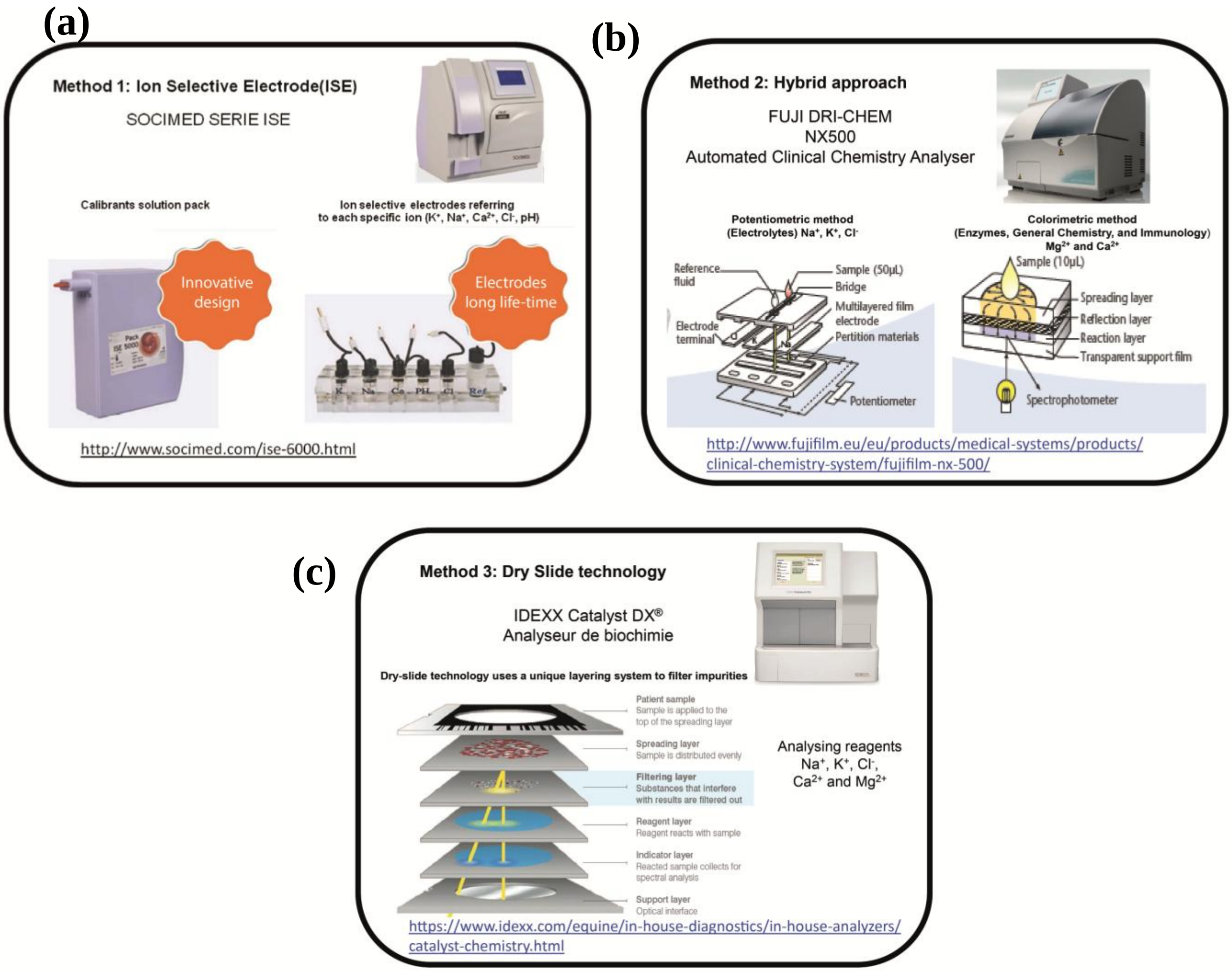

Figure 4.2 Schematic representation of 3 commercial equipments used to measure electrolytes concentration in serum; **(a) Method 1**: Socimed serie ISE: use only ISEs **(b) Method 2**: Fuji Dri-chem Nx500: hybrid approach using Potentiometric method for Na^+, K^+ and Cl^- , Colorimetric method for Ca^{2+} and Mg^{2+} **(c) Method 3**: Idexx catalyst dx: dry-slide technology, colorimetric method.

In this Chapter, using 0D nanotransistor biosensor, with apparently few effective charged surface functional groups, we also show a more than twice Nernstian sensitivity for Ca^{2+} and Mg^{2+} ions. We also propose a simple semi-empirical law for the cation sensitivity of these nanoscale sensors. Using the specificity of this equation, we demonstrate a new method for ion selectivity without need for selective coating layers on the nanotransistor. We show an application in biomedical diagnosis with the measurement of Na^+, K^+, Ca^{2+} and Mg^{2+} ions concentration in blood serum with the use of a single nanoscale transistor integrated on a millimeter square lab-on-a chip. Finally, we discuss the advantages of this new diagnosis technique and the impact of the proposed equation.

4.1. 0D ISFET's cation sensitivity

4.1.1. Nerntzian sensitivity to H^+, K^+, and Li^+ and super Nerntzian sensitivity to Na^+, Ca^{2+} and Mg^{2+} cations

To extend 0D ISFETs cation sensitivity to other cations than H^+ and Na^+, we have measured Ψ_0 for various salts at different ionic strengths and plotted results together with results for HCl and NaOH solutions shown in Figure 4.3a. The solution preparation of different salts with different ionic strengths has been described well in the Appendix. We selected $\Psi_0 = 0$ at pH = 6 and low ion concentration for easy comparison. Interestingly, we observe a similar response of Ψ_0 as a function of cation activity for all solutions. In particular, K^+ / H^+ related to KCl / HCl and Na^+ related to NaOH / NaCl show similar curves, which is again in favor of a weak impact of pH on surface functional groups. This response could be explained by a local measurement of the electrochemical potential of cation species in the solution without any site binding:

$$\Psi_0 = constant + \frac{A_i}{z_i}.\left(\sum_i \log\left(a_i + a_{i0}\right)\right) \qquad \text{Eq (4.1)}$$

z_i is the ionic valency of ion i including the sign, a_{i0} is a semi-empirical constant that may be related to free energy of interaction between cations and surface functional groups, cations hydration sheath, the influence of anion species, solution purity, and transistor design. A detailed analysis of this parameter is rather puzzling, however, as a_{i0} is significantly smaller for KH_2PO_4 than for KCl solutions (same K^+ ion), the anion may play a role in the value of a_{i0}, that remains in most cases ~ 5.10^{-4} M / L. Table 4.1 summarizes all extracted values of A_i, a_{i0} and possible relevant informations including counter ions, action charge, the effective cationic radius and the hydrated cationic radius of salts studied. A_i is in the range of 59 mV/ log (a_i). However, strict fitting of A_i with Eq

4.1 provides 59 < A_i < 140 mV/log (a_i). H^+, Li^+ and K^+ show a full Nernstian sensitivity, Na^+ a super Nernstian sensitivity and Ca^{2+}, Mg^{2+} a more than twice Nernstian sensitivity.

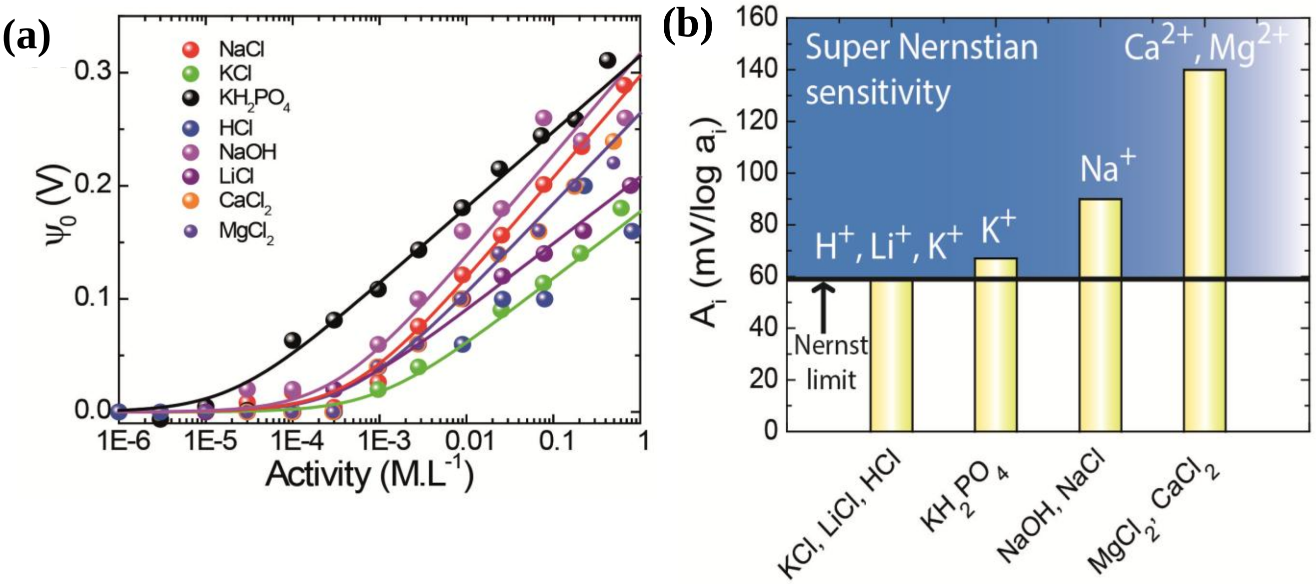

Figure 4.3 (a) Ψ_0 is plotted as a function of ions activity a_i for five different solutions (KH_2PO_4, NaCl, KCl, HCl, LiCl and NaOH). The solid line corresponds to the full Nernstian response (slope of +59 mV / log a_i). **(b)** A_i from fits of (a) with Eq 4.1 is plotted for all tested solutions. The Nernst limit of 59 mV / log a_i is indicated as a black line.

	KH_2PO_4	NaOH	LiCl	NaCl	$MgCl_2$	$CaCl_2$	KCl	HCl
a_{i0} (M/L)	2.10^{-5}	3.10^{-4}	3.10^{-4}	5.10^{-4}	5.10^{-4}	5.10^{-4}	10^{-3}	10^{-3}
A_i (mV)	67	90	59	90	160 (140*)	160 (140*)	59	59
Cation	K^+	Na^+	Li^+	Na^+	Mg^{2+}	Ca^{2+}	K^+	H^+
Anion	$H_2PO_4^-$	OH^-	Cl^-	Cl^-	Cl^-	Cl^-	Cl^-	Cl^-
Charge of Cation	1	1	1	1	2	2	1	1
Effective Cationic radius (pm)	138	102	76	102	72	100	138	
Hydrated Cationic radius (pm)	330	276	380	360	425	410	330	

Table 4.1 Table summarizes all the extracted values of Ai, ai0, counter ions, action charge, the effective cationic radius and the hydrated cationic radius of salts studied. *slope value if fitted as function of concentration.

a_{i0} is also plotted as a function of cation charge, cation radius and hydrated cation radius shown in Figure 4.4a, 4.4b and 4.4c respectively . No clear tendency is observed in these curves. However, because a_{i0} for KH_2PO_4 is significantly smaller than for KCl (same K^+ ion), the anion may play a role in the value of a_{i0}, as discussed above.

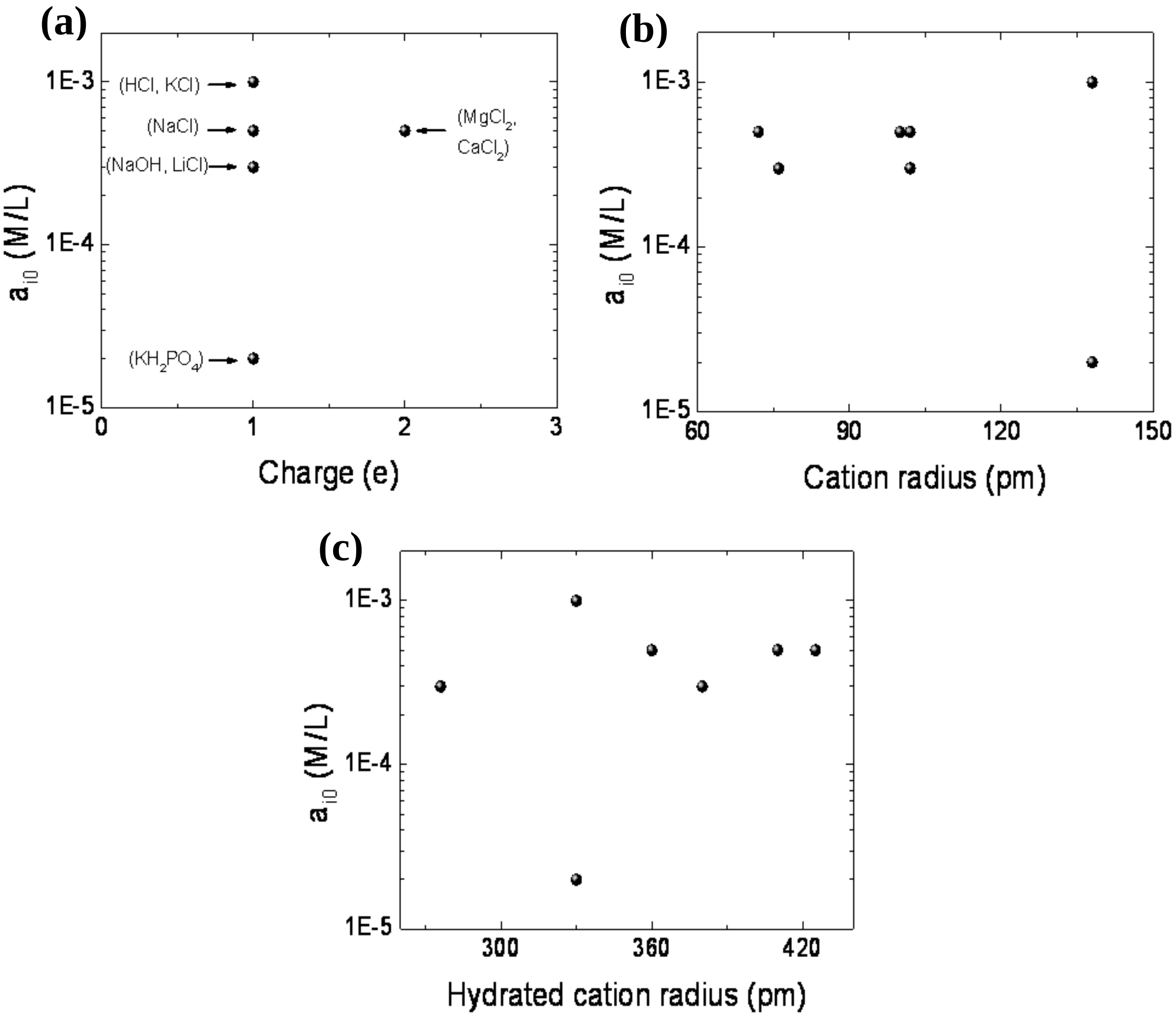

Figure 4.4 (a) Datas of a_{i0} extracted from Figure 4.3a are plotted as a function of cations charge **(b)** as a function of cations radius **(c)** as a function of hydrated cations radius.

4.1.2. Hypothesis of overcharging effect

The concept of overcharging [5, 6] or charge reversal in salty environment would take place at high electrolyte concentration and surface charge densities. The counter ion concentration next to the surface can become so large that the surface charge is overcompensated and the overcharging occurs. It is typically observed for biomolecules charge screening with multivalent ions. Interestingly, a molecular dynamics simulation of equilibrium distribution of ions around peptides has shown that the two peaks corresponding to contact ion pairing and solvent-separated ion pairs are more pronounced for Na^+ than for K^+ and in general for multivalent than monovalent ions [6]. This conclusion is in phase with our observation of higher super-Nernstian slopes for Na^+ than for K^+ and even higher for multivalent cations.

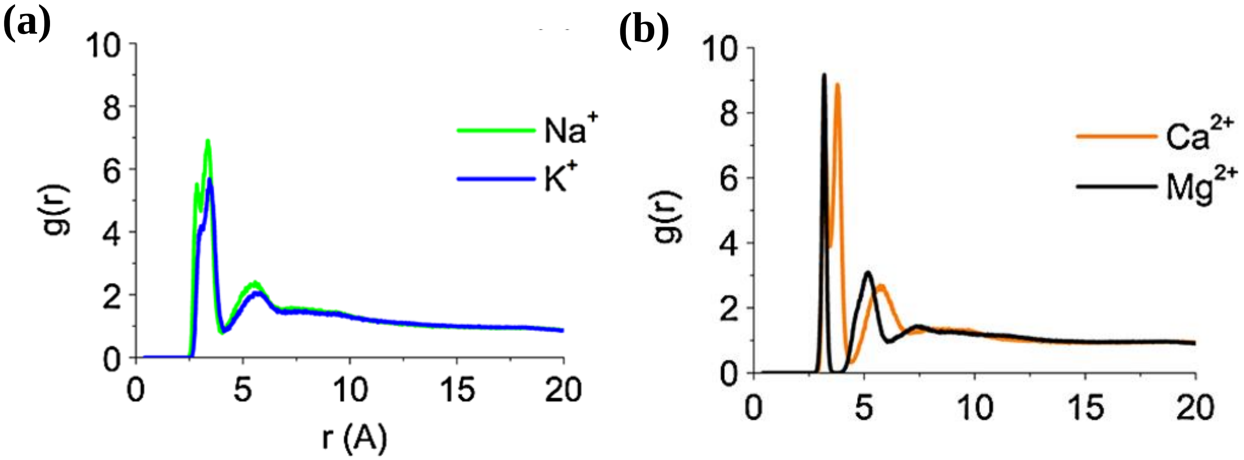

Figure 4.5 Figures reprinted from reference [6] **(a)** Radial distribution functions of Na^+ and K^+ peaks corresponds to contact ion pairing between the carboxylic groups and the metal cations and solvent-separated ion pairs **(b)** for divalent ions of Ca^{2+} and Mg^{2+}.

4.1.3. Ψ_0 response to two species coexistence of Na^+ and H^+ or Na^+ and K^+

Eq 4.1 seems to be valid when two species coexist in solution, for example by modifying both concentrations of Na^+ and H^+ or Na^+ and K^+ (see Figures 4.6a and 4.6b). This experiment also stress the weak contribution of the double layer capacitance in a_{i0} that remains identical for $[K^+] = 10^{-6}$ or 10^{-2} M [7]. Eq 4.1 looks similar to the Nikolsky - Eisenman equation (ion-exchange theory: Eq 4.2) usually used to determine the selectivity of an ion-selective electrode to interfering ions, except that the *log* is inside the sum operator.

$$\Psi_0 = constant + \frac{A_i}{z_i}.\log\left(a_i + \sum_j k_{ij} a_j^{\frac{z_i}{z_j}}\right) \qquad \text{Eq (4.2)}$$

k_{ij} is the selectivity coefficient. Eq 4.1, which generally stood the test of time, is a semi-empirical law based on an ion-exchange reaction at the surface, an approach not so far from the SBM in the sense that SiO^- interface charged sites (for silica) are indirectly involved in the reaction [8]. Therefore, it is not surprising that Eq 4.2 can't be used to fit our results.

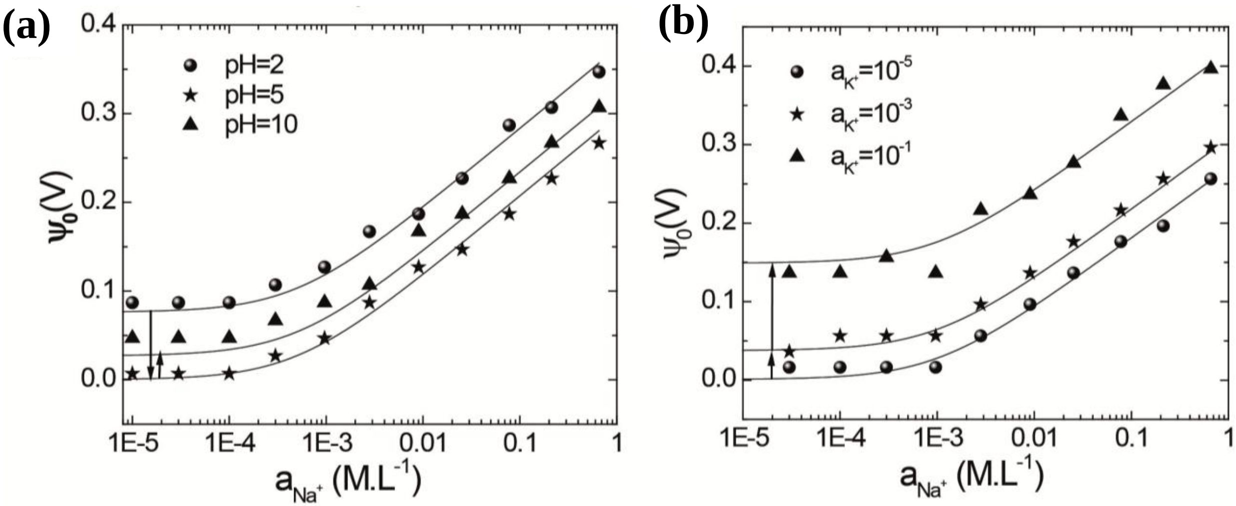

Figure 4.6 (a) Ψ_0 is plotted as a function of Na^+ activity for 3 different pHs (2, 5 and 10) to verify equation Eq 4.1 Fitting parameters are A_{Na+}=0.09 V/log(a_{Na+}), A_{H+}=0.059 V/pH, a_{NaCl0}=5x10^{-4}M/L, a_{HCl0}=5.3x10^{-4}M/L, **(b)** Ψ_0 is plotted as a function of Na^+ activity for 3 different KCl concentrations (10^{-5} M, 10^{-4} M and 10^{-2}M). Fitting parameters are A_{Na+}=0.09 V/log(a_{Na+}), A_{K+}=0.059 V/pH, a_{NaCl0}=10^{-3}M/L, a_{KCl0}=3x10^{-4}M/L.

4.2. Concept of ion selectivity without selective coating membrane on 0D ISFETs

4.2.1. Proposing Eq 4.3 for cation selectivity

The difference between Eq 4.1 and Eq 4.2 suggests two different ways of reaching selectivity. With Eq 4.2, selectivity is coming from specially designed ion-selective membranes [9], whereas with Eq 4.1, selectivity can be attained by measuring the variation of surface potential $\Delta\Psi_0$ after taking a reference and adding spikes of ions of interest in an unknown solution. It appears clearly in Eq 4.3 when taking an example with typical cations found in blood (Na^+, K^+, Mg^{2+} and Ca^{2+} with unknown activities $a_{Na\_unknown}$, $a_{K\_unknown}$, $a_{Mg\_unknown}$, $a_{Ca\_unknown}$, respectively), and rewriting Eq 4.1 as Eq 4.3. $\Psi_0(0)$ is the reference potential (bare solution). If we suppose that Mg^{2+} is the ion of interest, a_{Mg} is the concentration of Mg^{2+} added in solution from $MgCl_2$ salt, $a_{iunknown}>>a_{i0}$ for all the four cations and A_i = A for simplicity:

$$\begin{aligned}\Delta\Psi_0(a_{Mg})&=\Psi_0(a_{Mg})-\Psi_0(0)= \\ &A\,(\cancel{\log[a_{Na\_unknown}]}+\cancel{\log[a_{K\_unknown}]}+\log[a_{Mg}+a_{Mg\_unknown}]+\cancel{\log[a_{Ca\_unknown}]}) \\ &-A\,(\cancel{\log[a_{Na\_unknown}]}+\cancel{\log[a_{K\_unknown}]}+\log[a_{Mg\_unknown}]+\cancel{\log[a_{Ca\_unknown}]}) \\ &=A(\log[a_{Mg}+a_{Mg\_unknown}]-\log[a_{Mg\_unknown}])\end{aligned} \qquad \text{Eq (4.3)}$$

All constant cations are suppressed in this equation, whatever their concentration, thanks to the reference $\Psi_0(0)$. In other words, although the device is sensitive to all ions, the variation of Ψ_0 is only sensitive to the ion with tuned concentration. Eq 4.3 can be generalized as Eq 4.4:

$$\Delta\psi_0(a_i)=\psi_0(a_i)-\psi_0(0)=\frac{A_i}{z_i}\left(\log[a_i+a_{iunknown}]-\log[a_{iunknown}]\right) \qquad \text{Eq (4.4)}$$

$a_{iunknown}$ is the unknown activity of ion *i* in the unknown solution. In Eq 4.4, we supposed $a_{iunknown} >> a_{i0}$.

4.2.2. Blood ionogram with 0D ISFETs

4.2.2.1. Spike technique proposed based on Eq 4.4 for cation selectivity

To validate Eqs 4.1 and 4.4, but also because of the potential application in the biomedical field, we used fetal bovine serum (FBS) from blood (life technologies©) as a complex solution with many ions. The protocol is shown in Figure 4.7a: raw FBS is considered first to get $\Psi_0(0)$ as a reference potential. While increasing the concentration of the ion of interest, we reach the threshold $\Delta\Psi_0 > 0$ when $a_i \sim a_{iunknown}$. For a quantitative extraction of $a_{iunknown}$, it is better to get a fit of $\Delta\Psi_0\,(a_i)$ over a large range of a_i using Eq 4.3. The minimum ion concentration a_{i0} that can be detected with this technique, extracted from DI water, is below the window of ions concentration for blood or serum ionogram shown in Figure 4.7b.

In serum, Na^+ is the dominant cation (~0.1 M/L). Using our protocol and Eq 4.4, the concentration of minority cations should be detected, for example Mg^{2+} ($a_{Mg2+} \sim 10^{-3}$ M in FBS) whereas with Eq 4.2, only the majority ion would be detected (see Figure 4.7c) unless resorting to a specific Mg^{2+} selective membrane. For these measurements, we used an "on chip" Pt electrode instead of the Ag/AgCl electrode (we didn't notice relevant differences between both electrodes) to demonstrate an ionogram lab-on-chip with ultimate integration. The optical image of LoC with integrated platinum electrodes used for blood ionogram study is shown in Figure 4.7d and Figure 4.7e shows the zoomed-in picture near sensor region.

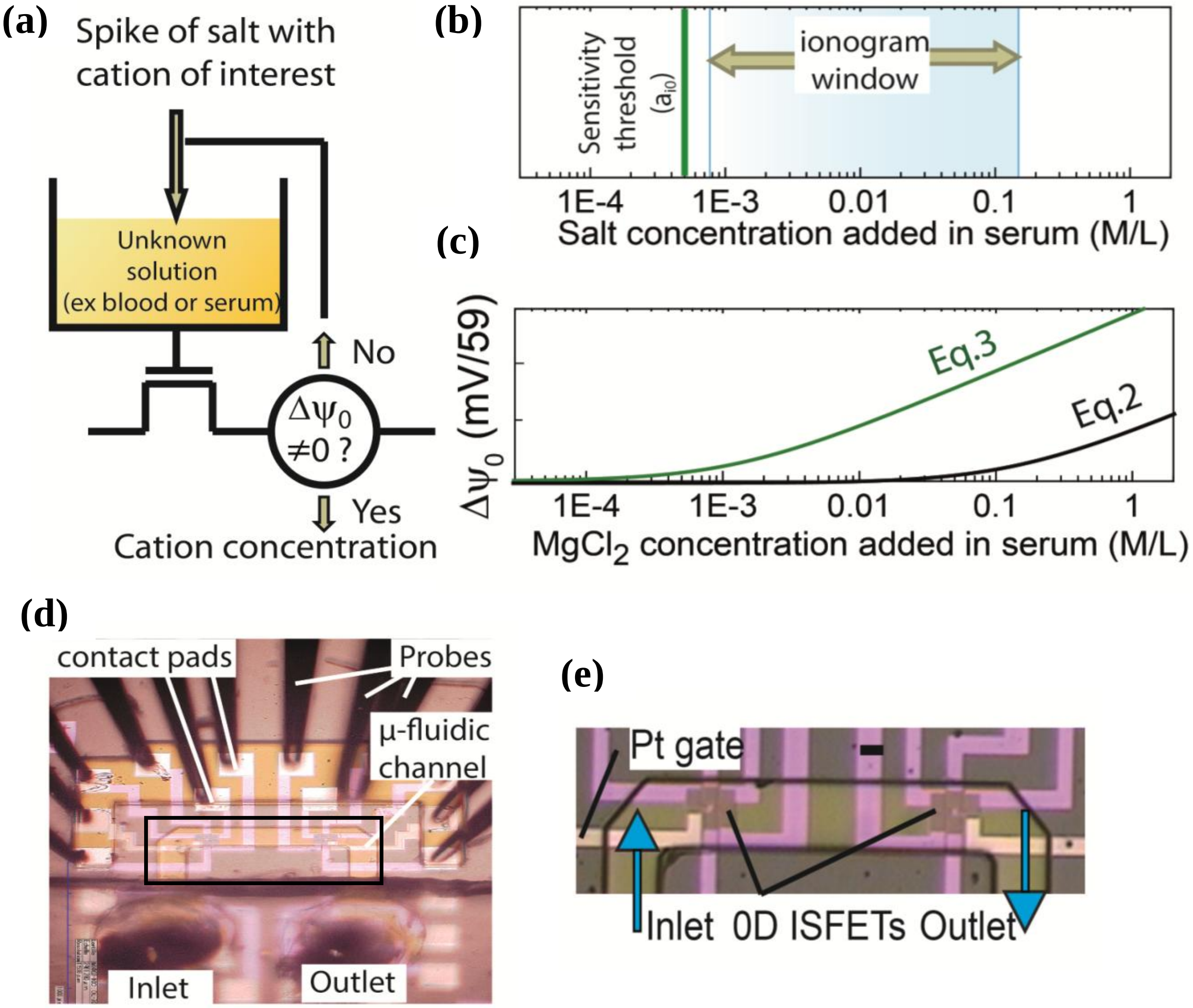

Figure 4.7 (**a**) Schematic representation of a new technique based on Eq 4.3 to extract selectively of a cation concentration without selective coating layer. For example, to extract the concentration of Mg^{2+} in an unknown solution, we add $MgCl_2$ salts in the unknown solution until reaching a threshold in Ψ_0 (spike technique). Best quantitative results are reached by considering a large range of ion concentrations and fitting with Eq 4.3 **(b)** Sensitivity of this device is determined by a_{i0} extracted from cation response in DI water (Eq 4.1). It is good enough for ionogram application **(c)** Example of difference between Eq 4.3 and Eq 4.2 for a minority ion in serum such as Mg^{2+}. With Eq 4.2 with $\kappa_i = 1$ for all ions, only the majority ions (Na^+) would be detected in blood serum. **(d)** Optical image of the lab-on-chip used for this blood ionogram. Scale bar is 50 µm. It includes electrical contact pads, four identical 0D nanotransistor

biosensors, two Pt gates and a 200 µm-large microfluidic channel with inlets / outlets for Pt tubes. **(e)** Zoomed image on the sensor zone (black square area on figure d).

4.2.2.1. Detection of cations in serum using LoCs blood ionogram

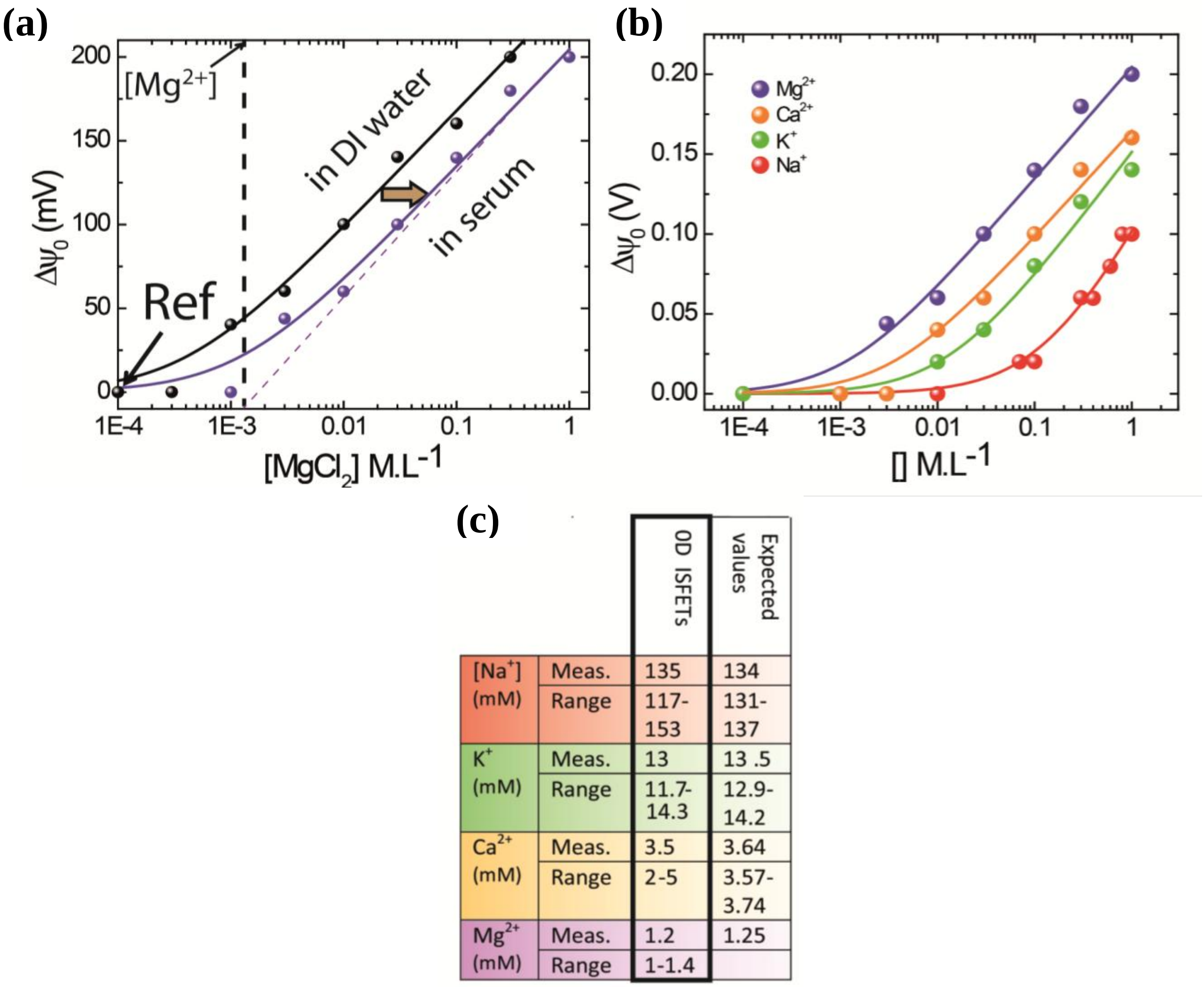

		0D ISFETs	Expected values
[Na⁺] (mM)	Meas.	135	134
	Range	117-153	131-137
K⁺ (mM)	Meas.	13	13 .5
	Range	11.7-14.3	12.9-14.2
Ca²⁺ (mM)	Meas.	3.5	3.64
	Range	2-5	3.57-3.74
Mg²⁺ (mM)	Meas.	1.2	1.25
	Range	1-1.4	

Figure 4.8 (a) $\Delta\Psi_0$-[$MgCl_2$] is plotted for DI water and FBS. Sensitivity is enough to detect [Mg^{2+}] in FBS (shift to higher [$MgCl_2$]). Good fits are obtained with Eq 4.3. **(b)** $\Delta\Psi_0$-[ ], with [ ] corresponding to $MgCl_2$, $CaCl_2$, KCl and NaCl concentrations, are fitted with Eq 4.3 **(c)** Extracted cations concentrations from fits of (b) and error bars are compared with values provided by life technologies, except for [Mg^{2+}] (not provided by life technologies) that was analyzed with IDEXX catalyst Dx biochemical analyzer.

Figure 4.8a shows Mg^{2+} detection in serum and DI water. Mg^{2+} plays an important role in many enzymatic reactions, has an anti-tetany effect, and its level is important in the diagnosis of gastrointestinal disorders. We preferred to show concentrations instead of activities for simplicity since both representations give same unknown ion concentrations. Fits using Eq 4.3 in Figure 4.8a provided [Mg^{2+}] = 1.2 mM/L, in quantitative agreement with the 1.25 mM/L (30 mg/L) estimated from the Idexx Catalyst Dx biochemical analyser.

Similarly, this experiment has been extended to identify typical cations measured for biomedical diagnosis; Na^+ (related to cardiac, renal or hepatic insufficiency), K^+ (cardiac arrhythmia, certain cancer treatments) and Ca^{2+} (carence in Vitamin D, thyroid cancer, renal insufficiency) and the similar fits with Eq 4.3 of which is shown in Figure 4.8b. Extracted cation concentrations from fits is shown in Figure 4.8c, are in the range of expectations provided by Life technology. The error bar related to the standard deviation in estimated concentrations from fits is larger in this proof of principle (~15% in average) than actual commercial machines (~1.5%). Table 4.2 is a detailed comparison of relevant parameters with commercial machines.

Name of the Machine	Operation method / cost	Sample size	Machine Dimension & weight	Reagents	Precision	Analyzing time/test	Durability
SOCIMED SERIE ISE*	ISE 3750 euros	150 µL	39cm W 44.5cm H 34cm D 22 lbs.	Na^+ K^+ Cl^- Li^+ Ca^{2+}	< 1.0% < 1.0% < 1.0% < 3.0% < 2.0%	60sec	5 years Max. For Ca^{2+} : 6months max
FUJI DRI-CHEM NX500**	Potentiometric /Colorimetric 8143 euros	50 µL/ 10 µL	47cm W 42cm H 36cm D 55.1 lbs.	Na^+ K^+ Cl^- Ca^{2+} Mg^{2+}	< 1.5%	60sec 300sec 120sec	Disposable film electrode/ analytical film
IDEXX Catalyst Dx®***	Dry slide technology 19900 euros	150 µL	35.56cm W 43.82cm H 41.28cm D 50 lbs.	Na^+ K^+ Cl^- Ca^{2+} Mg^{2+}	< 1.5%	8min	Disposables
OD ISFET****	Spike technique 10euro/chip	35 mL/ each ion	0.15cm L 0.15cm W /each chip	Na^+ K^+ Ca^{2+} Mg^{2+}	< 15%	42min/ each ion	Reusable

Table 4.2 Detailed comparison of relevant parameters of commercial machines with our 0D ISFET. *Use separate electrodes to detect each specific ion, not able to detect Mg^{2+}, use calibrants disposable solution pack ** Use Potentiometric method to detect Na^+, K^+ and Cl^-,

Colorimetric method to detect Mg^{2+} and Ca^{2+} *** Uses unique layering system to filter the impurities ****Detect no anions; mentioned dimensions and cost exclude power supply, prober, semiconductor analyzer, syringe holder and dilution is done separately; the process cost for a 4inch wafer is ~7200euro with 720 chips/wafer.

When compared to commercial machines, actual 0D ISFETs characteristics have several weaknesses: typically low precision, large volume of serum, but also clear potential strengths: low cost, small dimensions and durability. Below we discuss each of these parameters as perspectives of improvement for 0D ISFETs.

4.2.3. Perspectives of improvements for 0D ISFETs

4.2.3.1 Costs

Although the chip itself is extremely cheap, the environment is actually expensive (syringe holder: ~2500 euros, semiconductor analyser: ~30000 euros, high precision balance~ 3000 euros and operator time for dilution, measurements and treatment of datas). This could be drastically reduced using “on-chip” dilution systems [10, 11], dedicated power-supply / measurement and pumps [12]. Cost could be clearly the strength of this equipment. To date, because of high price, such clinical chemical analysis is mainly performed in dedicated laboratories.

4.2.3.2 Volume of serum

The volume of serum used for this demonstration is actually orders of magnitude larger than for commercial machines. One cannot envision taking 120 mL of blood to evaluate four ions concentration. Because the technique proposed here requires several measurements at different ionic strengths, it is naturally consuming a larger volume of serum when compared to other techniques. But on the other hand, the sensor itself is extremely small (can operated with pL volume of liquid as discussed in Chapter2). With a commercial dilution machines that dispense volumes from 100 nL [13], we could expect performing our measurements with only tens of µL of serum, as for commercial equipments. Also “on-chip” dilution can be done [10, 11] which may further reduce the volume of serum needed. As a consequence, it should be possible to use a single droplet of blood for doing such measurement with 0D ISFETs.

4.2.3.3 Equipment dimensions

Actual system dimension for the complete setup is in the range of commercial equipments mentioned above because semiconductor analyzer has typical dimensions of a desk computer. However, with "on-chip" integrations mentioned above, one could imagine a 1 cm x 1cm x 5mm total equipment dimensions, keeping the 1.5 mm x 1.5 mm of silicon area for costs optimization. Blood-serum separation [14], pumping [12] and dilution [10, 11] would occupy most of the area (~1 cm²).

4.2.3.4 Precision

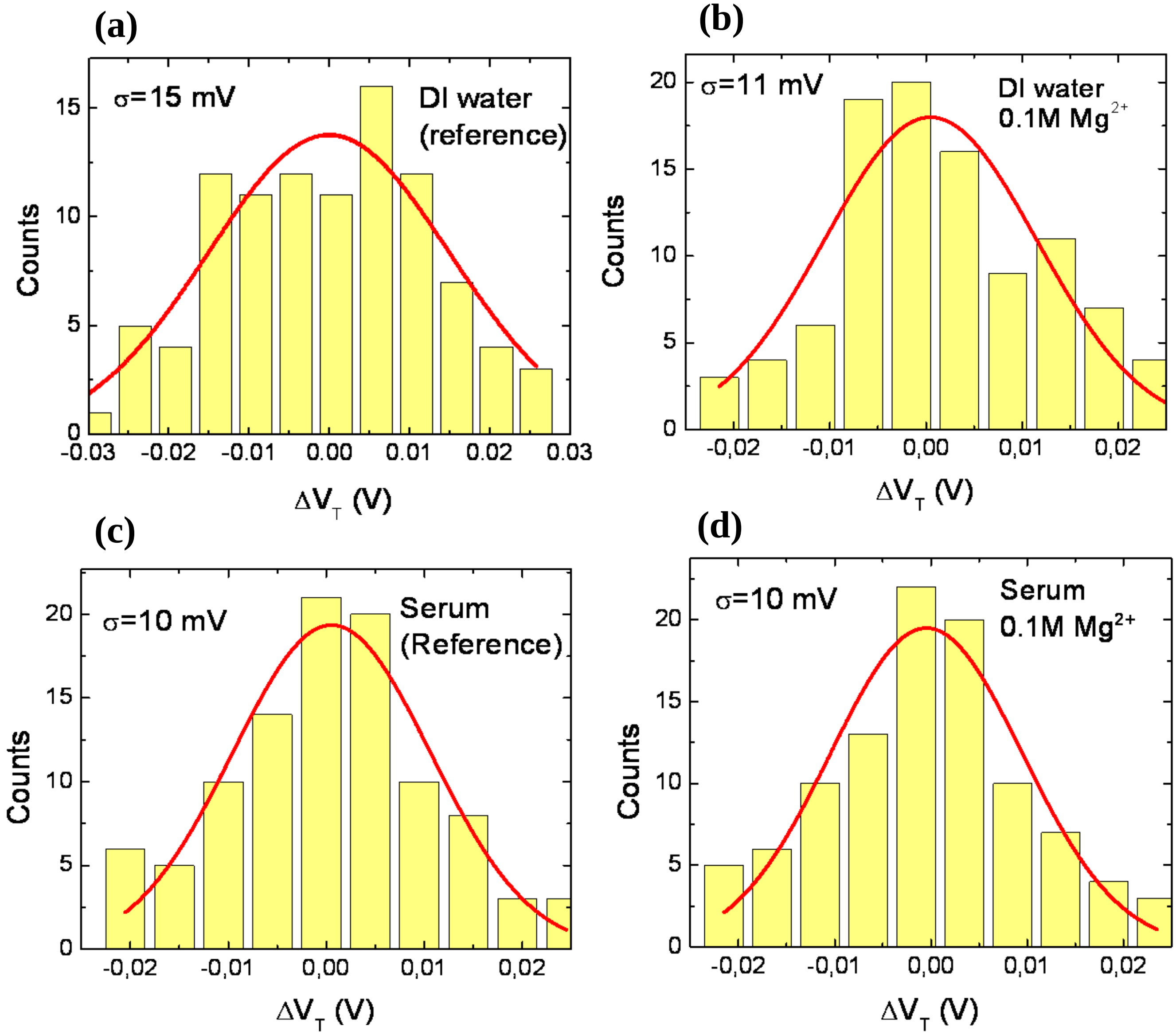

Figure 4.9 (a) Experimental histogram of threshold voltage variation from 100 measurements with the same device: liquid = DI water) **(b)** liquid = DI water + 0.1M $MgCl_2$ (c) liquid=FBS (d) liquid = FBS + 0.1M $MgCl_2$

Actual precision ~15 % is not acceptable for commercial application. To improve it, we propose an averaging filter. Figure 4.9 shows the fluctuation of threshold voltage ΔV_T (or Ψ_0) for 100 measurements performed on the same device. Before each measurement, liquid is moved for few seconds. A ~10 mV threshold voltage Standard deviation was found for DI water with 0.1 M $MgCl_2$ (Figure 4.8b) or serum (Figure 4.8c) or serum with 0.1 M $MgCl_2$ (Figure 4.8d). A larger standard deviation (~15 mV) was found for DI water (Figure 4.8a).

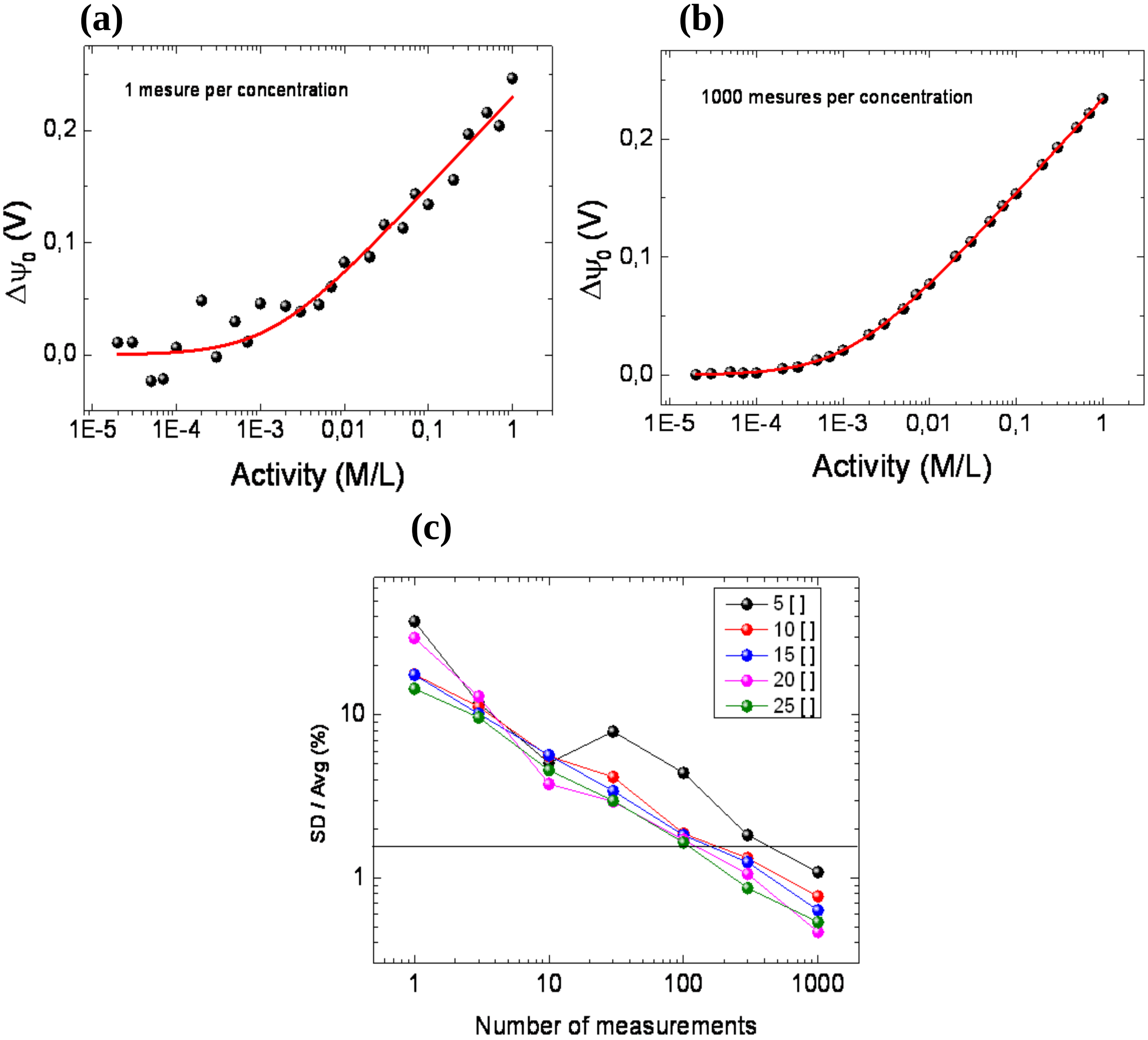

Figure 4.10 **(a)** simulated $\Delta\Psi_0$ curve as a function of Mg^{2+} concentration based on the Gaussian distribution with a standard deviation in Ψ_0 of 20 mV. Each point is generated randomly **(b)** Simulated $\Delta\Psi_0$ curve as a function of Mg^{2+} concentration based on the Gaussian distribution with

a standard deviation in Ψ_0 of 20 mV. Each point is the average from 1000 measures generated randomly **(c)** Simulated standard deviation to the concentration expected (normalized in %) as a function of the number of measurements per concentration and the number of concentrations measured. The SD expected for commercial application (1.5%), is represented by a black line.

Considering a Gaussian distribution of Ψ_0 with a standard deviation of 20 mV (x2 when compared to experimental results in serum to get a margin) and Eq 4.4, we simulated the impact of an average filter in the standard deviation to estimated concentration. Figure 4.10a shows an example of randomly generated curve for 1 measure per concentration and Figure 4.10b for 1000 measures per concentration. Error to the ideal fit is drastically reduced. Figure 4.10c shows that the standard deviation in estimated concentration should be reduced from ~20% to ~1% by increasing the number of measurements from 1 to few hundreds. It also shows that it is not necessary to measure more than 10 different concentrations (as was done in that study), if an average filter is used.

4.2.3.5 Measurement time

Times to perform measurements for extraction of one ion concentration was more than ten times longer in our study when compared to commercial machines. It was clearly not our objective. We preferred to get a nice set of datas with slow I_d-V_{lg} measurements starting from pA current with hundreds of points per curve. However, the reduction of standard deviation with an average technique inevitably multiplies the measurement time by the number of measurements. Solutions may come from time-dependent measurements at a fixed drain current and direct measurement of the shift in gate voltage. Another approach could be multiplexing since it is possible to integrate many devices on a chip (even along a concentration gradient) and device to device dispersion is relatively small which is shown in Figure 4.11 and 4.12.

4.2.3.6. Discussion

Gaussian dispersion from 100 measurements on a single device (Figures 4.9) suggests that an average filter should allow drastic reduction in the standard deviation below 1.5% with 200 measurements per concentration. Statistics on several devices can also be used (Figures 4.11). An actual limitation is the manual dilutions, with salt weight down to 200 µg to reduce to ~5 mL the volume of serum at low ionic strength.

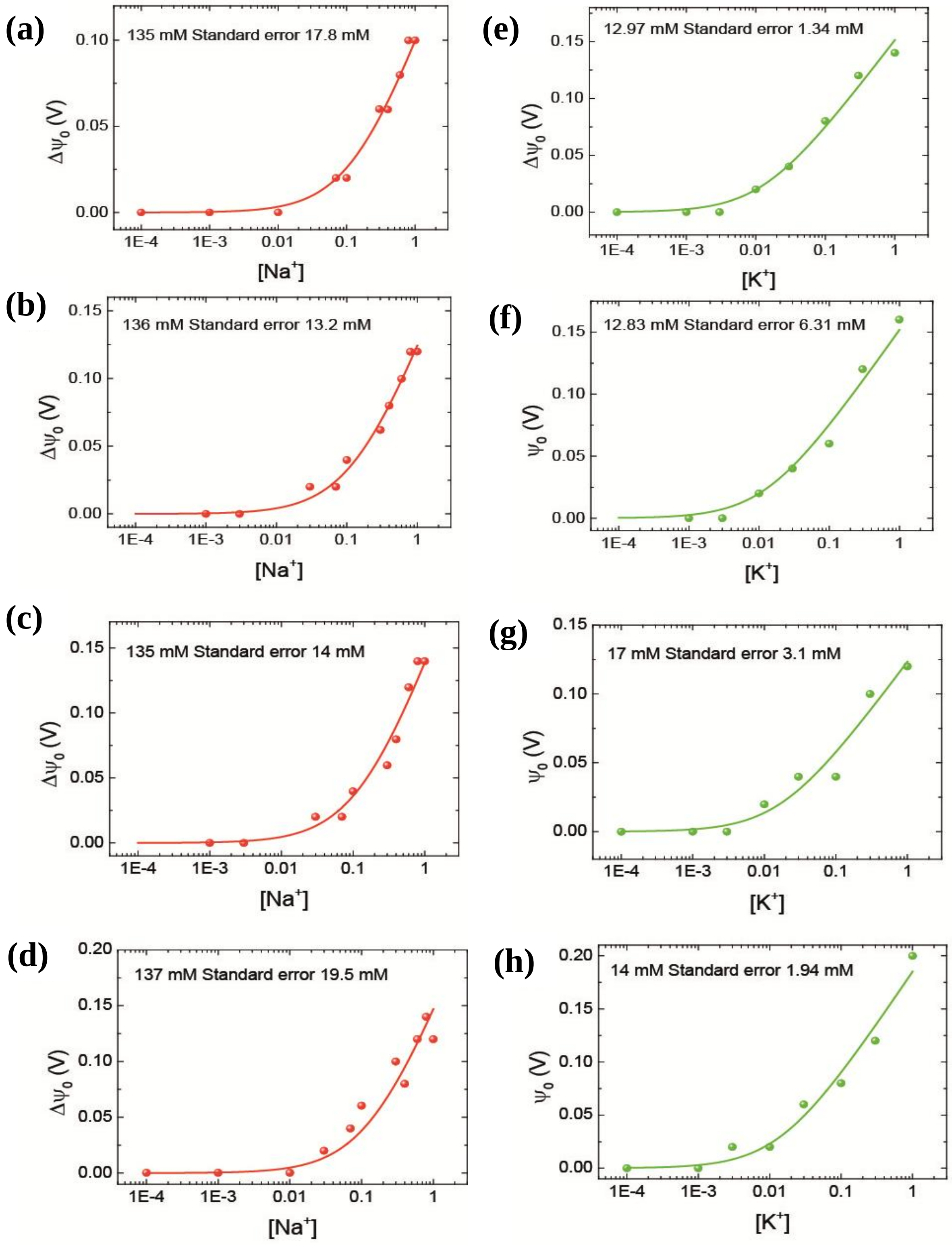

Figure 4.11 (a) S13a $\Delta\Psi_0$-[ ], with ai corresponding to NaCl **(a-d)** and KCl concentrations **(e-h)**, are fitted with Eq 4.3 for four devices. Estimated concentrations and standard errors are indicated in each figure.

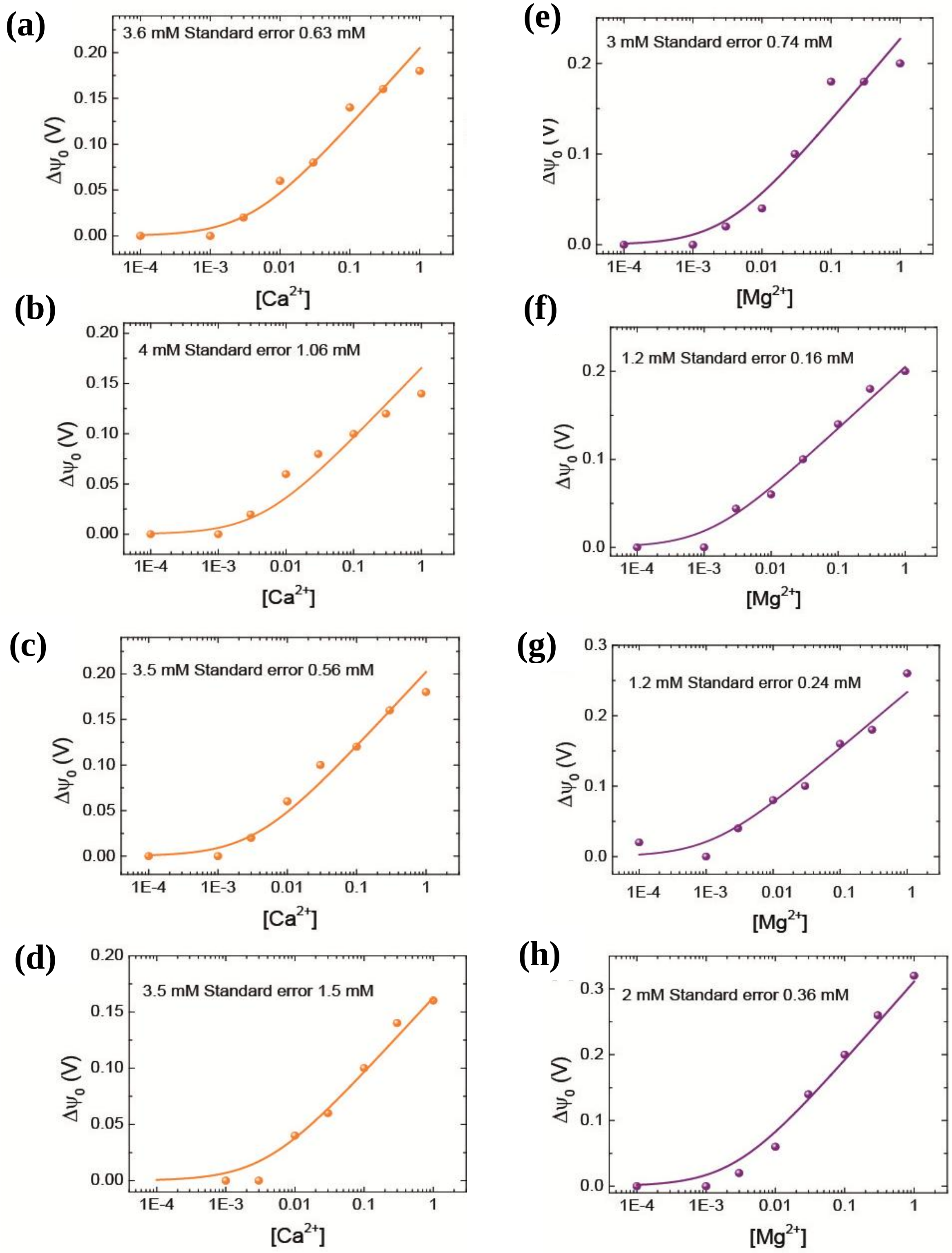

Figure 4.12 $\Delta\Psi_0$-[ ], with a_i corresponding to $CaCl_2$ **(a-d)** and $MgCl_2$ concentrations **(e-h)**, are fitted with Eq 4.3 for four devices. Estimated concentrations and standard errors are indicated in each figure.

Both automated precise dilution of salts in serum with nL range volumes [10] and blood-serum separation [14] can now be achieved “on-chip”, which promises an ultra-scaled and cheap ionogram chip with this technology when compared to the extremely large and expensive commercial machine used here to evaluate [Mg^{2+}]. The PDMS-based lab-on chip proposed here (1.5 mm x 1.5 mm with tubes and electrical contacts) is close to the ultimate integration that can be achieved with such labs-on-chip as we discussed in Chapter 2. It is therefore already optimized for costs thanks to the small silicon area and the simple process without specific coating layer.

Nowadays, such small devices can be fabricated with mass fabrication Complementary Metal-Oxide-Semiconductor (CMOS) techniques with optical lithography [15]. We noticed that this reusable sensor remains operational for months of measurements (time related to our study) and seems not to be affected by biofouling, a usual sensors drawback when working with blood or serum (discussed briefly in the below section). It is probably due to the extremely small device dimensions or to the repulsion of negatively charged proteins during measurement. With this device, there is actually no clear limitation to envision a cheap ionogram diagnosis at home from a single blood droplet. Also diagnosis ability may be extended to enzymes in the future.

4.3 Biofouling on 0D ISFETs

Adsorption of proteins on solid surfaces and their interaction are major concerns in a number of fields, such as biology, medicine, biotechnology and food processing, and sometimes play an important role in system’s performance [16]. For ISEs, it has been claimed that electrode fouling due to protein adsorption on the electrode surface is more serious in case of glass than for solvent polymeric membranes [17]. However, regular cleaning of glass electrodes, as recommended by certain manufacturers of clinical analyzers and the International Federation of Clinical Chemistry [18] can be used to solve this problem if it occurs. In our particular case: (1) We noticed that we shouldn’t let the serum for long time static in the microfluidic channel to avoid its drying (typically 1 hour) (2) Except the drying problem and viscosity of FBS, no relevant difference was observed in electrical measurements in FBS when compared to aqueous solutions.

4.3.1. Discussion on AFM measurement compared to Figures 3.13

To check if the surface itself of our transistor eventually repulses proteins, we have inserted an identical chip without microfluidic channel in serum for one night (Figure 4.13a for reference and 4.13b after FBS incubation). An increase of RMS roughness from 0.4 nm to 1 nm was observed (experiment performed on the large pad), which suggests protein adsorption on the SiO_2 surface. In addition, no significative topography or adhesion difference at the nanoconstriction (Figure 4.13c and 4.13d), which suggests that, after one night, protein adsorption also occurs at the nanoconstriction.

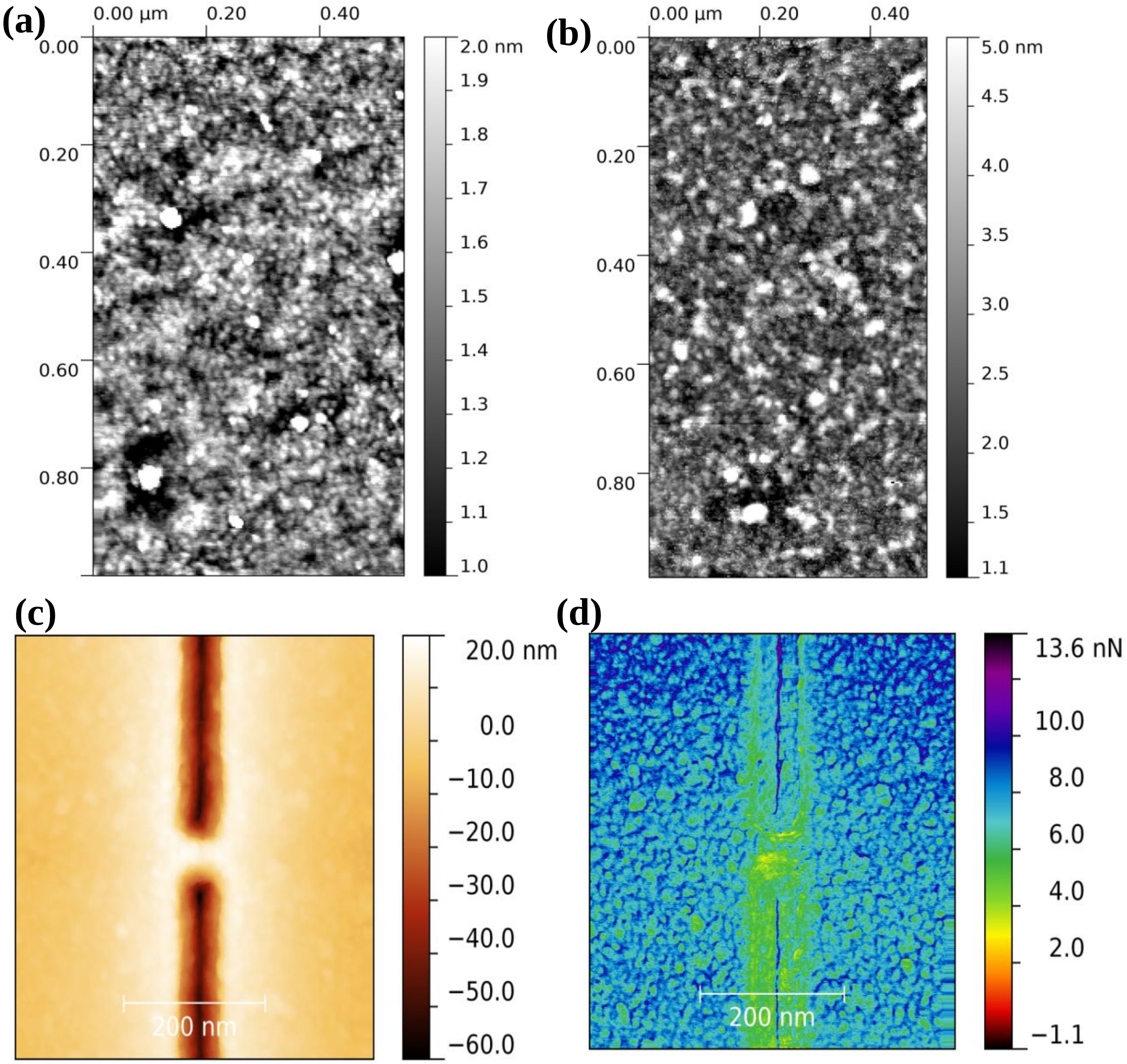

Figure 4.13 (a) 1 µm x 500 nm AFM topographic image on the large pad before incubation 1 night in FBS (rms roughness: 0.4 nm) **(b)** after incubation 1 night in FBS (rms roughness: 1 nm)

(c) AFM topographic image of the 0D ISFET and contact pads after 1 night insertion in FBS **(d)** Adhesion image related to (c)

The reason why biofouling is not considered to be an issue in our device may be related to the convection movement every 15 mn, the extremely small device dimensions or to the repulsion of negatively charged proteins during measurement (proteins are usually negatively charged and this device attracts cations at the interface). Also eventual protein adsorption would not affect the 0D ISFET gate capacitance since 35 nm of SiO_2 is thick when compared to a 1 nm-thick layer of proteins.

4.4 Discussion on the impact of the proposed equation on our understanding of oxides / ions interaction

From these experiments performed with serum that contains not only ions, but also proteins (antibody, albumin), we validated Eq 4.1 and 4.4 with a complex solution, which suggests that 0D nanotransistor biosensors are sensing the chemical potential of weakly bound cations and cation's complexes at the SiO_2 interface and not the charged surface functional groups. The proposed equations could have an impact far beyond that of 0D ISFETs.

Indeed, it was recently reported that ideal pH sensors with full Nernstian response made of Si NWs coated with Al_2O_3 or HfO_2 have sensitivity to salts that can't be explained with usual models including Nikolsky-Eisenman equation [19]. Their curves are similar to those presented in Figure 4.3a with a plateau and a Nernstian slope except that $a_{i0} \sim 20$ mM (inside the ionogram window) and Ψ_0 has a negative slope. An alternative model relying on the SBM was proposed based on surface complexation such as $MOHCl^-$, with M being Al or Hf. Unfortunately, their model can't explain our results due to the few surface functional charged sites and it shouldn't provide selectivity for complex solution with many ions. At the opposite, our Eq 4.1 (considering anions instead of cations) could also fit their results in the whole pH range except for H^+ / OH^- ions that still follow the SBM due to the large density of OH active sites in their device. XPS measurements on silica-water interface formed in NaCl solution at variable pH and ionic strength have shown that Na^+ ions are either chemically bound to SiO^- at high pH forming ion pairs (inner-sphere complexes Si-ONa) or "free" at the surface, keeping their hydration sheath fully or partly (outer-sphere complexes) [19]. The first situation may be related to the SBM and the second to Eq 4.1. As a consequence, although the pH response is specific to our 0D nanotransistor biosensors, the impact of Eq 4.1, related to the contribution of weakly bound ion's complexes on surface potential, may go far beyond the device studied here, including fields of NW biosensors, colloid particles, nanofluidics or biomolecules screening (overcharging effect).

4.5. Summary

Using 0D nanotransistor biosensors with few effective charged surface functional groups on surface, we show specific cation selectivity and more than twice Nernstian sensitivity found for Ca^{2+} and Mg^{2+} divalent ions which is probably due to overcharging effect. Also we proposed a simple semi-empirical law for the cation sensitivity of these nanoscale sensors. Using the specificity of this equation we demonstrated ion selectivity of Na^{+}, K^{+}, Mg^{2+} and Ca^{2+} in serum without need for ion-selective membranes on the nanoconstriction region of 0D nanotransistor. The selected blood ionogram with the use of single nanoscale transistor on millimeter square LoCs, was based on a new engineering concept which may find broad application in the field of biomedical diagnosis. Finally we have discussed the advantages of this new diagnosis technique and the impact of proposed equation. This study will surely find impact in the field of micro/nanotechnology, physico- and bio-chemistry, sensors engineering and biomedical diagnosis.

Bibliography

[1] Buhlmann P, Pretsch E, Bakker E (1998) Carrier-Based Ion-Selective Electrodes and Bulk Optodes. 2. Ionophores for Potentiometric and Optical Sensors. Chem. Rev. 98 (4):1593-1687.

[2] Knopfmacher O, Tarasov A, Fu W, Wipf M, Niesen B, Calame M, Schönenberger C (2010) Nernst Limit in Dual-Gated Si-Nanowire FET Sensors. Nanolett. 10 (6):2268-2274.

[3] Liu CC, Bocchicchio DB, Overmyer PA, Neuman MR (1980) A Palladium-palladium oxide miniature pH electrode. Science 207(4427):188-189.

[4] Miyake M, Chen LD, Pozzi G, Bühlmann P (2012) Ion-selective electrodes with unusual response functions: simultaneous formation of ionophore-primary ion complexes with different stoichiometries. Anal. Chem. 84(2):1104-1111.

[5] Kubickova A et al (2012) Overcharging in biological systems: reversal of electrophoretic mobility of aqueous polyaspartate by multivalent cations. Phys. Rev. Lett. 108 (18):186101.

[6] Lenz O, Holm C (2008) Simulation of charge reversal in salty environments: Giant overcharging? Eur. Phys. J. E 26:191-195.

[7] Nikolsky BP Zh Fiz Khim 10, 495 (1937)

[8] Scholz F et al (2011) Nikolsky's ion exchange theory versus Baucke's dissociation mechanism of the glass electrode. J. Solid State Electrochem. 15:67-68.

[9] Schasfoort RBM, Schlautmann S, Hendrikse J, van den Berg A (1999) Field-Effect Flow Control for Microfabricated Fluidic Networks Science 286:942-945.

[10] Kim C, Lee K, Kim JH, Shin KS, Lee KJ, Kim TS, Kang JY (2008) A serial dilution microfluidic device using a ladder network generating logarithmic or linear concentrations Lab Chip 8(3):473-479.

[11] Lee K, Kim C, Kim Y, Jung K, Ahn B, Kang JY, Oh KW (2010) 2-layer based microfluidic concentration generator by hybrid serial and volumetric dilutions Biomed Microdevices 12(2):297-309.

[12] Yobas L, Tang KC, Yonga SE, Onga EKZ (2008) A disposable planar peristaltic pump for lab-on-a-chip Lab Chip **8**:660-662.

[13] Microlab 600 Dispenser and diluters.
http://www.hamiltoncompany.com/products/laboratory-products/laboratory-instruments/microlab-600-diluter-dispenser/microlab-600-configurations

[14] Chen J et al (2014) Blood plasma separation microfluidic chip with gradual filtration. Microelec. Eng. 128:36-41.

[15] Voisin B et al (2014) Few-Electron Edge-State Quantum Dots in a Silicon Nanowire Field-Effect Transistor. Nano Lett. 14 (4):2094–2098.

[16] Nakanishi et al (2001) On the adsorption of proteins on Solid Surfaces, a common but very complicated phenomenon. J. Biosci. Bioeng. 91(3):233-244.

[17] Simon W, Ammann D, Anker P, Oesch U, Band DM (1984) Ion-selective electrodes and their clinical application in the continuous ion monitoring. Ann N Y Acad Sci. 428:279-285.

[18] Mass AHJ, Weisberg HF, Burnett RW, Muller-Plathe O, Wimberley P, Zijlstra WG (1987) Approved IFCC methods. Reference method (1986) for pH measurement in blood. J Clin Chem Clin Biochem 25:281-289.

[19] Shchukarev A, Rosenqvist J, Sjoberg S (2004) XPS study of the silica-water interface. J. Electron Spectroscopy 137:171-176.

5

Conclusions and Perspectives

5.1 Conclusions

In this thesis, the goal of the work done relies on four important parts.

1. The first part deals with investigation of new technique proposed for PDMS / Silicon chip alignment with sub-µm precision that uses no lubricant.
2. The second part deals with addressing the technological and physical limits for maximal integration of PDMS-based LoCs with nanotransistor biosensors. Also, we discussed the impact of such integration on sensors properties.
3. The third part deals with using 0D nanotransistor biosensors. We have shown a rupture in the universal monotonic decrease of oxide surface potential Ψ_0 with pH and presented a U-shape pH response.
4. In the fourth part, we have shown specific cation selectivity and super Nerntzian sensitivity for divalent (Mg^{2+} and Ca^{2+}) ions without need for ion selective membrane using 0D nanotransistor biosensors. The proposed model is at the origin of the new method for ion selective measurements.

In more detail,

In the first Chapter, we proposed a new alignment technique for PDMS / Silicon chip. We have shown that thin PDMS layers are of great advantage for precise alignment because the shrinkage ratio is reduced by 50% and adhesion force is larger than the weight of the PDMS layer. This has been considered for designing a dedicated tool for fast and easy alignment with high throughput. It will also enable the replacement of resist microbath with perfectly aligned PDMS microfluidic channels on silicon nanosensors. This technique can also be used for PDMS-PDMS alignment with high accuracy and reproducibility.

In the second Chapter, we have addressed the technological and physical limits for the maximal integration of PDMS-based LoCs. This integration is related to the critical distance between the microfluidic channel and the holes for the electrical contacts below which we observe leakage. For a functional device with ultimate integration, optimal values of channel width and the critical distance (sensing device to the closest electrical contact pad) have been investigated. Using 1.5 mm × 1.5 mm LoCs with 0D nanotransistor biosensors, we have successfully shown Nernstian response to Na^+ with reduced standard deviation compared to resist microbath approach and ability to operate with picoliter range volumes. We have also demonstrated the importance of scaling the electrical contacts and the microfluidic channel width for optimal frequency response up to few mega-Hertz of these nanoscale sensors. Finally, we uncovered the possibility of tuning the nanotransistor threshold voltage with microfluidic channel width which may allow these nanotransistor biosensors to operate with optimized power consumption. This work could be transposed for all LoCs that require electrical contacts close to microfluidic channel.

In the third Chapter, using 0D nanotransistor LoC biosensors, we have shown a rupture in the universal monotonic Ψ_0 - pH response with apparently few charged functional groups at the nanoconstriction region. Mainly, the surface potential $\Psi_0 > 0$ suggested that 0D ISFETs are new type of sensors only sensitive to cations of H^+ and Na^+ in the acid-base solutions due to presence of few SiO^- sites. Also we checked and demonstrated that large ISFET fabricated with identical technological process integrated on our same chip showed universal Ψ_0 - pH response and is well fitted with site-binding model. Although the possible “nanoscopic picture” of the 0D nanotransistor biosensors surface chemistry is not fully understood yet, we have evidenced from the Ψ_0 - pH response and drift measurements that there are likely only few charging sites at the maximum on top of nanotransistor.

In the fourth Chapter, we showed a potential application towards biomedical diagnostic LoC system with 0D nanotransistor biosensors. With apparently few effective charged surface functional groups on the nanoconstriction region, we have shown specific cation selectivity and more than twice Nerntzian sensitivity for Mg^{2+} and Ca^{2+} divalent ions. Also we proposed semi-empirical formula for cation sensitivity and using the specificity of this equation, we demonstrated the ion selectivity of Na^{+}, K^{+}, Mg^{2+} and Ca^{2+} in serum without need for ion selective membranes. We performed a blood ionogram with the use of single nanoscale transistor on millimeter square LoCs based on this new engineering concept which may find broad application in field of biomedical diagnosis. Also we have discussed the advantages of this new diagnosis technique. This study will surely have a impact in the field of micro/nanotechnology, physico- and bio-chemistry, sensor engineering and biomedical diagnosis.

5.2. Perspectives

5.2.1. 0D nanotransistor for biomimetic studies

The present study could have an impact beyond our expectations. An example is the study of biological systems using electrophoretic mobility. It is a widely used technique to extract the amount of positively and negatively charged amino acid residues at the surface of peptides and proteins, in direct relation with their solubility and tendency to form complexes. In particular, it was pointed out that the presence of multivalent salt ions can significantly affect the charge extracted for biomolecules, with overcharging being the extreme case of compensation [1]. Using the most simple equation of electrophoretic mobility proposed by Smoluchowski:

$$\mu_e = \varepsilon_0 \varepsilon_r \xi / \eta \qquad \text{Eq (5.1)}$$

where ε_r is the dielectric constant of the dispersion medium, ε_0 is the permittivity of free space, η is the dynamic viscosity of the dispersion medium and ξ is the zeta potential (i.e. the electrokinetic potential of the slipping plane in the double layer), and if we neglect the effect of Stern layer such that surface potential Ψ_0 represents the zeta potential at the surface, we get:

$$\mu_e = constant + \frac{\varepsilon_0 \varepsilon_r}{\eta} \sum_i \frac{A_i}{z_i} \log(a_i + a_{i0}) \qquad \text{Eq (5.2)}$$

This equation has been tested on published experimental datas for anionic liposomes [2] with reasonable agreement shown in Figure 5.1. We don't pretend that this simple equation will replace atomistic and coarse grained simulations of biological systems, for example. Our aim is to point out the potential of using such solid-state devices to mimic complex charge compensation effects in biological systems and vice-versa.

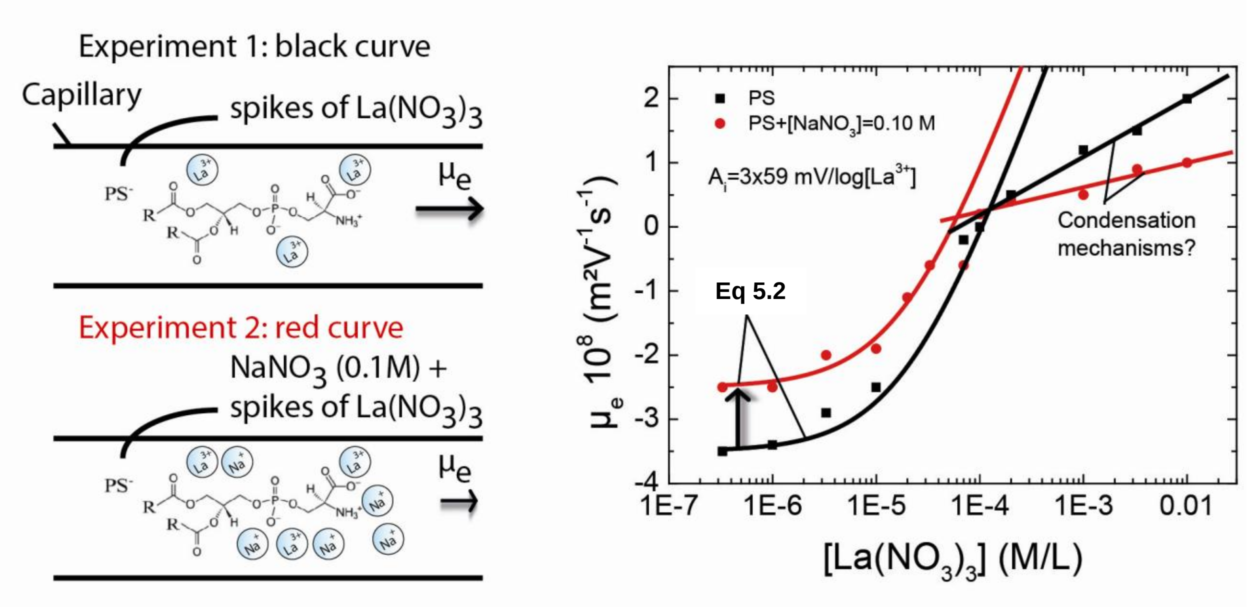

Figure 5.1 Electrophoretic mobility μe of PS- liposomes as a function of $[La(NO_3)_3]$ taken from reference [2]. Black squares corresponds to PS- (no background electrolyte), red circles to PS- with 100 mM of $NaNO_3$ as a background electrolyte. Inset: Chemical structure of the PS- lipid. In reference [2], quantitative discussion on these curves was mainly related to the concentration at which μ_e=0. Using Eq 5.2, we obtained good fits considering A_i = 3x59mV/log ($[La^{3+}]$) and $a_{i0}=2x10^{-5}$ M/L. The shift in μ_e for the black and red curves look similar to the shifts shown in Fig.3D with 0D nanotransistor biosensors. Quantitatively, it corresponds to a shift in zeta potential of ~+14 mV, a feasible value if a_{i0} for $NaNO_3$ is in the range of 10^{-4} M/L. The triple Nernstian slope for trivalent ions may be possible given that a twice Nernstian slope is found for divalent ions. This example shows the potential of biomimetics studies of biomolecules charge compensation with 0D nanotransistor biosensors and vice versa. For example, it was recently suggested that the saturation observed in this figured (fitted with a simple log dependence) may be related to some condensation mechanisms [3, 4].

5.2.2. Hydrogen Silsesquioxane (HSQ)-based Nanofluidics

In recent years with the fast evolution and growth in the field of nanotechnology, many types of nanofluidic structures have been successfully fabricated and demonstrated for use in chemical sensors and biosensors [5]. We could envision to integrate nanochannels with at least one characteristic dimension below 100nm [6, 7] on the site of detection devices (eg. 0D nanotransistors) coupled to well-developed PDMS microfluidics, thus having lower cost, higher detection sensitivity and to speed up sample delivery with nanofluidic techniques. These distinctive features give access to transport phenomenon that can only occur at the nanoscale and that has shown great potential in both bio- and energy-related fields.

Nanofabrication strategies for nanofluidic channels include optical, e-beam or nanoimprint lithography with sacrificial layers or etching. Another alternative is the use of nanoporous materials. Here, we propose a new alternative based on the direct, 3D prototyping of Hydrogen Silsesquioxane (HSQ) trans-parent walls. This approach is rapid and versatile.

Technological steps for the proposed approach are summarized in Figure 5.2a. We use HSQ (Fox 16, Dow Corning), a negative resist that can be exposed by e-beam lithography. It can be almost fully densified to SiO_2 after plasma exposure, thus providing robust, hydrophilic and transparent nanofluidic channel walls. Then, using an aligned and patterned Polydimethylsiloxane (PDMS) layer, nanofluidic channels are sealed and connection to micro-fluidic channels is established. The distance between walls has to be small enough and walls sharp enough to avoid bonding of PDMS to the bottom of the channels. On the other hand, at the opposite side of the walls, a smooth slope is required for proper PDMS/HSQ sealing. This 3D proto-typing can be achieved, thanks to the unique properties of HSQ, using different e-beam doses within a single writing step (less exposed areas appear thinner after HSQ resist development).

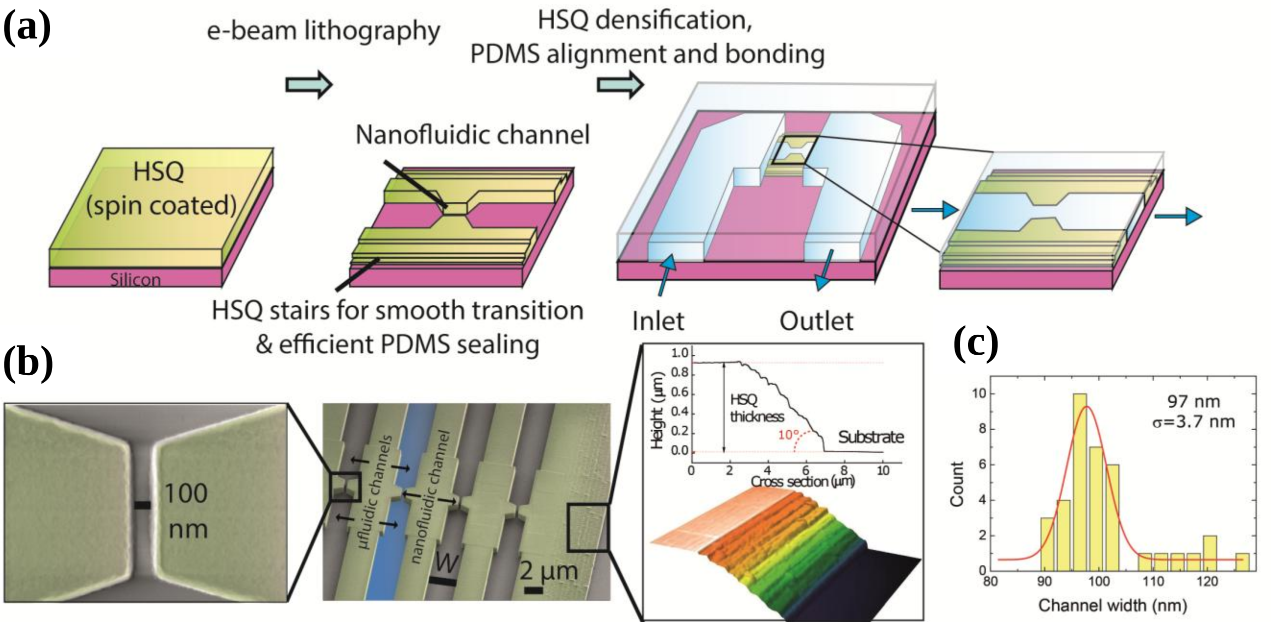

Figure 5.2 (a) Schematic view of the HSQ-based process for nanofluidics. 900 nm-thick HSQ is first spin-coated. HSQ walls and stairs are written within a unique and short e-beam lithography

step (typically 1 mn/chip). HSQ is densified by plasma O_2 and the PDMS microfluidic channel is then aligned and bonded. **(b)** Scanning Electron Microscope (SEM) top views of the HSQ nanochannels and Atomic Force Microscope image topography image of HSQ stairs with a cross section. Channel width W is 3 µm at inlets and outlets and below 100 nm at the nanoconstriction that defines the nanofluidic channel. **(c)** Histogram of nanofluidic channel width measured by SEM for 37 channels. Average width is 97 nm and standard deviation σ = 3.7 nm.

Figure 5.2b shows the fabricated HSQ structure composed of parallel large channels with constrictions (nanofluidic channels). The average roughness is 0.7 nm. A smooth slope of 10° has been obtained from ten 90 nm-thick, 500 nm-long stairs obtained from 10 different exposure doses. Figure 5.2c shows the dispersion of channel width obtained from 37 channels. The average nanofluidic channel width is 97 nm with a standard deviation of 3.7 nm. It highlights the reliability of the proposed technology. We can nevertheless observe that 15% of the channels are out of this statistics, but they all remain within an error of 25 nm above the average width.

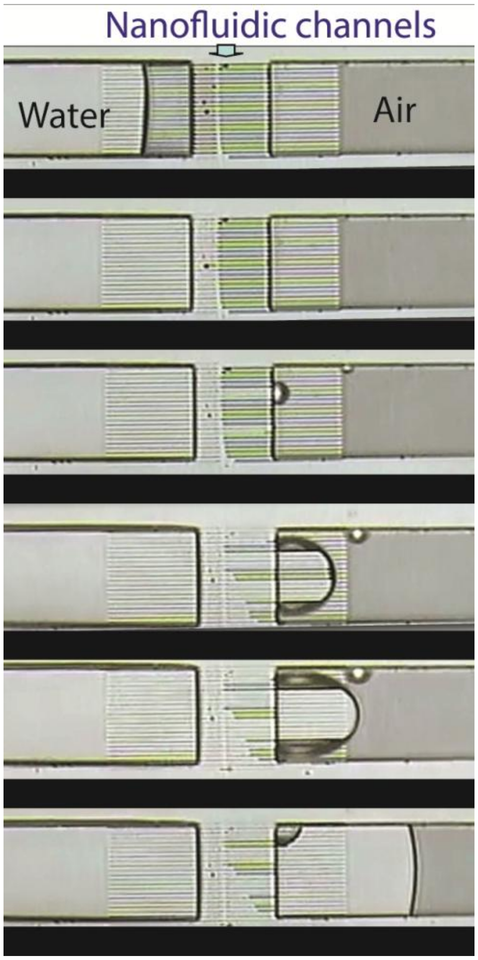

Figure 5.3 Optical microscope images of PDMS-sealed nanofluidics channels under constant pressure of 3 bars at different times.

Figure 5.3 shows optical picture of PDMS-sealed nanofluidics channels at different stages of water filling under a given pressure of 3 bars. It confirms that functional nanofluidics channels can be successfully obtained with this technology. Although dispersion in filling times (up to tens of seconds) is observed, all channels can be filled under the same pressure. We believe that the proposed technology will surely become a toolbox for versatile and reliable nanofluidics-based applications, with the unique possibility of aligning nanofluidic channels with few nanometer precision.

Bibliography

[1] Kubickova A et al (2012) Overcharging in biological systems: reversal of electrophoretic mobility of aqueous polyaspartate by multivalent cations. Phys. Rev. Lett. 108 (18):186101.

[2] Martin-Molina A et al (2010) Charge reversal in anionic liposomes: experimental demonstration and molecular origin. Phys. Rev. Lett. 104 (16):168103.

[3] [3] Zhang F et al (2008) Reentrant Condensation of Proteins in Solution Induced by Multivalent Counterions. Phys. Rev. Lett. 101 (14):148101.

[4] Zhang F et al (2010) Universality of protein reentrant condensation in solution induced by multivalent metal ions. Proteins 78(16):3450-3457.

[5] Gates B et al (2005) New Approaches to Nanofabrication: Molding, Printing, and Other Techniques. Chem. Rev. 105:1171-1196.

[6] Eijkel JCT, Berg AVD (2005) Nanofluidics: What is it and what can we expect from it?" Microfluid. Nanofluid. 1(3):249-267.

[7] Sparreboom W, Berg AVD, Eijkel JC (2009) "Principles and applications of nanofluidic transport," Nat. Nanotechnol. 4(11):713-720.

A

Appendix: Fabrication Protocols

Device Fabrication

Silicon wafer Characteristics

- Wafer: 3” Silicon
- Supplier: SILTRONIX Silicon technologies
- Orientation: (100) ±0.5°
- Type / Dopant: n-type, Phosphorous
- Resistivity: 0.001 - 0.003Ωcm
- Thickness: 355 - 405µm
- Process: Czochralski (CZ) technique

Silicon mold for PDMS Microfluidics

- ***Silicon Wafer Cleaning:***
  i. UV-Ozone for 15 min
  ii. piranha solution: H_2O_2: H_2SO_4 (1:3) for 15 min, DI (deionised) water rinsing for 1 min, Nitrogen (N_2) dry.
  iii. hydrofluoric (HF) acid 5% clean for 1.5 min, DI water rinse for 1min, N_2 dry
- ***Spin Coating***:

  i. S1818 resist, speed: 2500 rpm, acceleration: 1000 rpm, time: 12 sec, thickness ~4 µm
  ii. prebake on hot plate in contact for 1 min at 110 °C

- ***UV lithography (SUSS MicroTec) and Development:***
  i. exposure time: 12 sec, exposure gap: 10 µm, wec offset: 0, wec type: cont, exposure type: hard
  ii. MIF 319 for 50 sec, DI water rinse, N_2 dry.
- ***Reactive Ion Etching (RIE): STS surface technology systems (multiplex ICP)***
  i. SF_6 450 sccm, O_2 45 sccm, C_4F_8 100 sccm, coil power: 1000 W, pressure: 20 mT, temperature: 10 °C, time= 10min, Etching rate ~ 4 µm / min
  ii. dip in EKC 265 at 60 °C for 30 min to strip the remaining resist, followed by acetone and isopropanol (IPA) for 5 min each.

PDMS device fabrication

- ***PDMS Sol mixing***:
  i. curing agent: base ratio 1:3, mixing thoroughly for 15 min
  ii. degas in vacuum desigator / chamber for atleast 30 min to remove bubbles
- ***Spin coating of PDMS on Silicon mold:***
  i. speed: 300 rpm, acceleration: 100 rpm, time: 30 sec, thickness ~200 µm
  ii. curing in two steps 1) at 65 °C for 20 min in contact with hot plate, and 2) in convection oven at 120 °C for 1 hr.
- ***Cutting:***
  i. After cooling the PDMS layer was cut and peeled-off from the substrate. The reverse pattern of the silicon mold was transferred to the solid PDMS part.

SU-8 / Silicon hybrid mold for making holes in PDMS device

SU-8 structures on pre-defined pattern were formed on silicon mold to create holes in 200 µm thin PDMS layer as shown in Figure A1 for electrical contacts and tubing. SU-8 is a negative tone epoxy resist, sensitive to UV light and electron beam exposure. The 300 µm thick SU-8 layer was required so as to form holes in the PDMS microfluidic system. After UV lithography, the SU-8 was baked and developed, according to the protocol below. Then, the silicon mold with SU-8 structures on top were covered with a thick and fluid PDMS layer using spin coating technique (refer the protocol of PDMS device fabrication above) that was thermally cured to obtain a cross-linked and solid PDMS structures. During spin coating the residual PDMS on SU-8 structures were selectively removed by blowing with nitrogen gun to generate holes in thin

PDMS layer (J H Kang et al). After cooling, the PDMS layer was cut and peeled-off from the substrate.

- ***Fabrication of SU-8 structures***

i. UV-Ozone (5 min) and 5% HF (1.5 min) cleaning before spin coating SU-8 resist on patterned silicon mold (refer silicon mold for PDMS microfluidics above).
ii. dehydration bake at 180 °C for a 15 min.
iii. spin coating first layer of SU-8 2002 resist: *step1*- speed: 500 rpm, acceleration: 100 rpm, time: 5 sec *step2*- speed: 2000 rpm, acceleration: 100 rpm, time: 30 sec, prebake on hot plate in contact for 1 min at 65 °C and 2 min at 95 ˚C
iv. spin coating second layer of SU-8 2075 resist: *step1*- speed: 500 rpm, acceleration: 100 rpm, time: 5 sec *step2*- speed: 2000 rpm, acceleration: 300 rpm, time: 30 sec, prebake done with two levels of annealing steps 1) at 65 °C for 30 min and 2) at 95 °C for 12 hr; each temperature ramp was 1hr , thickness~300 µm
v. UV lithography - exposure time: 45 sec, exposure gap: 300 µm, alignment gap: 100 µm wec offset: 0, wec type: cont, exposure type: prox
vi. post exposure bake is done again with two levels of same annealing steps 1) at 65 °C for 30 min and 2) at 95 °C for 12 hr; each temperature ramp was 1hr
vii. developing with SU-8 developer for 12hr, IPA rinse, N_2 dry
viii. hard bake at 190°C for 1 hr, and the temperature ramp was 1hr from room temperature.

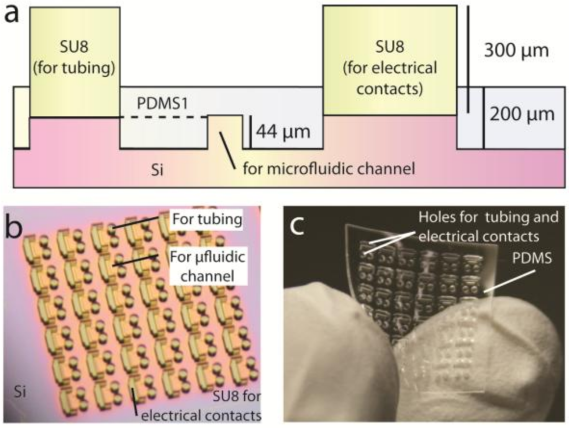

Figure A1 (a) Schematic view of mold used for PDMS1 to define the microfluidic channel (silicon) and the holes for the electrical contacts and tubings (SU-8). (b) Optical microscopy image of 1.5 mm x 1.5 mm of the mold. (c) Picture of 200 µm thick 1.4 cm x 1.4 cm PDMS1 with holes for electrical contacts and tubing.

Device fabrication 0D and nanoribbon transistors (NTT, Japan: K.Nishiguchi and A.Fujiwara)

The 0D and nanoribbon transistors were fabricated on an SOI wafer. First, a narrow constriction sandwiched between two wider (400-nm wide) channels was patterned on the 30-nm-thick top silicon layer (p-type, boron concentration of 10^{15} cm^{-3}). The length and width of the constriction channel were 30 and 40 nm, respectively. No constriction was defined for the nanoribbon transistor. The patterning was followed by thermal oxidation at 1000 °C to form a 20-nm-thick SiO_2 layer around the channel. This oxidation process reduced the size of the constriction to about 15 nm, giving a final channel dimension of 15×25 nm. Then, we implanted phosphorous ions outside the constriction, 5 µm away from it, using a resist mask to form highly doped source and drain regions. Finally, aluminium electrodes were evaporated on the source and drain regions.

For the ionogram lab-on-chip, Platinum electrodes were evaporated using electron beam evaporation (75 nm) using resist mask to form an integrated liquid gate.

Solutions preparation and information

- ***Deionized water***

  Solutions with different ion concentrations were prepared in DI water (resistivity 18 MΩ). The adsorption of carbon dioxide can change pH of aqueous solutions. Carbon dioxide dissolves slightly in water to form a weak acid called carbonic acid, H_2CO_3, according to the following reaction
  $CO_2+H_2O\leftrightarrow H_2CO_3$
  Carbonic acid dissociates in water to form carbonate and bicarbonate.
  $H_2CO_3\leftrightarrow HCO_3^-+H^+\leftrightarrow CO_3^-+2H^+$
  Protons are produced during this dissociation process. As a result, the pH of water exposed to air is around 5.5 instead of 7. All solutions used in this work were measured by a pH meter. Due to uncertainty in exact pH value near pH=7, point are not represented in this pH range in Figs. 4F and 4H.

  We always started from 1 mol/L of defined salt solution, i.e. measure out 1 mole of salt (NaCl, KCl, KH_2PO_4, $MgCl_2$ and $CaCl_2$) dissolved in total volume of DI water (1000mL). We then performed serial dilutions to prepare salts of different concentration for our study. To avoid complex solutions with many ions, we used laboratory prepared pH solutions starting with 1M HCl and made serial dilution to get successive values between pH 0 to pH 6. Equivalently starting with 1M NaOH to get values between pH 14 to pH 8.

- ***Fetal Bovine Serum (FBS): Y.Coffinier***

  Standard FBS was purchased from Life technologies and stored in the freezer at -20°C. Ion concentration for Na^+, K^+ and Ca^{2+} were provided and are reported in Figure 4.8c. For Mg^{2+}, the ion concentration was estimated with an Idexx biochemical analyzer. Similar protocol as for DI water was used to prepare tubes of FBS with various ion concentrations. To avoid consuming large quantities of FBS, an ultra-microbalance (XP26 Mettler Toledo) was used. The smallest weight M was 300 µg. Each tube was 5 mL. Detailed values are shown in Table.

Salt/Conc. (mol/L)	**M(NaCl) mg**	**M(KCl) mg**	**M($CaCl_2$) mg**	**M($MgCl_2$) mg**
0.001	0.2922	0.3727	0.5549	0.4760
0.003	0.8766	1.1182	1.6647	1.4281
0.01	2.92	3.73	5.55	4.76
0.03	8.77	11.18	16.65	14.28
0.1	29.22	37.28	55.49	47.61
0.3	87.66	111.83	166.47	142.82
1	292.20	372.75	554.90	476.05

Electrical measurement

- ***Ag /AgCl electrode***

  For electrical measurements a commercial Ag/AgCl electrode (BAS) was inserted at the end of the microfluidic tube and used as the liquid-gate.

- ***Probe Card***

  A probe card with 12 DC probes and 12 triaxal cables was purchased from Cascade microtech with a specific design to our pattern. It was convenient for measurement of 4 devices simultaneously on a highly integrated chip. Probes are located at the front of the chip and microfluidic tubes at the back. The probe card was fixed inserted in a micromanipulator from Cascade Microtech.

Temperature in the electrical measurements room was strictly controlled at 293K.

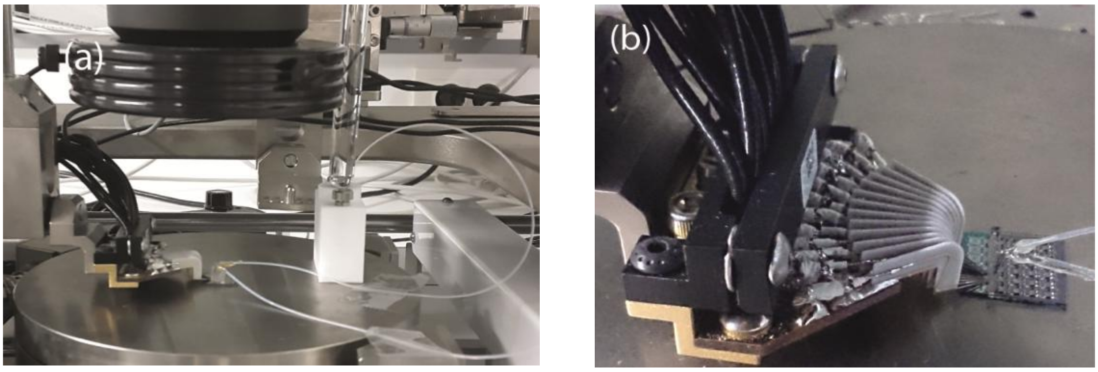

Figure A2 Photo of the experimental setup used in this study **(a)** with the reference electrode. **(b)** zoomed on the probe card that has 12 probes to address each of the 1.5 mm x 1.5 mm chips.

- ***Semiconductor parameter analyzer***

  Electrical measurements were performed with a Keithley 4200 SCS parameter analyzer. All sources were grounded to the ground unit via triaxal T.

- ***Measurements***

  Electrical measurement were done going from lower concentrated solution to higher concentration. At each switching of sample solution, the inlet tube is rinsed with DI water and blown with nitrogen. The solutions are delivered by the syringe pump (KD Scientific) with constant flow rate of 10µL/ min controlled manually. The pump is stopped during measurement.

- ***Ψ_0 plots***

  V_{th} to Ψ_0*:* Threshold voltages V_{th} were converted into surface potential via $\Psi_0=V_{th}(PZC)-V_{th}$.

- ***Activity conversion***

  Ions in solution interact with each other as well as with water molecules. At low concentrations and low background salt concentrations these interactions can possibly be ignored, but at higher concentrations ions behave chemically like they are less concentrated than they really are. Concentration can be related to activity using the free ion activity coefficient γ, where [a] =γ(c) with the site interaction theory (SIT). The value of γ depends on concentration of ions and charge in the solution, charge of the ion, and diameter of the ion (website: http://www.lenntech.com/calculators/activity/activity-coefficient.htm).

- ***Fits***

  Simulations and fits were performed with OriginC (Originlab software)

List of Publications

Publications in peer-reviewed journals

- **R. Sivakumarasamy**, K. Nishiguchi, A. Fujiwara, D. Vuillaume and N. Clément, A simple and inexpensive technique for PDMS/silicon chip alignment with sub-µm precision, **Anal. Methods**, 2014, 6, 97-101 (**Cover page selected**)
- **R. Sivakumarasamy**, K. Nishiguchi, D. Vuillaume, A. Fujiwara and N. Clément, Ultimate integration of a PDMS-based lab-on-a-chip with nanotransistor biosensors. Submitted
- **R. Sivakumarasamy**, K. Nishiguchi, A. Fujiwara and N. Clément, Anomalous pH response and ion selectivity beyond Nernst limit in Silicon Nanotransistors. Submitted

Oral presentation and poster in conferences

- **R. Sivakumarasamy**, K. Nishiguchi, A. Fujiwara, D. Vuillaume and N. Clément, Ultimate Integration of PDMS-based Lab-On-Chip with Nanotransistor Biosensors**, MNC 2013 International Conference,** Sapporo, Japan **(Oral Presentation)**
- **R. Sivakumarasamy**, E. Richard, C. Slomianny, D. Vuillaume, Y. Coffinier and N. Clément, Facile routes to acquire Single DNA functionalized gold nanoarrays on silicon chip. **EMRS-Spring Meeting 2014**, Lille, France (**Oral Presentation)**
- **R. Sivakumarasamy**, K. Nishiguchi*****, A. Fujiwara, D. Vuillaume and N. Clément, Zero Dimensional Ion-Sensitive Field-Effect Transistors, **MNC 2014 International Conference,** Fukuoka, Japan **(*Presented Poster)**

Titre / Title: Biocapteurs à base de nanotransistor 0D / 0D nanotransistor Biosensors

Résumé : L'objectif de cette thèse était d'explorer le potentiel des biocapteurs à base de transistors à 1 électron. Depuis l'invention de l'électrode de verre il y a plus de 100 ans, la réponse monotone du potentiel de surface avec le pH est devenue universelle. Aussi, il est bien connu que les mesures de la concentration en ions dans des solutions complexes, de grande importance pour le domaine biomédical, requière des membranes sélectives aux ions. En utilisant ces transistors nanométriques, nous montrons une rupture dans ces concepts avec l'observation d'une réponse en U au pH et la mesure sélective des cations Na^+, K^+, Ca^{2+} et Mg^{2+} dans le sérum sanguin, sans avoir recours aux membranes sélectives. Par ailleurs, les ions divalents ont été mesurés avec une sensibilité deux fois supérieure à la limite de Nernst. Les équations proposées, à l'origine d'une nouvelle méthode pour les mesures sélectives d'ions, peuvent-être étendues à la mobilité électrophorétique. Nous suggérons que ces nanotransistors 0D devraient également permettre des études biomimétiques de la compensation de charge des protéines. Nous montrons enfin que ces composants peuvent être intégrés sur un laboratoire sur puce en PDMS de 1.5 mm x 1.5 mm, qui promet un système de diagnostic sanguin peu couteux et très intégré.

Abstract: The aim of this thesis was to explore the potential of 0D nanotransistor biosensors. Since the invention of glass electrode a century ago, the monotonic decrease of oxides surface potential with pH has become universal. Also, it is well known that the measurement of ions concentration in complex solutions, of great importance for biomedical field, requires ion-selective membranes. Using these nanometric transistor biosensors, we report a rupture in these concepts with the observation of a U-shape pH response and the selective measurement of Na^+, K^+, Ca^{2+} and Mg^{2+} cations in blood serum, without falling back on selective membranes. In addition, divalent ions were measured with a sensitivity twice of that of Nernst limit. Proposed equations, at the origin of the new method for ion selective measurements, can be extended to the electrophoretic mobility. We also suggest that 0D nanotransistor biosensors are a relevant test bed for biomimetic studies of proteins charge compensation. We finally show that these devices can be ultimately integrated on a mm² PDMS-based lab-on chip, which promises for a cheap and small blood diagnosis system.

Mots clefs: Biocapteurs à base de nanotransistor 0D, laboratoire sur puce, ion-sensitive field-effect transistors, potentiel de surface en liquide, PDMS, selectivé ionique, ionogramme sanguine, microfluidique.

Keywords: 0D nanotransistor Biosensors, lab-on-chip, ion-sensitive field-effect transistors, surface potential in liquid, PDMS, ion selectivity, blood ionogram, microfluidic.